



National Library
of Canada

Acquisitions and
Bibliographic Services Branch

395 Wellington Street
Ottawa, Ontario
K1A 0N4

Bibliothèque nationale
du Canada

Direction des acquisitions et
des services bibliographiques

395, rue Wellington
Ottawa (Ontario)
K1A 0N4

Vous êtes votre bibliothèque

Vous êtes votre bibliothèque

NOTICE

The quality of this microform is heavily dependent upon the quality of the original thesis submitted for microfilming. Every effort has been made to ensure the highest quality of reproduction possible.

If pages are missing, contact the university which granted the degree.

Some pages may have indistinct print especially if the original pages were typed with a poor typewriter ribbon or if the university sent us an inferior photocopy.

Reproduction in full or in part of this microform is governed by the Canadian Copyright Act, R.S.C. 1970, c. C-30, and subsequent amendments.

AVIS

La qualité de cette microforme dépend grandement de la qualité de la thèse soumise au microfilmage. Nous avons tout fait pour assurer une qualité supérieure de reproduction.

S'il manque des pages, veuillez communiquer avec l'université qui a conféré le grade.

La qualité d'impression de certaines pages peut laisser à désirer, surtout si les pages originales ont été dactylographiées à l'aide d'un ruban usé ou si l'université nous a fait parvenir une photocopie de qualité inférieure.

La reproduction, même partielle, de cette microforme est soumise à la Loi canadienne sur le droit d'auteur, SRC 1970, c. C-30, et ses amendements subséquents.

UNIVERSITY OF ALBERTA

BENDING STRENGTH OF
LONGITUDINALLY STIFFENED STEEL CYLINDERS

by

QISHI CHEN



A thesis submitted to the Faculty of Graduate Studies and Research
in partial fulfillment of the requirements for the degree of Doctor of Philosophy.

DEPARTMENT OF CIVIL ENGINEERING

EDMONTON, ALBERTA

FALL 1993



National Library
of Canada

Acquisitions and
Bibliographic Services Branch

395 Wellington Street
Ottawa, Ontario
K1A 0N4

Bibliothèque nationale
du Canada

Direction des acquisitions et
des services bibliographiques

395, rue Wellington
Ottawa (Ontario)
K1A 0N4

Your file / Votre référence

Our file / Notre référence

The author has granted an irrevocable non-exclusive licence allowing the National Library of Canada to reproduce, loan, distribute or sell copies of his/her thesis by any means and in any form or format, making this thesis available to interested persons.

L'auteur a accordé une licence irrévocable et non exclusive permettant à la Bibliothèque nationale du Canada de reproduire, prêter, distribuer ou vendre des copies de sa thèse de quelque manière et sous quelque forme que ce soit pour mettre des exemplaires de cette thèse à la disposition des personnes intéressées.

The author retains ownership of the copyright in his/her thesis. Neither the thesis nor substantial extracts from it may be printed or otherwise reproduced without his/her permission.

L'auteur conserve la propriété du droit d'auteur qui protège sa thèse. Ni la thèse ni des extraits substantiels de celle-ci ne doivent être imprimés ou autrement reproduits sans son autorisation.

ISBN 0-315-88082-1

UNIVERSITY OF ALBERTA

RELEASE FORM

NAME OF AUTHOR: QISHI CHEN

TITLE OF THESIS: BENDING STRENGTH OF LONGITUDINALLY
STIFFENED STEEL CYLINDERS

DEGREE: DOCTOR OF PHILOSOPHY

YEAR THIS DEGREE GRANTED: 1993

Permission is hereby granted to the University of Alberta Library to reproduce single copies of this thesis and to lend or sell such copies for private, scholarly or scientific research purposes only.

The author reserves other publication rights in association with the copyright in the thesis, and except as hereinbefore provided neither the thesis nor substantial portion thereof may be printed or otherwise reproduced in any material form whatever without the author's prior written permission.



21, 7803-105 Street

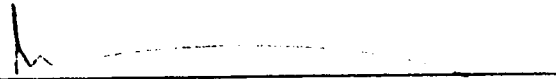
Edmonton. Alberta T6E 4H1

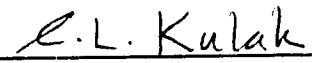
August 23, 1993

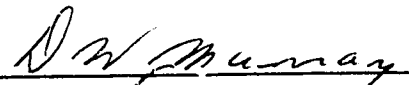
UNIVERSITY OF ALBERTA

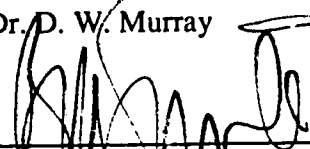
FACULTY OF GRADUATE STUDIES AND RESEARCH


The undersigned certify that they have read, and recommend to the Faculty of Graduate Studies and Research for acceptance, a thesis entitled Bending Strength of Longitudinally Stiffened Steel Cylinders submitted by Qishi Chen in partial fulfillment of the requirements for the degree of Doctor of Philosophy in Civil Engineering.



Dr. A. E. Elwi (Co-supervisor)


Dr. G. L. Kulak (Co-supervisor)


Dr. D. W. Murray


Dr. W. J. Spruce


Dr. A. W. Lipsett


Dr. H. G. L. Prion (External Examiner)

August 23, 1993

ABSTRACT

Fabricated steel cylinders with large R/t ratios are often used in conveyor galleries, offshore platforms, storage tanks, towers, vessels, and the like. The use of longitudinal stiffeners in these large cylinders has proven to be an efficient way to promote structural stability. The increase of load capacity is significant. However, the attachment of the stiffeners complicates the problem by introducing additional buckling modes and new design parameters.

Research needs exist for fabricated large cylinders with longitudinal stiffeners. The lack of large-scale bending test data and, thus, a verified analytical model, limits its efficient use as a structural element. The failure loads for bending suggested by available design specifications are very conservative.

The objective of the research program was to investigate the local buckling behavior and ultimate load capacity of longitudinal stiffened steel cylinders subjected to bending. It included a comprehensive study of the experiment, the finite element analysis, and the design of these structures.

In the experimental phase, four large-scale specimens were tested. The collected data included the load versus deformation behavior, as well as the geometric imperfections and welding residual stresses of the specimens.

A finite element model of stiffened cylinders in bending was established using the program NISA. The geometric imperfections and welding residual stresses measured in the tests were incorporated into the model. The analysis was verified through the simulation of experiments, and then was extended to cylinders with different parameters.

On the basis of experimental and numerical results, a parametric study was conducted. Buckling behavior of different failure modes is summarized and the effect of key parameters is identified. A set of new design equations and the corresponding design procedure are proposed.

ACKNOWLEDGEMENTS

The author is deeply grateful to his supervisors, Dr. A. E. Elwi and Dr. G. L. Kulak, for their support, supervision and participation throughout the course of this study.

This study forms part of a continuing research program undertaken in the Department of Civil Engineering at the University of Alberta. The objective of the program is to experimentally and numerically investigate the local buckling behavior of large diameter steel cylinders under transverse loading, and to produce relevant design information. The current study is jointly funded by the National Science and Engineering Research Council of Canada, the Government of the Province of Alberta, and the Department of Civil Engineering at the University of Alberta.

The advice and assistance provided by laboratory technicians R. Helfrich and L. Burden, and summer employee S. Undershute during the experimental phase of this project are greatly appreciated.

Finally, the author wishes to thank his wife, Weiping, for her encouragement and support and son, Edmond, for his patience and understanding.

TABLE OF CONTENTS

Chapter One Introduction.....	1
1.1 Background to the Problem	1
1.2 Objectives.....	2
1.3 Organization of the Thesis	3
 Chapter Two Literature Review	 4
2.1 Large-Scale Experiments of Fabricated Steel Cylinders.....	4
2.1.1 Longitudinally Stiffened Cylinders in Bending	5
2.1.2 Unstiffened Cylinders in Bending	5
2.1.3 Longitudinally Stiffened Cylinders in Axial Compression	6
2.2 Design Guidelines	6
2.2.1 API, ASME and ECCS Recommendations.....	7
2.2.2 DnV and CSA Standards	9
2.3 Other Design Models	10
2.3.1 The Reduced Stiffness Method	11
2.3.2 The Equivalent Column Approach	11
2.4 Finite Element Analysis	12
2.4.1 Unstiffened Cylinders in Bending.....	12
2.4.2 Unstiffened Cylinders in Shear	13
2.4.3 Longitudinally Stiffened Cylinders in Axial Compression	13
2.5 Summary.....	14
 Chapter Three Experimental Study.....	 17
3.1 General.....	17
3.2 Test Specimens.....	17
3.2.1 Design and Fabrication	17
3.2.2 Material Properties.....	18
3.2.3 Initial Imperfections	19
3.2.4 Residual Stresses	22
3.3 Test Program	24
3.3.1 Test Set-Up.....	24
3.3.2 Instrumentation	25
3.3.3 Test Procedure	27

3.4 Test Results.....	28
3.4.1 Specimen SB2	28
3.4.2 Specimen SB3a	29
3.4.3 Specimen SB3b.....	30
3.4.4 Specimen SB4	30
3.5 Summary.....	31
Chapter Four Numerical Simulation of Experiments	53
4.1 General.....	53
4.2 NISA Program	54
4.3 Finite Element Model.....	55
4.3.1 The Cylinder	55
4.3.2 The Stiffeners	56
4.3.3 The Rigid End.....	57
4.3.4 Loading	58
4.4 Initial Imperfections	59
4.5 Residual Stresses	60
4.6 Numerical Results	63
4.6.1 Test SB2.....	63
4.6.2 Test SB3a.....	64
4.6.3 Test SB3b	65
4.6.4 Test SB4.....	65
4.6.5 Test SB1.....	66
4.7 Summary.....	67
Chapter Five Finite Element Analysis for Parametric Study.....	81
5.1 General.....	81
5.2 Selection of Parameters	82
5.3 Configuration.....	83
5.4 Numerical Model.....	85
5.5 Initial Imperfections	85
5.6 Residual Stresses	87
5.7 Buckling Behavior.....	88
5.7.1 Curvature and Displacement.....	88
5.7.2 Failure Mode	89
5.8 Effect of Residual Stresses and Initial Imperfections.....	91

5.9 Summary.....	92
Chapter Six Design for Bending Capacity	111
6.1 General.....	111
6.2 Evaluation of Existing Design Provisions	111
6.3 Parametric Study.....	114
6.3.1 Shell Buckling outside the Stiffened Area	114
6.3.2 Failure in the Stiffened Area.....	116
6.4 Interaction of Buckling Modes in Stiffened Cylinders	117
6.4.1 Classical Buckling Analysis.....	118
6.4.2 Mode Interaction.....	119
6.4.3 Design Considerations.....	120
6.5 Capacity for the Case of Shell Buckling outside the Stiffened Area	121
6.6 Capacity for the Case of Failure in the Stiffened Area.....	126
6.7 Design Procedure for Longitudinal Stiffeners.....	128
6.8 Comparison with the Bending Strength of Unstiffened Cylinders.....	130
6.9 Summary.....	131
Chapter Seven Conclusions	141
7.1 Conclusions	141
7.2 Discussion	142
References.....	144
Appendix The IGI Programs	149

LIST OF TABLES

Table 2.1	Dimensions of Specimen SB1	15
Table 2.2	Material Properties of Specimen SB1	15
Table 2.3	Large-Scale Flexural Tests of Unstiffened Cylinders	16
Table 2.4	Large-Scale Compression Tests of Longitudinally Stiffened Cylinders.....	16
Table 3.1	Dimensions of Test Specimens	33
Table 3.2	Material Properties.....	33
Table 3.3	Maximum Magnitude of Initial Imperfections	34
Table 3.4	Test Results.....	34
Table 4.1	Symmetric Boundary Conditions	68
Table 4.2	Parameters for the Material Model of HSS Stiffeners	68
Table 4.3	Comparison of Numerical Analysis and Physical Tests.....	69
Table 5.1	Cylinders for the Parametric Study	93
Table 5.2	Capacity and Failure Mode of Cylinders for the Parametric Study	94
Table 5.3	Effect of Compressive Residual Stress.....	95
Table 5.4	Effect of Tensile and Compressive Residual Stresses.....	95
Table 6.1	Ultimate Moment Predicted by API Design Guideline	132
Table 6.2	Ultimate Moment Predicted by Equation 6.13.....	133
Table 6.3	Comparison of Design Capacity	134

LIST OF FIGURES

Figure 3.1	Schematic of test specimens.....	35
Figure 3.2	Tensile coupon tests for cylinder material	36
Figure 3.3	Stub column test of the HSS stiffener (specimen SB2).....	37
Figure 3.4	Categories of initial imperfections.....	38
Figure 3.5	Specimen SB2: measured initial imperfections.....	39
Figure 3.6	Specimen SB3a: measured initial imperfections	40
Figure 3.7	Specimen SB2: measured residual strains	41
Figure 3.8	Test set-up: overview	42
Figure 3.9	Test set-up: the composite beam	43
Figure 3.10	Instrumentation: measurement for displacement and strain.....	44
Figure 3.11	Specimen SB2: moment versus curvature response.....	45
Figure 3.12	Specimen SB2: deformed shape.....	45
Figure 3.13	Specimen SB2: strain distribution.....	46
Figure 3.14	Specimen SB3a: moment versus curvature response.....	46
Figure 3.15	Specimen SB3a: strain distribution.....	47
Figure 3.16	Specimen SB3a: moment versus compressive strain at different cross-sections.....	47
Figure 3.17	Specimen SB3b: moment versus deflection response.....	48
Figure 3.18	Specimen SB3b: strain distribution.....	48
Figure 3.19	Specimen SB3b: buckles in the stiffened area.....	49
Figure 3.20	Specimen SB3b: deformed stiffeners and shells.....	49
Figure 3.21	Specimen SB3b: moment versus curvature response	50
Figure 3.22	Specimen SB4: moment versus compressive strain at different cross-sections.....	50
Figure 3.23	Specimen SB4: moment versus curvature response.....	51
Figure 3.24	Specimen SB4: strain distribution	51
Figure 3.25	Specimen SB4: deformed shape	52

Figure 4.1	Degrees of freedom of the plate-shell element	70
Figure 4.2	Schematic of the finite element model.....	71
Figure 4.3	Boundary conditions for the finite element model	72
Figure 4.4	Dual node model.....	73
Figure 4.5	Assumed residual stress distribution	73
Figure 4.6	Comparison of residual stress distribution for SB2: shell between stiffeners.....	74
Figure 4.7	Comparison of residual stress distribution for SB2: shell outside the stiffened area	74
Figure 4.8	Material model for HSS stiffeners of SB2.....	75
Figure 4.9	Moment versus curvature response of test SB2.....	75
Figure 4.10	Deformed shape of SB2	76
Figure 4.11	Material model for shell of SB3a and SB3b.....	76
Figure 4.12	Moment versus curvature response of test SB3a	77
Figure 4.13	Deformed shape of SB3a	77
Figure 4.15	Deformed shape of SB3b.....	78
Figure 4.14	Moment versus curvature response of test SB3b	78
Figure 4.16	Moment versus curvature response of test SB4.....	79
Figure 4.17	Deformed shape of SB4	79
Figure 4.18	Moment versus curvature response of test SB1.....	80
Figure 4.19	Deformed shape of SB1	80
Figure 5.1	Deformed shape of S24a	96
Figure 5.2	Deformed shape of S24b	96
Figure 5.3	Deformed shape of S11.....	97
Figure 5.4	Deformed shape of S12.....	97
Figure 5.5	Deformed shape of S13.....	98
Figure 5.6	Deformed shape of S14.....	98
Figure 5.7	Deformed shape of S21.....	99
Figure 5.8	Deformed shape of S22.....	99
Figure 5.9	Deformed shape of S23.....	100

Figure 5.10	Deformed shape of S24.....	100
Figure 5.11	Deformed shape of S31.....	101
Figure 5.12	Deformed shape of S32.....	101
Figure 5.13	Deformed shape of S33.....	102
Figure 5.14	Deformed shape of S34.....	102
Figure 5.15	Moment versus curvature response of S13.....	103
Figure 5.16	Moment versus curvature response of S14.....	103
Figure 5.17	Moment versus curvature response of S21.....	104
Figure 5.18	Moment versus displacement response of S21.....	104
Figure 5.19	Moment versus curvature response of S23.....	105
Figure 5.20	Moment versus displacement response of S23.....	105
Figure 5.21	Moment versus curvature response of S24.....	106
Figure 5.22	Moment versus displacement response of S24.....	107
Figure 5.23	Moment versus curvature response of S31.....	108
Figure 5.24	Moment versus displacement response of S31.....	108
Figure 5.25	Moment versus curvature response of S33.....	109
Figure 5.26	Moment versus displacement response of S33.....	110

Figure 6.1	Comparison of API guideline with test and numerical analysis.....	135
Figure 6.2	Failure mode: inside or outside the stiffened area.....	135
Figure 6.3	Failure in the stiffened area: general buckling versus shell buckling.....	136
Figure 6.4	Effect of the spacing to thickness ratio (s/t) for $\Phi = 77.3^\circ$	136
Figure 6.5	Effect of the spacing to thickness ratio (s/t) for $\Phi = 51.6^\circ$	137
Figure 6.6	Effect of the radius to thickness ratio (R/t)	137
Figure 6.7	Effect of the angle Φ for $s/t = 54$	138
Figure 6.8	Design curves for multiple buckling modes	138
Figure 6.9	Comparison of Equation 6.11 with the finite element results	139
Figure 6.10	Effect of the torsional stiffness (J_s) of longitudinal stiffeners.....	139
Figure 6.11	Comparison of Equation 6.13 with test and numerical results	140
Figure 6.12	Comparison of stiffened versus unstiffened cylinders	140

LIST OF SYMBOLS

Latin Characters

a	scaling factor used to plot displacements or imperfections in finite element meshes
A	cross-sectional area
A_s	cross-sectional area of a stiffener
E	Young's modulus of elastic material
E_{h1}, E_{h2}	hardening modulus
f	stress resulting from applied load
F	buckling stress for design
FS	factor of safety
I_y	moment of inertia about y-axis
J_s	St. Venant torsional stiffness of a stiffener
M	bending moment
M_p	fully plastic moment
M_u	ultimate moment
$M_{u\text{ prd}}$	predicted ultimate moment
N_x	shape function for displacement U_x
P	axial compression force
P_u	ultimate axial force
P_y	yield axial force
R	radius of middle surface
s	center-to-center spacing of stiffeners
s_e	effective spacing between stiffeners
t	shell thickness

t_e	equivalent shell thickness of stiffened cylinders
T	temperature applied to generate initial strains
\mathbf{u}	displacement vector
\mathbf{u}_0	pre-buckling displacement vector
\mathbf{u}_i	displacement vector for i th buckling mode
\mathbf{u}_{ij}	second-order displacement vector for i th and j th buckling mode
\mathbf{U}_T	thermal displacement vector
U_x, U_y, U_z	displacements in global coordinate system
\mathbf{U}_0	initial imperfection vector
$d\mathbf{U}$	change of displacement increment during iterations
$\Delta\mathbf{U}$	total increment of displacement vector
z_0	z coordinate of neutral axis

Greek Characters

α	knockdown factor to account for initial imperfections
α_T	coefficient of thermal expansion
γ_s	coefficient reflecting material properties and R/t ratio in Stephens' equation
ϵ	strain
ϵ_1	tolerance for convergence
ϵ_{rc}	compressive residual strain
ϵ_x	longitudinal strain
η	knockdown factor to account for inelasticity
λ	load factor
λ_c	critical load factor for a perfect system

λ_i	load factor for i th buckling mode
ξ_i	amplitude factor for i th buckling mode
σ_{cr}	elastic buckling stress
σ_r	residual stress
σ_{rc1}	compressive residual stress in the shell between stiffeners
σ_{rc2}	compressive residual stress in the shell outside the stiffened area
σ_t	tensile residual stress
σ_T	thermal stress vector
σ_u	ultimate stress for the shell outside the stiffened area
σ_x	longitudinal stress
σ_y	static yield stress
σ_{y2}	yield stress in the shell outside the stiffened area
σ_θ	circumferential stress
σ_1	ultimate stress for unstiffened cylinders
Φ	angle along the circumference covered by longitudinal stiffeners
Φ_1	modified value of angle Φ
ϕ_x, ϕ_y, ϕ_z	rotation of shell node normal about the global x -, y - and z -axis
ϕ_θ	rotation of shell node normal about the tangent of the circumference
Φ_1	first eigenvector
χ	coefficient reflecting the effect of R/t ratio

CHAPTER ONE

INTRODUCTION

1.1 Background to the Problem

Cylindrical shells with large radius to thickness ratio (R/t) which are subjected to axial forces, shear forces, and bending moments usually fail by local buckling. In order to enhance the buckling strength, cylinders can be longitudinally stiffened (also called stringer-stiffened or axially stiffened), circumferentially stiffened (ring-stiffened), or stiffened in both directions (orthogonally stiffened). Longitudinal stiffening is considered effective for buckling due to bending or axial compression. Circumferential stiffeners are used when the loading condition involves external pressure, or to reduce the ovalization of the thin-walled cross-section.

Stiffened steel cylinders are often used as conveyor galleries, columns of offshore platforms, and other civil engineering structures. These cylinders are fabricated by cold-rolling steel plates into curved cylindrical shells. The tubes are completed by performing longitudinal seam welding. The short tubes formed in this way are then joined together by circumferential girth welds to form long spans. Longitudinal or circumferential stiffeners are welded to the shell surface. Inevitably, initial geometric imperfections and residual stresses are introduced in the fabrication procedure.

This study deals with longitudinally stiffened cylinders subjected to flexural moment, particularly of the configuration usually used as conveyor galleries. These structures have a R/t ratio between 100 to 400. The outside diameter ranges from 2.5 to 4 meters. Circumferential stiffeners are often welded at intervals of 0.5 to 2.0 diameters to help maintain the round shape of the tubes. The span can be as long as 60 meters. An example of such a long span is the main tubular conveyor at the Genesee Power Plant in Alberta.

A representative model to study flexural buckling behavior of longitudinally stiffened cylinders is a segment of cylinder under pure bending. Since the local buckling wavelength can be expected to be very short compared with the radius, a length equal to the diameter is sufficient for the segment. Practical boundary effects such as imperfections due to girth welds and the variation of shell thickness should also be reflected in the model.

The flexural capacity of longitudinally stiffened cylinders is usually governed by the instability of a local area that is highly stressed in compression. The buckling modes of such failure include a number of possible cases:

- (1) Shell buckling, in which shell plating buckles like an unstiffened cylinder. The stiffeners essentially remain straight.
- (2) General buckling, in which the shell and longitudinal stiffeners buckle simultaneously. This happens when the stiffeners are closely spaced.
- (3) Stiffener buckling, in which the stiffeners are twisted and distorted before shell buckling. This mode may occur when stiffeners with low torsional stiffness, such as thin-walled open cross-sections, are used.

Of course, these buckling modes may interact with each other.

The flexural behavior of a longitudinally stiffened cylinder differs from an unstiffened cylinder because stiffeners provide restraint to the shells and introduce additional buckling modes. It is also different from axial compression behavior because the bending stress is not uniform and can be redistributed after local failure.

Because there is inadequate research into the flexural behavior of stiffened cylinders at the present time, the assumption that buckling stress in bending is equal to that in uniform compression is widely employed in design guidelines. Although unstiffened cylinders tend to fail at comparable stress levels in bending and compression, it was found in a previous bending test of a longitudinally stiffened cylinder (Bailey and Kulak 1984) that the ultimate moment in general instability failure is about 90% of the fully plastic moment of the stiffened cylinder (or 6% higher than the yield moment). Apparently, the design criteria based on uniform compression could not predict such a high capacity. These design criteria need to be examined so that the benefit of longitudinal stiffeners can be fully recognized.

1.2 Objectives

The objective of the study is to investigate the buckling behavior of longitudinally stiffened cylinders subjected to bending. Such failure dominates the flexural capacity of these structural elements. The study will focus on the general buckling mode, the shell

buckling mode, and their interaction. The local buckling of stiffeners is not included in the scope of this study.

The following objectives are considered essential for the completion of this study:

- (1) To review and evaluate current design procedures.
- (2) To carry out an experimental study of large-scale specimens.
- (3) To establish a finite element model that can predict the buckling behavior and the ultimate bending capacity.
- (4) To demonstrate the validity of the model by comparison with the results of physical tests.
- (5) To examine the effect of initial imperfections and residual stresses on buckling behavior.
- (6) To identify the parameters that affect the buckling behavior and capacity and to study their effects through an extensive numerical parametric study.
- (7) To present recommendations that will improve current design practice.

1.3 Organization of the Thesis

Chapter Two presents a review of existing literature and design guidelines. The experimental program is described in Chapter Three. It includes the measurements of material properties, initial imperfections, and residual stresses. The test results of four large-scale specimens, which have an outside diameter of 1270 mm, are presented and observations are noted. Chapter Four presents the finite element model used for the simulation of physical tests. The capability of the model is demonstrated by comparing the numerical and experimental results. This model is then used to carry out a numerical analysis of cylinders with different parameters. The results of the analysis are presented in Chapter Five. The buckling behavior, the ultimate flexural capacity, and the effect of imperfections and residual stresses upon the numerical models are examined. A parametric study based upon the results of the tests and the numerical study is reported in Chapter Six. These results have also been used to evaluate current design guidelines. New design equations based on the parametric study are proposed for different failure modes. A design procedure for longitudinal stiffeners is also outlined in Chapter Six. Finally, the conclusions of this study are presented in Chapter Seven.

CHAPTER TWO

LITERATURE REVIEW

Early research into the stability of stiffened cylinders (from the 1930's to 1970's) was generally associated with aeronautical industry. Relevant research in this field is reviewed by Becker (1958), and tests of aluminium alloy cylinders were summarized by Ellinas and Croll (1983). The shell thickness was less than 1/3 mm for most of these cylinders while the R/t ratio could be over 1000. Unlike civil engineering structures, a large portion of material was used to construct rigid stiffeners. The cylinder was usually fabricated by covering an orthogonal frame, which consisted of longitudinal and circumferential stiffeners, with a thin membrane, or by machining a tube into a thin shell with flat longitudinal stiffeners. Test results showed that the levels of buckling stress were in the linear elastic regime.

Since the material properties, geometry of the shell and stiffeners, and imperfections and residual stresses that arise during the fabrication of aerospace shells are significantly different from those of fabricated steel cylinders, the focus of the following review will be limited to the testing, analysis, and design of fabricated large diameter steel cylinders.

2.1 Large-Scale Experiments of Fabricated Steel Cylinders

Testing of large-scale specimens is the most direct and reliable way to investigate the buckling behavior of large diameter steel cylinders. The specimens in such tests are usually fabricated by industrial procedures, so that the material, initial imperfections, and residual stresses can represent the situation in the practical structures.

A number of small-scale compression tests of stiffened steel cylinders were reported by Walker *et al.* (1982) and by Ageiidis *et al.* (1982). Those small models usually had a radius of 160 mm and an R/t ratio of about 200. It can be expected that, because of different fabrication procedures, the residual stresses and imperfections of small models diverge from those of industrial structures. Therefore, this review will cover only large-scale experiments.

2.1.1 Longitudinally Stiffened Cylinders in Bending

The test done by Bailey and Kulak (1984), designated as SB1 hereafter, was the first one reported in this category—a large diameter longitudinally stiffened fabricated steel cylinder subjected to pure bending. The test set-up and the arrangement of the test specimen were similar to that which will be described in Chapter Three: a composite beam was built using two heavy end trusses, with the specimen placed between them and subjected to pure bending under a two point loading system. The clearance below the specimen was relatively small, and this subsequently affected the test.

Cylinder SB1 was made of CSA G40.21M 300W steel and it had an R/t ratio of 128. Five HSS 50.8 x 25.4 x 3.18 longitudinal stiffeners were welded to the compression region of the 5.05 mm thick cylinder, covering an angle of 76° . The geometry and material properties of the specimen are given in Tables 2.1 and 2.2, respectively.

The failure mode of SB1 was typical of general buckling. After yielding of the shell between stiffeners, initial shell buckling was observed at a bending moment of 2200 kN·m. The development of buckles forced the stiffeners to bend together with the shell. The load continued to rise at a decreasing rate as the buckling waves increased in size. As the test was approaching the ultimate load, the deflection of the testing apparatus became so large that the specimen was approaching the floor. Photographs of the specimen showed that the buckles were appreciably deep and wide at the time when testing had to be terminated. The maximum moment achieved during the test was 3068 kN·m, which is about 89% of the theoretical plastic moment capacity.

2.1.2 Unstiffened Cylinders in Bending

Three large diameter unstiffened steel cylinders were also tested at the University of Alberta. Specimens B1 and B2 were made of grade 300W hot-rolled steel plates (Stephens *et al.* 1982), and specimen B3 was fabricated from grade 700Q low alloy steel (Bailey and Kulak 1984). As summarized in Table 2.3, the R/t ratios vary from 149 to 222. Test results showed that all three shells failed by local buckling at the extreme compression zone.

Table 2.3 also lists the ratio of ultimate test moment, M_u , divided by the fully plastic moment, M_p , for these tests. Specimen B1 has geometry (R and t) and material properties (E and σ_y) similar to that of the longitudinally stiffened specimen SB1 described

in Section 2.1.1. However, the moment ratio of unstiffened cylinder B1 ($M_u/M_p = 0.475$) is only 53% of that of the stiffened cylinder SB1 ($M_u/M_p = 0.891$). In this case, the use of longitudinal stiffeners nearly doubled the moment ratio.

Based on test data of fabricated cylinders subjected to axial compression, Stephens *et al.* (1982) proposed a set of design formulae to predict the buckling stress of tubular members subjected to uniform compression. As concluded by Stephens *et al.* (1982) and by Bailey and Kulak (1984), the flexural buckling stresses of B1, B2 and B3 could also be reasonably predicted by these formulas.

2.1.3 Longitudinally Stiffened Cylinders in Axial Compression

Green and Nelson (1982) reported the testing of three large diameter longitudinally stiffened cylinders subjected to axial compression. The radius of the specimens was nearly 600 mm and the R/t ratio varied from 95 to 285 as a result of the use of different shell thicknesses. The arrangement of stiffeners was typical for offshore platforms: flat steel strips were welded to the inside surface of the cylinders. Residual stresses arising from the welding of stiffeners were measured. It was observed that the presence of a significant compressive residual stress caused local yielding to precede shell buckling. The review of the test results indicates that the level of residual stresses probably affects the load-carrying capacity. Specimen GU1, which had a high level of compressive residual stress because of its small shell thickness ($t = 2$ mm), failed by local shell buckling and the P_u/P_y ratio was only 69%. Meanwhile, GU2, which had a relatively low level of residual stress, reached a P_u/P_y ratio of 97%. The geometry, measured compressive residual strain, and the failure capacity of these specimens are summarized in Table 2.4.

Unstiffened cylinders with relatively small R/t ratios have also been tested under axial compression and flexure (Chen and Han 1985, Prion and Birkemoe 1987, and SSRC 1988). However, the stiffness of these shells is higher because of their large curvature. Consequently, local shell buckling behavior and strength are different from those with large R/t ratios.

2.2 Design Guidelines

The existing design rules for longitudinally stiffened steel cylinders have generally been developed for offshore structure design codes. The guidelines reviewed in this section are the most recent provisions used in North America and in Europe.

2.2.1 API, ASME and ECCS Recommendations

The American Petroleum Institute, API, published a stability design bulletin (Bulletin 2U) for cylindrical shells (API 1987). The bulletin applies mainly to steel tubular columns in tension leg platforms. Design equations are based upon the allowable stress design method, which can be expressed as

$$f < \frac{F}{FS} \quad (2.1)$$

In Equation 2.1, f is the stress resulting from the applied loads according to linear elastic analysis and FS is the factor of safety, which ranges from 1.25 to 2. The general expression for buckling stress F is given as

$$F = \alpha \eta \sigma_{cr} \quad (2.2)$$

in which σ_{cr} is the elastic buckling stress for a perfect shell, and α and η are knockdown factors to account for imperfections and inelasticity, respectively. The critical stress σ_{cr} is obtained from elastic buckling analysis of stiffened or unstiffened shells in various loading cases, and then calibrated to elastic buckling tests by α and to inelastic tests by η . Different values of α are given to structures with various buckling modes and different geometry. Based on the assumption that unstiffened cylinders have similar buckling strength whether in compression or in bending, the allowable stress for bending is established as the same as that for compression, for both stiffened and unstiffened cylinders. However, such an assumption may be too conservative for the general buckling of stiffened cylinders.

The general buckling stress and the local shell buckling stress for longitudinally stiffened cylinders subjected to bending are specified by API as outlined following.

General buckling

The general buckling of a longitudinally stiffened cylinder is called “bay instability” by API. The elastic bay instability stress is given by two approaches: the orthotropic shell equation and the equivalent column equation.

The orthotropic shell equation, which is based on the work of Block *et al.* (1965), is the standard approach recommended by API. It assumes that the longitudinal stiffeners are “smeared” over the shell surface so that the shell has orthotropic stiffness properties in

the longitudinal and circumferential directions. The elastic buckling stress of the orthotropic shell is derived as

$$\sigma_{cr} = \frac{\det \begin{pmatrix} A_{11} & A_{12} & A_{13} \\ A_{21} & A_{22} & A_{23} \\ A_{31} & A_{32} & A_{33} \end{pmatrix}}{Y \det \begin{pmatrix} A_{11} & A_{12} \\ A_{21} & A_{22} \end{pmatrix}} \quad (2.3)$$

in which Y is a function of the shell length. The elements of the A matrix depend upon the properties of the orthotropic shell, such as the Young's modulus E_{ij} , the shear modulus G_{ij} , and the flexural stiffness D_{ij} . The indices i and j refer to the orthotropic axes z or θ . In this procedure, the three key factors to be determined are the effective shell width between stiffeners and the number of buckling waves in each of the circumferential and longitudinal directions. These three factors are calculated iteratively so that the lowest buckling stress can be obtained.

Orthotropic analysis has been generally accepted for densely stiffened cylinders. For the approach to be valid, the cylinder should behave like a continuous shell rather than as a system of discrete stiffeners and shell panels. Usually, there should be at least two longitudinal stiffeners in every circumferential buckling halfwave length (Walker and Sridharan 1980).

In addition to the orthotropic shell equation, the API guideline adopted the equivalent column equation (Faulkner *et al.* 1983) as an alternative approach for bay instability. This equation is a direct analogy of a column buckling expression. The equivalent column consists of a longitudinal stiffener and the effective portion of the adjacent shell plating. The elastic general buckling stress is approximately the sum of the Euler buckling stress of the pseudo-column and the classical shell buckling stress of a shell panel. Compared with the orthotropic shell equation, the procedure is quite lengthy, even though no iterations are involved.

Both the orthotropic shell equation and the equivalent column equation have been used to predict the failure loads of the test SB1 reported by Bailey and Kulak (1984). The moment capacity predicted by the orthotropic shell equation is 2248 kN·m and that predicted by the equivalent column equation is 2312 kN·m. These predictions are conservative by 27% and 25%, respectively, when compared with the maximum moment attained in the test. The safety factor specified by API has not been applied to the above calculations.

Shell buckling

The elastic local buckling stress of the shell between stiffeners is given by the classical formula (SSRC 1988) for unstiffened cylindrical shells, i.e.

$$\sigma_{cr} = C E \frac{t}{R} \quad (2.4)$$

where the parameter C varies according to the geometry of the cylinder. It is noted that the advantage of stiffening is not contained in Equation 2.4. For densely stiffened shells, however, the knockdown factor for imperfections, α (Equation 2.2), is higher than that for unstiffened shells. This may be based upon the analytical results which indicated that stiffened cylinders are less sensitive to imperfections than are their unstiffened counterparts (Hutchinson and Amazigo 1967). The boundary effect due to the torsional resistance of stiffeners and the stiffener spacing is not considered in the calculation for the shell buckling stress.

In order to avoid the possible interaction of different buckling modes, the API guideline requires that the calculated buckling stresses for other modes be at least 20% greater than that of local shell buckling. As a result, the load-carrying capacity is always governed by local shell buckling between stiffeners.

Design criteria similar to the API bulletin can also be found in the shell buckling design code for metal containment vessels, published by the American Society of Mechanical Engineers (ASME 1986), and in the European recommendations for steel shell design, prepared by the European Convention for Constructional Steelwork (ECCS 1988). There are only minor differences among the three guidelines, mainly in the knockdown factors and the effective width of the shell between stiffeners.

2.2.2 DnV and CSA Standards

The design rules of Det norske Veritas for mobile offshore structures (DnV 1987) include the buckling strength analysis for stiffened or unstiffened cylinders subjected to bending. The allowable bending stress is set equal to that for axial compression. The buckling resistance of a longitudinally stiffened cylinder may be calculated by the method used for stiffened plates unless the advantage of curvature is significant. Since the conventional design of stiffened plates requires stiffeners to support the plate as rigid nodal

lines, the use of frequent and heavy stiffeners is emphasized. In fact, the stiffening effect is neglected for stiffener spacing (s) in excess of a moderate value ($s/t > 3\sqrt{R/t}$). The buckling strength of stiffened plates is given by empirical equations based on approximate methods. Generally, the DnV rules are more conservative than the API provisions (API 1987).

The Canadian standard for fixed steel offshore structures (CSA 1992) made significant reference to the DnV rules for the design of longitudinally stiffened cylinders. These cylinders are classified into three categories. Category A includes sparsely stiffened cylinders, which are designed as unstiffened cylinders. The buckling strength of cylinders with closely spaced heavy stiffeners (Category B) is taken equal to that of an equivalent stiffened flat plate. A simplified orthotropic shell design equation is used for Category C, which consists of densely stiffened cylinders using light stiffeners.

The rules of classification are similar in the DnV and CSA standards. For example, when the spacing ratio, s/t , is larger than $3\sqrt{R/t}$, the shell is considered a Category A cylinder and the buckling strength is similar to its unstiffened counterpart. For the test specimen SB1 of Bailey and Kulak (1984), it is found that s/t ratio is 42.6, which is greater than $3\sqrt{R/t}$, or 34.0. Consequently, SB1 would be expected to fail in shell buckling according to the DnV and CSA criteria. In the physical test, however, SB1 failed by general buckling and the maximum moment achieved was 89% of the plastic moment. Since the capacity associated with shell buckling is substantially lower than that for general buckling, it is apparent that the criterion used by the DnV and CSA is too conservative for the case of SB1.

In order to achieve a general buckling failure, the DnV and CSA rules allow a high s/t ratio for cylinders with large R/t values ($s/t < 3\sqrt{R/t}$). However, since the large R/t ratio reduces the bending stiffness of a shell panel and the stress distribution in such cylinders is relatively uniform, the tendency for shell buckling will increase. It would seem that cylinders with large R/t ratios should have a small s/t limit so that local shell buckling can be precluded.

2.3 Other Design Models

In addition to the design methods adopted in current design codes, the literature contains other design models for general instability of longitudinally stiffened steel

cylinders under axial compression. These models are essentially based on the orthotropic shell model or the equivalent column approach.

2.3.1 The Reduced Stiffness Method

Ellinas and Croll conducted a series of studies on stiffened cylinders under axial loading (Ellinas *et al.* 1981, Croll 1985). In the energy expression they established for the classical buckling of orthotropic cylinders, there is a term resulting from nonlinear hoop stress. From their early study on isotropic cylinders, they found that the reduction of buckling loads due to imperfections could be reflected by simply eliminating this energy term. This idea was then applied to stiffened cylinders to give a lower bound buckling load for imperfect cylinders. The approach was termed “reduced stiffness method”. In addition to the research described above for elastic buckling, Croll (1985) suggested a first yield criterion using the elastic instability stress from the reduced stiffness equation. Such a criterion provides a lower bound for inelastic failure.

2.3.2 The Equivalent Column Approach

The model proposed by Walker and Sridharan (1980) is that of a column supported on a set of lateral springs distributed along the column length. The column is composed of a stiffener and half of the shell panel on each side. The ends of the column are either pinned or clamped, as appropriate. The shell imperfections are represented by the initial deflection of the column. The springs represent the support provided by adjacent shells along the circumference. The elastic stiffness of springs is estimated by equating the elastic buckling stress of a continuous orthotropic shell to that of a stiffened curved panel. The failure of the equivalent column is identified by the first yield of the compressive stress, that is

$$\frac{P}{A_{col}} + \frac{M y}{I_{col}} = \sigma_y \quad (2.5)$$

In this equation, A_{col} and I_{col} are the cross-sectional properties of the equivalent column, y refers to the distance from the centroidal axis to the location of the maximum compressive stress, and M is the bending moment resulting from the lateral forces in the springs and the secondary effect (P – Δ effect).

2.4 Finite Element Analysis

Finite element procedures incorporating both the geometrical and material nonlinearities are capable of predicting the ultimate instability behavior of cylindrical shells. A number of sophisticated analyses have been reported in the literature. The effect of initial imperfections and residual stresses have been studied numerically by several investigators. The following is a brief review of the relevant literature.

2.4.1 Unstiffened Cylinders in Bending

Petrick (1985) performed an analysis of the two bending specimens, B1 and B2, tested by Stephens *et al.* (1982). One quarter of the cylinder was modeled by sixteen-noded shell elements. The study focused on the geometric imperfections, which were expressed as an eigenvector abstracted from measured imperfections, i.e.

$$U_0 = \xi_1 \Phi_1 \quad (2.6)$$

In Equation 2.6, U_0 is the imperfection in the finite element model and Φ_1 is the first eigenvector obtained from the elastic buckling analysis. The scaling factor ξ_1 is obtained from

$$\xi_1 = \frac{\Phi_1^T U_0^*}{\Phi_1^T \Phi_1} \quad (2.7)$$

in which U_0^* is the measured imperfection of test specimen. This approach was based on the work by Pinkney *et al.* (1983).

The characteristics of U_0^* are significantly different from those of Φ_1 , however. The local shell deflections in U_0^* are concentrated near the girth weld at the ends, whereas Φ_1 had the buckles near the midspan. As a result, the generated imperfections were extremely small ($\xi_1 = 0.004$ for B1 and 0.013 for B2). With these types of imperfections, the finite element model over-predicted the failure moment by 29% for B1 and 17% for B2. To make the numerical results match the test results, magnification factors of 6.3 and 4.0 had to be used for specimens B1 and B2, respectively. The investigator concluded that part of the discrepancy was attributable to the residual stresses, which were not included in the analysis.

2.4.2 Unstiffened Cylinders In Shear

A series of numerical studies on large diameter tubes under transverse shear have been reported by investigators at the University of Alberta (Mok and Elwi 1986, Roman and Elwi 1987, Obaia *et al.* 1991). These studies were conducted using the NISA program (Häfner *et al.* 1981, Stegmüller 1984). Mok and Elwi (1986) studied the effect of initial imperfections on the shear buckling load by using the first eigenvector. Significant discrepancy was found between the numerical analysis and the physical tests reported by Bailey and Kulak (1984). Roman and Elwi (1987) carried out an extensive study using a modified version of NISA which could simulate the cold-forming and seam weld residual stresses by the application of a fictitious temperature field. The imperfections incorporated into the numerical models were those measured from the test specimens. Their main conclusions were that the initial stiffness was essentially independent of imperfections and residual stresses, and that the cold-forming residual stresses were the most significant factor affecting the ultimate shear buckling strength. Obaia *et al.* (1991) further improved the finite element model by using a more accurate description of experimental boundary conditions. Satisfactory agreement was reached between the numerical and experimental results. The data base generated by the numerical analysis, together with the test data, was used in the development of the mechanical and empirical design models.

2.4.3 Longitudinally Stiffened Cylinders In Axial Compression

Chryssanthopoulos *et al.* (1991a) reported a numerical study on the imperfection sensitivity of longitudinally stiffened cylinders subjected to axial compression. The software employed was an in-house program developed at the Imperial College, London for stiffened plates and shells. Eight-node shell elements were used for the cylinder and spatial three-node beam elements for longitudinal stiffeners. The imperfections were described using Fourier series in both the longitudinal direction (x) and the circumferential direction (θ):

$$w_0 = \sum_k \sum_l \xi_{kl} \sin\left(\frac{k\pi x}{L}\right) \sin(l\theta + \phi_{kl}) \quad (2.8)$$

in which w_0 is the shell deflection relative to a reference surface, ξ_{kl} is the modal amplitude and ϕ_{kl} is the phase angle. The values of ξ_{kl} and ϕ_{kl} were determined by statistical analysis

(Chryssanthopoulos *et al.* 1991b) of the laboratory measurement of some small-scale specimens ($R = 160$ mm, $t = 0.63$ to 0.84 mm). For one particular specimen, the mean values and the standard variations of different waves (i.e. different k and l) were combined to demonstrate their effect on the buckling load. Compared to the model with the best-fit imperfections of the measured specimen, these different combinations resulted in a variation of between -9% to 6.9% of the failure load. Since the small-scale specimens were stress-relieved by heat treatment, residual stresses did not have to be considered in the numerical analysis.

2.5 Summary

Research into the stability behavior and load capacity of longitudinally stiffened steel cylinders subjected to bending appears to be inadequate. In fact, the test reported by Bailey and Kulak (1984) is the only large-scale bending test reported in the literature. So far, most of the experimental research in this field has been concentrated on the loading case of axial and radial compression, for which the compressive stress is uniform throughout the structure.

Research needs also exist for numerical study of stiffened cylinders in bending. Previous finite element investigations of unstiffened cylinders have concluded that the effects of initial imperfections and residual stresses are significant.

The current design guidelines assume, conservatively, that the bending capacity of a longitudinally stiffened steel cylinder is the same as its capacity in axial compression. However, the comparison with the test result of Bailey and Kulak shows that, in the case of the general buckling failure, existing design provisions underestimate the capacity by 25% .

Table 2.1 Dimensions of Specimen SB1^a

Radius R_{avg} (mm)	Shell Thickness		R_{avg} / t_1	Stiffener size $h \times b \times t$ (mm)	No. of Stiffeners	Stiffener Spacing s (mm)
	Test Segment t_1 (mm)	End Segment t_2 (mm)				
647.5	5.05	7.94	128	50.9x25.6x3.32	5	215

^a adapted from Bailey and Kulak (1984).

Table 2.2 Material Properties of Specimen SB1^a

Shell material		Stiffener
E (MPa)	σ_y (MPa)	σ_y (MPa)
203x10 ³	338	531

^a adapted from Bailey and Kulak (1984).

Table 2.3 Large-Scale Flexural Tests of Unstiffened Cylinders

Specimen	R (mm)	t (mm)	R/t (MPa)	σ_y (MPa)	M_u (kN·m)	M_p (kN·m)	M_u / M_p
B1 ^a	764.5	5.13	149	376	2143	4509	0.475
B2 ^a	761.7	3.43	222	306	1028	2436	0.422
B3 ^b	879.0	5.05	174	729	4253	11378	0.374

^a adapted from Stephens *et al.* (1982).

^b adapted from Bailey and Kulak (1984).

Table 2.4 Large-Scale Compression Tests of Longitudinally Stiffened Cylinders ^a

Specimen	R (mm)	t (mm)	R/t	Stiffener No.-b (mm) x t (mm)	σ_y (MPa)	ϵ_{rc} ^b (x10 ⁻⁶)	P_u / P_y
GU1	570	2	285	20-32 x 2	224	270	0.63
GU2	570	6	95	8-95 x 6	290	100	0.97
GU3	590	3	197	30-45 x 3	410	400	0.69 ^c

^a adapted from Green and Nelson (1982).

^b ϵ_{rc} = average compressive residual strain over the shell between stiffeners.

^c Premature failure due to the fracture of stiffener weld.

CHAPTER THREE

EXPERIMENTAL STUDY

3.1 General

The literature survey indicated that there is a lack of experimental data of large diameter longitudinally stiffened steel cylinders in bending. The test reported by Bailey and Kulak (1984), designated as SB1, appears to be the only one in this category. It is apparent that more experimental research is needed so that analytical predictions can be verified and design approaches can be established.

In the experimental phase of this investigation, four specimens, SB2, SB3a, SB3b, and SB4, were tested under pure bending moment. One specimen, SB3a, was reused as SB3b after the local shell buckles that occurred in the initial test were repaired and additional stiffeners were attached.

All test specimens were fabricated steel cylinders longitudinally stiffened over part of the circumference using hollow structural sections (HSS). The outside diameter of the cylinders was 1270 mm, which is about 1/3 to 1/2 of that encountered in practice. The test parameters include the radius to thickness ratio (R/t) of the cylinder, the spacing between the stiffeners, and the total angle of the cross-section covered by the stiffeners. The R/t ratio used was between 130 and 200. The number of stiffeners varied from three to eight.

This chapter gives a detailed description of the experimental program and the preparation of the test specimens. The material properties, initial imperfections, and residual stresses of the specimens are also examined. The experimental behavior of the stiffened cylinders is presented along with observational comments.

3.2 Test Specimens

3.2.1 Design and Fabrication

All specimens had the general configuration shown in Figure 3.1. Each was longitudinally stiffened on the outside of the shell in the compression zone. The cylinder consisted of three segments: a 1300 mm long test portion at the center, and two 768 mm

long thicker segments at the ends. The end segments were added to preclude local buckling near the end boundary due to nonuniform stress distribution. All three segments shared the same outside diameter and they were joined together by circumferential groove welding. The dimensions of the cylinders and the stiffeners were measured prior to the test and the mean values are listed in Table 3.1.

The cylinders were fabricated from hot-rolled steel plates (CSA G40.21 300W or 260G) by a local steel fabricator using its standard procedures. The steel plate was cold-rolled several times until the desired curvature was reached. The two edges of the plate were then joined and welded together by complete penetration groove welds. During this process, restraints against springback (the stretching of the plate to release the elastic deformation) were not used. Thus, the so-called locked-in stress, which exists when springback is not free, might not be present. After each specimen was delivered to the laboratory, light interior fixture frames were installed into both ends to maintain the circular shape of the cross-section.

Stiffeners with open cross-sections may buckle torsionally under compression. Such a buckling mode could interact with other failure modes and complicate the investigation. For this reason, rectangular HSS sections were chosen for stiffeners. They were attached to the cylinders by means of 5 mm intermittent fillet welds, each of which was 50 mm in length and separated by 100 mm intervals. The location of the intermittent fillet welds on a given stiffener alternated from side to side.

3.2.2 Material Properties

In order to determine the material properties of the cylindrical shells, coupons were cut from the same plate used for test specimens in an orientation parallel to the longitudinal axis of the cylinder. Coupons were prepared as specified in ASTM E8-89 (ASTM 1989) and tested in a 1000 kN capacity universal testing machine. The material properties from coupon tests are summarized in Table 3.2. The coupon test curves for the steel used in test segments are shown in Figure 3.2. All coupon tests identified a sharp yield point which is typical of hot-rolled structural steels. The ductility was in the range between 25 ~ 30%. A long yield plateau can be observed from the stress versus strain relationship of materials for SB2 and SB4. However, the curve of SB3a and SB3b does not have the same characteristic. Instead, there is a moderate hardening slope shortly after the yield stress is reached.

The stiffeners were made from CSA G40.21 350W steel. Because of the way in which HSS shapes are manufactured, residual stresses can be quite significant. The yield stress is raised due to cold-forming and may not be uniform along the cross-section. In order to assess the average value of material properties under compression, stub column specimens were prepared and tested in accordance with the guidelines of the Structural Stability Research Council (SSRC 1988). A typical stress versus strain behavior from the stub column tests is plotted in Figure 3.3. A nominal yield strength can be obtained using the 0.2% strain offset as specified in various standards (SSRC 1988, ASTM 1989). However, the average stress versus strain curve of these small size HSS are so severely affected by the residual stresses and the nonhomogeneous material properties that the nominal yield strength corresponding to the 0.2% strain offset is no longer meaningful. As an alternative, the yield point shown in Figure 3.3 is defined as the intersection between the extended elastic and strain-hardening lines. The stub column test curve can then be interpreted as a uniform, bi-linear elastic-plastic hardening material with axial residual stress present which caused yielding at an early stage. Test results from the HSS stub column tests are also included in Table 3.2.

3.2.3 Initial Imperfections

Analytical studies of axially loaded cylinders have indicated that initial geometric imperfections of stiffened cylinders are important in evaluating the capacity (Hutchinson and Koiter 1970, Byskov and Hutchinson 1977). In this study, specimens SB2 and SB3a were chosen as typical representatives for 5 mm and 3 mm thick specimens, respectively, and their initial imperfections were examined.

3.2.3.1 Measurement

The measuring device used for recording imperfections was similar to that used by Obaia *et al.* (1991). It consisted of an aluminium bar, a rod, and a linear variable differential transformer (LVDT). The aluminium bar could rotate around its axis, and its ends were supported at the centers of the interior frames located at each end of the specimen. The rod was arranged at right angles to the aluminum bar, i.e., in the radial direction from the bar to the tube. An LVDT was mounted on the end of the rod adjacent to the tube, while a trolley was attached to the other end. The trolley allowed the rod to move

longitudinally on the track of the aluminium bar. The LVDT output gave the difference between the inside shell wall and the reference circle drawn by the rotating LVDT head.

The imperfections were measured after the welding of stiffeners but before the tube was welded to the end plates which would attach it to the test set-up. A total of 192 points (12 cross-sections with 16 circumferential points at each section) were measured for each specimen. To ensure that the measured configuration coincides with that which would be present during the test, the specimens were suspended horizontally at their ends by a crane while the imperfections were being measured. This position is similar to that used subsequently in the test set-up.

3.2.3.2 Categories of Imperfections

The data from the measurement described above must be interpreted properly so that the three-dimensional profile of the imperfect cylinder can be recreated. As a first step, different forms of imperfections need to be classified. Since a perfect cylinder can be characterized by its straight longitudinal axis, uniform radii along the length, and a perfectly round shape for every cross-section, the imperfections in a cylinder can be classified into the following categories (Figure 3.4).

(a) Out-of-straightness

This occurs when the longitudinal axis of the cylinder is not a straight line (Figure 3.4(a)). This type of imperfection is largely attributed to the deflection under the gravity load when the cylinder is in a horizontal position.

(b) Variation of radii

The nonuniform radii of cross-sections along the length defines this type of imperfection (Figure 3.4(b)). This likely is caused by the shrinkage of circumferential welds as successive segments of the tube are joined.

(c) Out-of-roundness

Out-of-roundness is defined as the deviation of the shell wall from a perfectly round cross-section (Figure 3.4(c)). Imperfections of this type may be important for both local buckling and general buckling.

In this study, the classification system outlined above was employed in the examination and numerical modeling of imperfections.

3.2.3.3 Analysis of Data

The measurements described in Section 3.2.3.1 located points relative to a reference cylindrical surface which is determined by the measuring device. However, it is difficult to make the axis of the measuring device coincident with the axis of the specimen. In fact, both these axes are not straight lines because they deflect under gravity load. Therefore, the reference cylindrical surface can not be used as a perfect cylinder and the raw data does not represent the real imperfections. Such errors must be eliminated during data analysis.

In the procedure established during this study, a best fit circle is found by the least squares method at each cross-section. The centers of these circles form the axis of the imperfect cylinder. The perfect reference cylinder, which is used to define imperfections, has the average radius and a straight axis connecting the two end cross-sections. Relative to the perfect reference cylinder, the radii of the best fit circles describe Type (b) imperfections (variation of radii), while the axis of the imperfect cylinder defines Type (a) imperfections (out-of-straightness). Consequently, Type (c) imperfections (out-of-roundness) are given at each cross-section by the deviation of the measured profile from the best fit circle.

Based on the procedure outlined above, two computer programs called IGI (Implementation of Geometric Imperfections) were developed. Program IGI1 processes the measured data, while IGI2 prepares the imperfections for the finite element models. A short description and the source code of programs IGI1 and IGI2 are included in the Appendix.

A summary of the results of the data analysis for specimens SB2 and SB3a is presented in Table 3.3. As can be seen from the table, the initial deviation of the central axis and the change of the radius are not significant for such short cylinders, and the initial shell deviation is in the order of wall thickness. The results also showed that the two specimens had similar imperfection patterns, with the thinner one (SB3a) having the more severe imperfections. The minus sign in the table denotes downward deflection of the

centroidal axis for Type (a) imperfections, shrinkage of the radius for Type (b) imperfections, and the inward shell deflection for Type (c) imperfections.

The recreated initial profiles of specimens SB2 and SB3a are plotted in Figures 3.5 and 3.6. Throughout this thesis, the scaling factor of displacements for finite element mesh plots is expressed by a . The imperfections in Figures 3.5 and 3.6 are scaled by a factor of 30. The deflection of the axis and the shrinkage due to girth weld can be seen from the side view plot. The pear shape of the cross-section could be attributed to the residual deformation due to the seam weld as well as the cold-forming process, in which the curvature applied might not be exactly uniform throughout the plate. The part away from the edges was over-rolled and, consequently, had a relatively large curvature. The interior fixture frames located at the cylinder ends helped to overcome the ovalization due to the self weight of the tube. Such an imperfection pattern agrees with the report of Dwight (1982) in which three offshore cylinders ($R = 7300 \sim 9200$ mm, $t = 16 \sim 40$ mm) were measured. In addition to the pear shape, the longitudinal weld underneath the stiffeners introduced circumferential waves in the local area.

3.2.4 Residual Stresses

3.2.4.1 Sources of Residual Stresses

In a stiffened steel cylinder, there are various types of residual stresses introduced during the fabrication process. The sources of residual stresses include:

(a) Cold forming

The rolling of a steel plate into a tube is a repetitive process of applying successive inelastic bending deformation to the plate and then unloading elastically. Circumferential residual stresses are induced in such a process. However, if springback is not restrained, which is considered to be the case for specimens fabricated for these tests, the amount of these residual stresses is reduced considerably.

(b) Longitudinal seam welding

The longitudinal residual stress caused by seam welding is concentrated in the vicinity of the weld (Chen and Han 1985). In this test program, the cylinders were arranged such that the seam was located at the middepth, near the neutral axis.

Consequently, the influence of seam welding on either the compression or the tension zone was minimized.

(c) Circumferential girth welding

There were four circumferential welds in each specimen: two performed by the fabricator to join the segments, and the other two attaching the ends of the specimen to the test set-up. The residual strains resulting from the end welds were measured using strain gages and results showed that a strain of about 40×10^{-6} existed in the test portion of cylinder SB2. However, information on residual strains resulting from the two shop welds was not available. The residual stresses that arise from this particular source are present mainly in the circumferential direction. The distribution is localized near the girth weld.

(d) Welding of Stiffeners

Welding of the longitudinal stiffeners to the shell produces longitudinal compressive residual stress near the welds. It is considered to be a major source of residual stresses in the compression zone of a stiffened cylinder, where local shell buckling may be promoted. As reported by other investigators (Green and Nelson 1982), the distribution of compressive residual stresses in the panels between the stiffeners is nearly uniform. Its average value varies mainly according to the shell thickness and the size of welds. The tensile residual stress in the immediate vicinity of the welds is much higher than the equilibrium compressive residual stress.

The combined residual stresses from the above sources are not necessarily equal to the summation of all distributions. In fact, some later processes, such as the welding of stiffeners, may eliminate part of the earlier distribution because of the large amount of heat input.

3.2.4.2 Residual Stresses from Stiffener Welding

The longitudinal residual stress resulting from the welding of stiffeners was measured only for specimens SB2 and SB3a as they represented the 5 mm and 3 mm thick cylinders, respectively. The intensive measurement of SB2, by Demec gages as well as strain gages, was aimed at collecting data for the residual stress distribution. These strain gages were mounted on the inner surface of the cylinder wall, while the Demec gage marks were punched on the outer surface at a gage length of 51 mm.

The residual stress results from SB2 (Figure 3.7) show that the distribution pattern of compressive residual stresses agrees with the description of Green and Nelson (1982). The average compressive residual strain was about 35% of the yield strain (ϵ_y) in the internal panels between stiffeners and about 15% of ϵ_y in the shell outside the stiffened area.

The measurements for SB3a were concerned merely with the magnitude and only strain gages were used. Compared with SB2, a higher compressive residual stress level was observed in this thinner shell, even though the welding was very similar to that of SB2. The average compressive residual strain was about 55% in the panels between the stiffeners and about 30% of ϵ_y in the shell outside the stiffened area.

Since residual stresses came from many sources, the measured level reflected only the change of residual stresses due to the welding of stiffeners, rather than the total residual stresses in the specimen, even though the measured data represent the dominant residual stresses in the compression zone.

Using the measured strains, the corresponding longitudinal residual stresses can be calculated by assuming that the shell is in a state of plane stress and is free to expand and shrink circumferentially. Thus,

$$\sigma_\theta = 0 \quad \text{and} \quad \sigma_z = E \epsilon_z \quad (3.1)$$

The subscripts z and θ refer to the longitudinal and circumferential directions, respectively. ϵ_z is the measured longitudinal residual strain.

3.3. Test Program

3.3.1 Test Set-Up

The test set-up used in these tests was similar to that used in earlier experiments in the University of Alberta program (Stephens *et al.* 1982, Bailey and Kulak 1984). As shown in Figure 3.8, it consists of two major parts: a large composite beam and a loading frame.

3.3.1.1 Composite Beam

The composite beam (Figure 3.9) consisted of two end trusses and a test specimen

in the center. The test region was subjected to pure bending under a two-point loading system. The ends of the specimen were expected to remain plane during bending because they were welded to the heavily stiffened base plates of the end trusses. Each end truss consisted of two parallel plane truss elements interconnected by short I-shapes. The chords of the plane trusses were welded wide-flange shapes and the web members were channel sections. They were assembled using A325 bolts.

The composite beam was simply supported at both ends, with horizontal translation allowed only at one end. There were two separate supports at each end, one for each plane truss. Every support consisted of a knife edge and a set of rollers. After the trusses had been positioned, the rollers at one end were restrained while those at the other end remained movable.

3.3.1.2 Loading System

The load was applied by means of two 2220 kN hydraulic jacks which were controlled by an air pump. By balancing the pressure valves of two outlets in the pump, the two jacks could maintain the same load level.

The jacks were simply supported between the loading frame and the composite beam. During the test, the horizontal rollers above the jacks enabled them to move with the loading points. A spherical device below the jack was present to allow for possible rotations. The jack load was transferred to the plane trusses through a distributing beam.

3.3.2 Instrumentation

3.3.2.1 Measurement of the Applied Load

Since the load was applied through a temporarily assembled system, not a standard testing machine, an accurate measurement of loads and reactions was emphasized in the design of instrumentation. The applied load was measured using two 2200 kN load cells under each loading jack. To check the uniformity of the reactions, the supporting force underneath each plane truss was measured individually. Two 900 kN and two 1300 kN load cells were distributed at the four supports under the composite beam. All the load cells

were calibrated prior to the test. The output of the six load cells were zeroed before the specimens were loaded. During the tests, the discrepancy between the loads and the reactions was within 3%.

The applied moment was calculated according to the average of the load cell readings. However, the total moment should also include the amount caused by the gravity load, which in this case contributes a large percentage to the total moment. In order to determine this portion of load, the end trusses were weighed by load cells and their centers of mass were located. It was found that each end truss had a weight of 62.3 kN and the center of mass was 2.99 m away from the end support. This resulted in a bending moment of 186.3 kN·m at the test specimen. When the weight of the specimen itself was included, the 5 mm thick cylinder (SB2) had a moment of 204 kN·m before testing, and the 3 mm thick cylinders (SB3a, SB3b and SB4) had a moment of 202 kN·m.

3.3.2.2 Measurement of Displacement and Strain

The displacements at various locations were measured using LVDT's, cable transducers and dial gauges. All of the LVDT's and cable transducers were calibrated before the installation. Deflections at three cross-sections were measured by cable transducers above and beneath the specimen, as shown in Figure 3.10. At the same cross-sections, LVDT's on both sides recorded the horizontal displacements.

The rotation of the test segment was obtained in two ways. First, rotation meters were mounted at both ends of the test segment to measure the change of the angles (Figure 3.10). The second approach was to calculate the angle from the relative translations at the top and the bottom. These translations were measured by LVDT's (Figure 3.10a).

Eight dial gauges were used to check that the base plates between the specimen and the trusses remained plane during deformation. All dial gauges were installed in the same plane so that any deviation from a plane would be detected. Several other dial gauges on the loading frame monitored the lateral movement of the trusses.

Fifty strain gages were mounted on the specimen. They formed three rings at the same cross-section as deflections were measured (Figure 3.10). Most of these gages were in the longitudinal direction except five which were mounted circumferentially on the

compression side of the central cross-section. Because of different arrangements of the stiffeners, the locations of the gages varied slightly among the specimens.

3.3.3 Test Procedure

After the trusses had been assembled, the base plates were carefully shimmed into a plane before the bolts were finally tightened. Then the specimen was positioned and welded to the plates using a partial penetration groove weld. The alignment of the end trusses, the specimen and the loading jacks was checked both before and after the welding. In order to observe the yielding and buckling pattern, the specimen was whitewashed before testing. A preliminary run up to 30% of the estimated failure load was carried out before each test in order to check for any defects in the set-up and the instrumentation.

Loads, displacements and strains were measured throughout the duration of every test. The electronic measuring devices were connected to a Fluke data acquisition system driven by a microcomputer. The load increment started at 5% of the estimated failure load, but this was decreased as the moment versus curvature behavior changed. All the data was scanned and recorded after each load increment. Dial gauge readings were taken at greater intervals.

During the test, the behavior of the composite beam was monitored by dial gauges. Lateral translation of the trusses was negligible and ceased completely after a few load steps. The out-of-plane displacement of the base plate was a maximum of 1.6 mm in the tension area of SB2. After reinforcing the connection by adding four additional bolts, this amount decreased to less than 0.4 mm in subsequent tests.

The uniformity of the four reactions was checked frequently during the test. Maintaining such a uniformity, however, was a problem in the test of SB2: the reaction in some supports was 20% different from the average. It was found later that some bolts in the trusses had become loose during the preliminary run. This significantly changed the shear stiffness of the plane trusses and, consequently, made the reactions uneven. By ensuring that all the bolts were in proper tightness, the nonuniformity of reactions was kept less than 6% from the average in the subsequent tests.

3.4 Test Results

3.4.1 Specimen SB2

The test segment of this specimen was a 4.72 mm thick cylinder with three HSS 50.8 x 25.4 x 3.18 stiffeners spaced at 180 mm covering an angle of 32° in the compression zone. Considering the presence of compressive residual stresses, yield was anticipated at a moment of 1414 kN·m. The calculated plastic moment was 2659 kN·m, based on measured dimensions and yield stress. In the test, specimen SB2 failed by local buckling in the shell outside the stiffened area.

The moment versus curvature response of specimen SB2 is plotted in Figure 3.11. The linear portion agrees well with the elastic beam theory. The yield in the shell between stiffeners, which only accounted for a small area in the compression zone, did not have any significant nonlinear effect on the measured rotations.

The change of the behavior near the ultimate point was sudden. At a bending moment of 1888 kN·m, yield lines at 45° appeared on the whitewashed shell surface in the compression zone. This occurred in the shell outside the stiffened area and near the circumferential weld joining the central and the end segments. During the load increment toward 1947 kN·m, the flaking of the whitewash signaled local shell buckling near the location of previous yielding. At this time, the strain gage readings indicated a large increment of deformation throughout the whole compression zone, which was confirmed by the observation of several shell buckles immediately after the first buckle. The ultimate moment of 1947 kN·m is about 73% of the theoretical plastic moment. Stiffeners remained straight until the ultimate point was reached, but finally bent with the shell at the post-peak stage. The behavior after the ultimate load point was stable. Figure 3.11 shows that large rotations took place with only a small decrease in moment. The buckled shape of the specimen is shown in Figure 3.12.

The strain distribution of the central cross-section at various load stages is presented in Figure 3.13. The elastic strains at $M = 773$ kN·m show that the cross-section remained a plane. The neutral axis at this moment was close to the position predicted by elastic beam theory (41 mm above the center of the circle). At high load levels, however, the nonlinear inelastic shell deformation deviated from the plane

assumption. After the ultimate moment was reached, the neutral axis shifted downwards as the buckled area extended towards the middepth of the cross-section.

3.4.2 Specimen SB3a

Specimen SB3a had five HSS 25.4 x 25.4 x 2.54 stiffeners on its 3.07 mm thick steel cylinder. These stiffeners were spaced at 175 mm and covered an angle of 64° . Using measured material properties and residual stresses, the predicted yield moment is 518 kN·m and the fully plastic moment is 1475 kN·m.

The moment versus curvature behavior of this specimen is presented in Figure 3.14, where the curvature was computed from both the rotation meters and the LVDT's. The response was linear up to about 660 kN·m, at which time yielding spread over the compression area. The departure of the LVDT curve from the rotation meter curve indicated that the cross-section was no longer a plane. This can also be seen from the strain distribution plotted in Figure 3.15.

The failure mode of SB3a was similar to that of SB2: the ultimate load capacity was controlled by shell buckling outside the stiffened region. As shown in Figure 3.16, local shell buckling was first identified by strain gages at various locations outside the stiffened region when the moment was 1110 kN·m. The buckling waves spread over the whole length of the testing segment as indicated by strain gages at different cross-sections. At a moment of 1120 kN·m, several shell buckles and yield lines were observed. These buckles were close to the circumferential welds, and those outside stiffened area were much longer and deeper than those between stiffeners. With the development of deformation, the load started to drop after reaching an ultimate moment of 1138 kN·m, which is about 77% of the plastic moment.

The buckling deformation was not severe at ultimate. Based on the observation of the previous test, continuing the experiment would only have provided a stable post-peak behavior like that of SB2. As an alternative, it was decided to stop the test and unload the specimen so that the cylinder could be modified and retested.

3.4.3 Specimen SB3b

As discussed, SB3b was the reuse of cylinder SB3a. The two major shell buckles that were presented in SB3a were pulled out and two additional stiffeners were welded to the shell. The size and spacing of the new stiffeners were the same as that of existing stiffeners. Altogether, there were now seven stiffeners, and they covered 95° of the circumference.

The specimen failed at 1333 kN·m, having reached 87% of the fully plastic moment (1524 kN·m). The observed failure mode was so-called general buckling, in which the stiffeners buckle together with the adjacent portion of the shell.

Yield lines first appeared at 1129 kN·m, and the first new buckle occurred at 1234 kN·m in the panel next to the central stiffener. As the load increased, shell buckles in the top panels extended rapidly from the circumferential welds towards the center, while the old buckles from SB3a outside the stiffened area remained unchanged. The difference between the top and the bottom deflection, as shown in Figure 3.17, indicated that buckling of the central stiffener started at about 1200 kN·m. Bending and yielding of five central stiffeners was observed near the ultimate load point (1333 kN·m). The strain distribution of the central cross-section, plotted in Figure 3.18, shows that a substantial inelastic tensile deformation developed before the failure. After passing the peak point, shell buckles extended to the unstiffened area. As shown in Figures 3.19 and 3.20, the whole compression zone was buckled by the time the test was stopped. On the other side of the cylinder, tensile yield lines could be seen at the bottom of the specimen.

As shown by the moment versus curvature graph in Figure 3.21, there was still a large increase in applied load after the initiation of buckling. This behavior is significantly different from the shell buckling failure of specimens SB2 and SB3a, in which shell buckling outside the stiffened area led to an abrupt failure.

3.4.4 Specimen SB4

Specimen SB4 used eight HSS 25.4 x 25.4 x 2.54 sections to stiffen its 3.34 mm thick cylinder. The stiffeners were spaced at 140 mm and covered a total angle of 89° . Assuming that the compressive residual stress was equal to that measured in SB3a,

the predicted yield moment was 730 kN·m. The fully plastic moment for SB4 was 1970 kN·m.

According to the strain gages located between the stiffeners (Figure 3.22), compressive yield occurred at 750 kN·m and it took place throughout the whole length of the test segment. Such a large volume of yielded shell reduced the stiffness considerably, as can be seen from the change of slopes of the curves in Figure 3.22. The yield moment agreed well with the predicted value.

Specimen SB4 also failed in general buckling similarly to SB3b. The first local buckle was observed at the panel of extreme compressive area when the load was 1308 kN·m. These deformations developed slowly before new yield lines and buckles appeared at about 1500 kN·m. The stiffeners bent slowly with the shell surface until the ultimate moment was reached. Yielding of the tension zone was indicated by strain gage readings at a moment of about 1600 kN·m. At 1800 kN·m, 45° yield lines were observed at the bottom of the cylinder. As the load approached and passed the ultimate point, buckling at the top and yielding at the bottom proceeded rapidly. The ultimate moment reached was 1857 kN·m, or 94% of the plastic moment.

The moment versus curvature graph for SB4, shown in Figure 3.23, illustrates how its behavior differed from the shell buckling failure of SB2 and SB3a. The development of deformation was slow and gradual, even though nonlinearity started early because of the yielding around the welding of stiffeners. The load increased significantly after the shell and the stiffeners buckled.

The strain distribution at the central cross-section is illustrated in Figure 3.24 for different loading levels. The upward migration of the neutral axis indicates there was a substantial stress redistribution after the initial buckling in the compression zone. At the time of failure, nearly all material below the center of the cylinder had yielded. Meanwhile, the deformed shape in Figure 3.25 shows that buckling waves covered the compression zone. The capacity of the full cross-section was nearly exhausted.

3.5 Summary

Four fabricated large diameter steel cylinders, reinforced by longitudinal stiffeners, were tested under pure bending moment. The test results are summarized in Table 3.4,

wherein the ultimate moment is compared with the plastic moment of the stiffened cross-section. The experimental study has led to the following conclusions:

- (1) The initial imperfections of the specimens, exclusive of the ovalization, were moderate. The 3 mm thick cylinder had more severe imperfections as compared with the 5 mm thick shell.
- (2) Significant compressive residual stress was introduced by the process of welding the stiffeners. The measurement of the two specimens showed that a higher residual stress level existed in the thinner shell.
- (3) Behavior in the elastic stage can be predicted adequately by one-dimensional beam theory. However, substantial nonlinear deformation was observed after yielding.
- (4) Even though large buckles were observed near the circumferential welds, strain gage readings showed that buckling occurred simultaneously throughout the whole length of the test section. The deformation was large near the welds because of the initial imperfections and, probably, residual stresses caused by the circumferential girth welding.
- (5) The failure of SB2 and SB3a occurred suddenly when shell buckling occurred outside the stiffened region. However, the post ultimate behavior was stable. The moment capacity was lower than had a general buckling failure occurred, but still much higher than that of an unstiffened cylinder.
- (6) Specimens SB3b and SB4 failed in general buckling when the stiffeners buckled gradually with the shell. The ultimate moment was close to the plastic moment.

Table 3.1 Dimensions of Test Specimens

Specimen	Radius	Shell Thickness		R_{avg}/t_1	Stiffener	No. of	Stiffener
	R_{avg}	t_1^a	t_2^b		$h \times b \times t$	Stiffeners	Spacing
	(mm)	(mm)	(mm)		(mm)		s (mm)
SB2	629.8	4.72	7.94	133	50.7 x 25.3 x 3.04	3	180
SB3a	631.5	3.07	6.23	206	25.4 x 25.4 x 2.38	5	175
SB3b	631.5	3.07	6.23	206	25.4 x 25.4 x 2.38	7	175
SB4	631.2	3.34	6.47	189	25.5 x 25.5 x 2.33	8	140

^a Thickness of the test segment.

^b Thickness of the end segments.

Table 3.2 Material Properties

Specimen	Cylinder Material				Stiffener	
	Testing Segment		End Segments		E	σ_y
	E ^a	σ_y^b	E	σ_y		
SB2	210 x 10 ³	303	199 x 10 ³	248	209 x 10 ³	483
SB3a; SB3b	204 x 10 ³	244	207 x 10 ³	290	214 x 10 ³	512
SB4	207 x 10 ³	298	210 x 10 ³	305	193 x 10 ³	492

^a Young's modulus (MPa).

^b Static yield stress (MPa).

Table 3.3 Maximum Magnitude of Initial Imperfections

Specimen	Type (a) (mm)	Type (b) (mm)	Type (c) (mm)
SB2	-0.8	-0.6, +0.4	-3.7, +4.9
SB3a	-0.6	-0.9, +0.5	-5.2, +6.7

Table 3.4 Test Results

Specimen	M_u (kN·m)	M_p^a (kN·m)	M_u / M_p	Failure mode
SB2	1947	2659	0.73	Shell buckling outside stiffened area
SB3a	1138	1475	0.77	Shell buckling outside stiffened area
SB3b	1333	1524	0.87	General buckling
SB4	1857	1970	0.94	General buckling

^a Plastic moment is calculated using the measured dimensions and material properties.
The effect of the stiffeners is included.

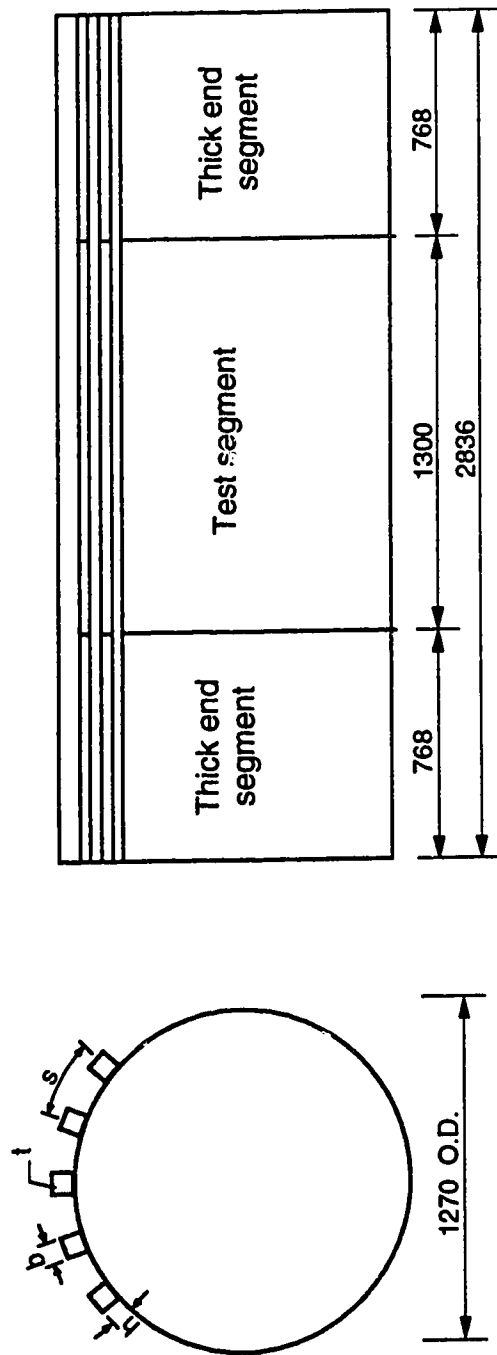
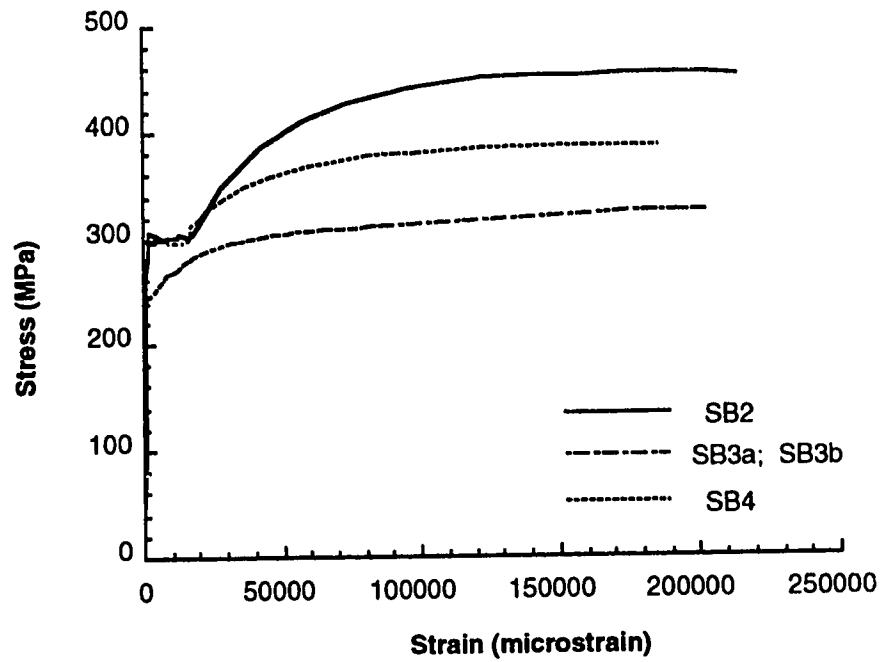
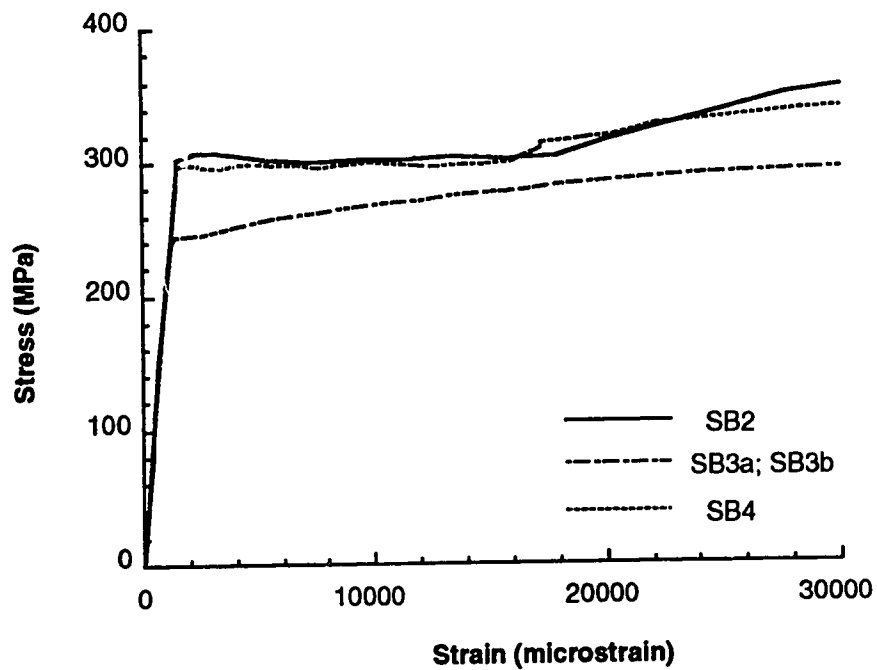


Figure 3.1 Schematic of test specimens (dimensions in mm)



(a) Full range



(b) Near the yield point

Figure 3.2 Tensile coupon tests for cylinder material

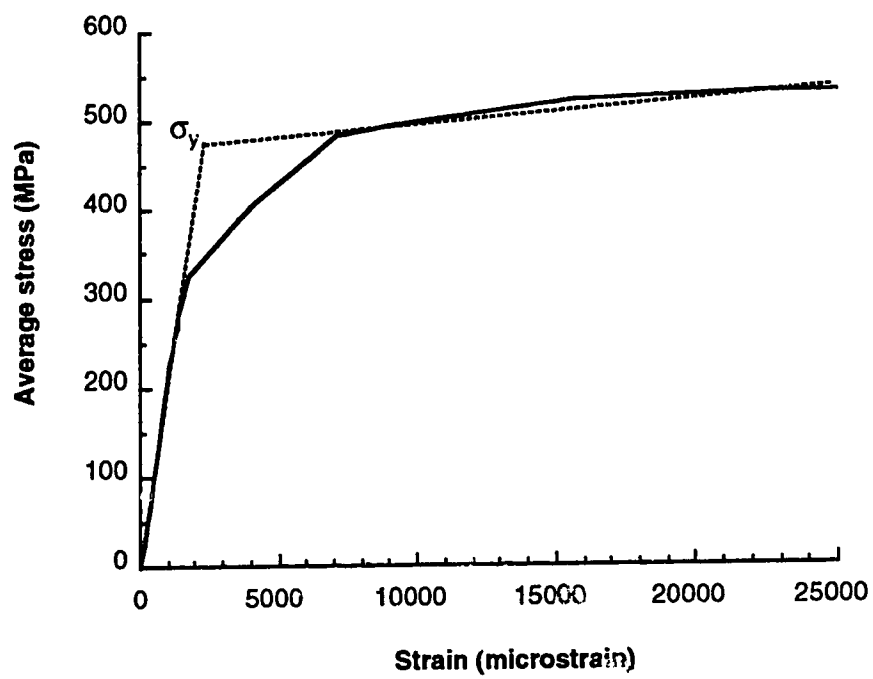
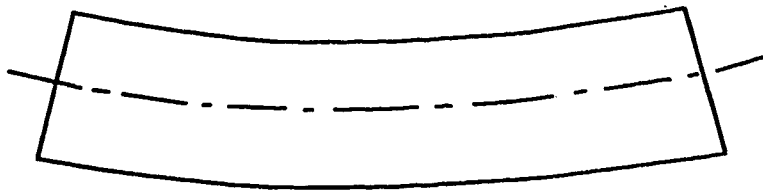
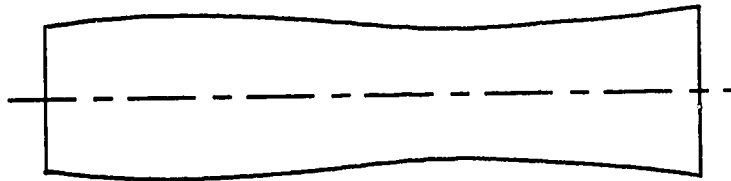


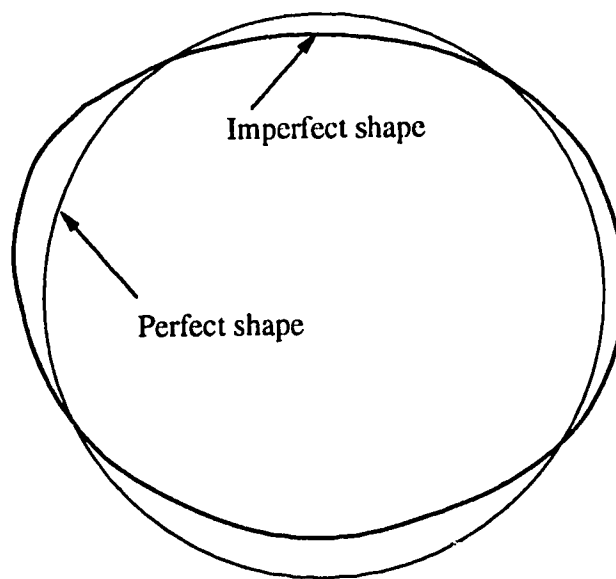
Figure 3.3 Stub column test of the HSS stiffener (specimen SB2)



Type (a): out-of-straightness

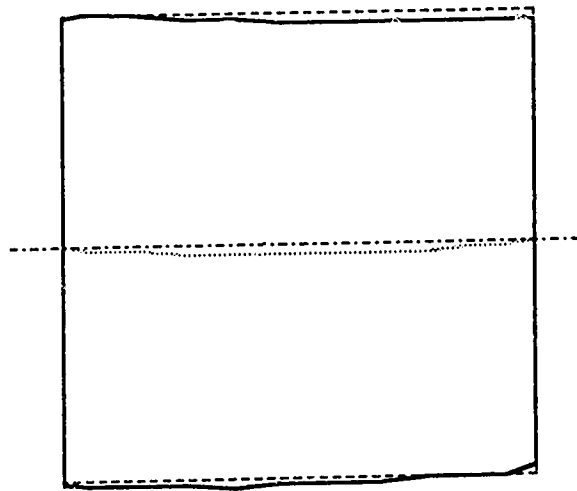


Type (b): variation of radii

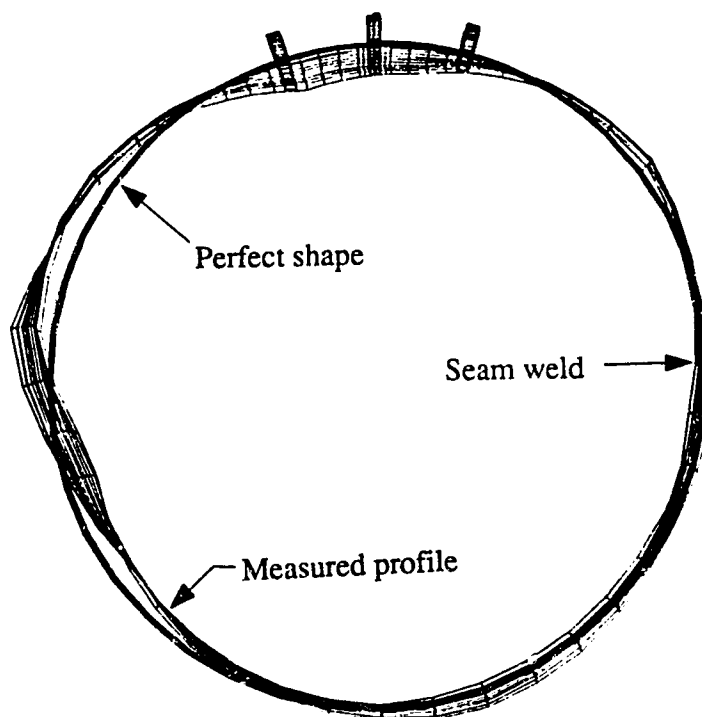


Type (c): out-of-roundness

Figure 3.4 Categories of initial imperfections

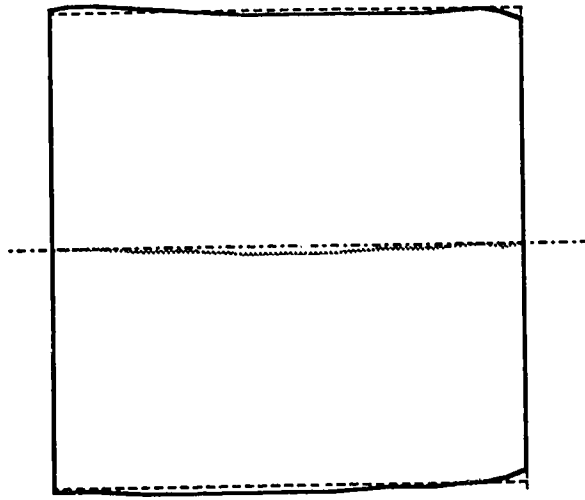


(a) Side view

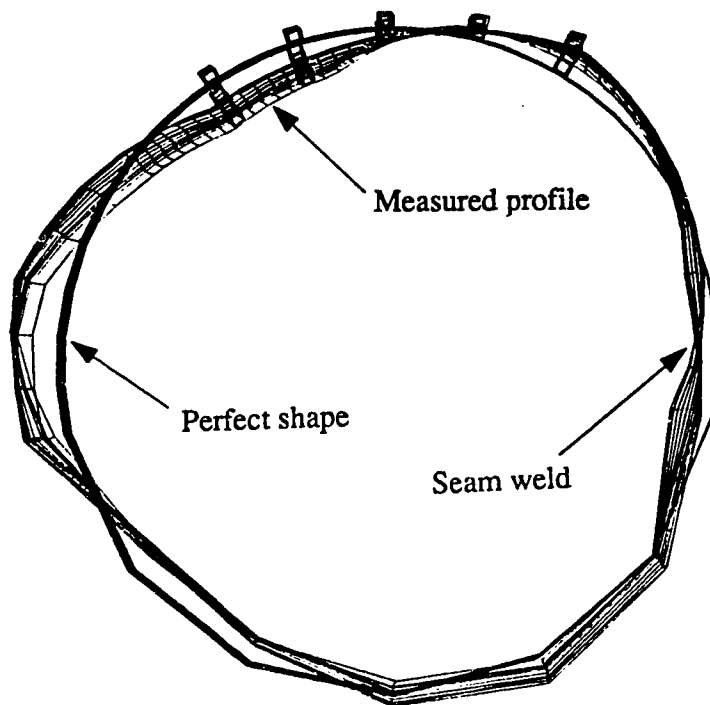


(b) Cross-sectional view

Figure 3.5 Specimen SB2: measured initial imperfections ($a = 30$)

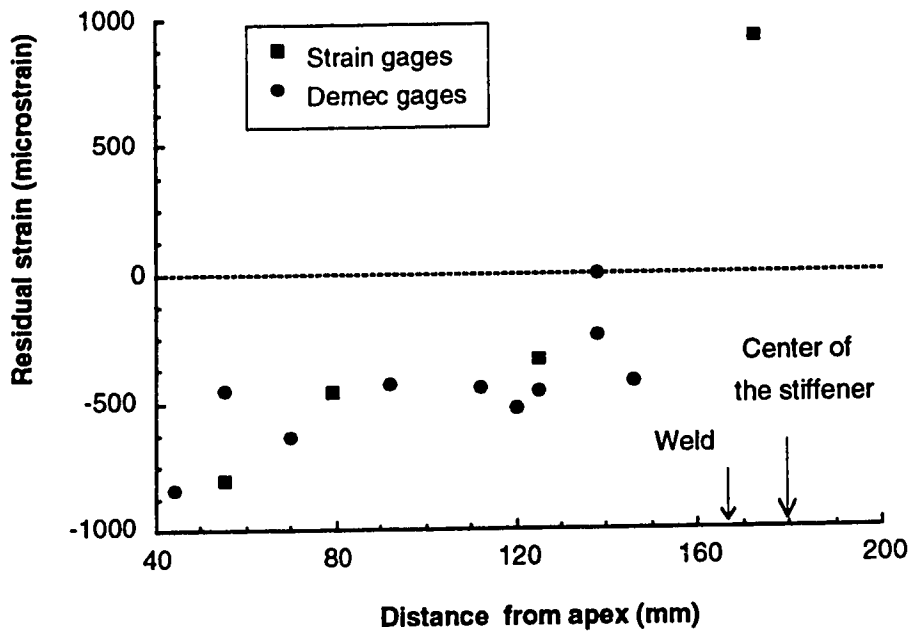


(a) Side view

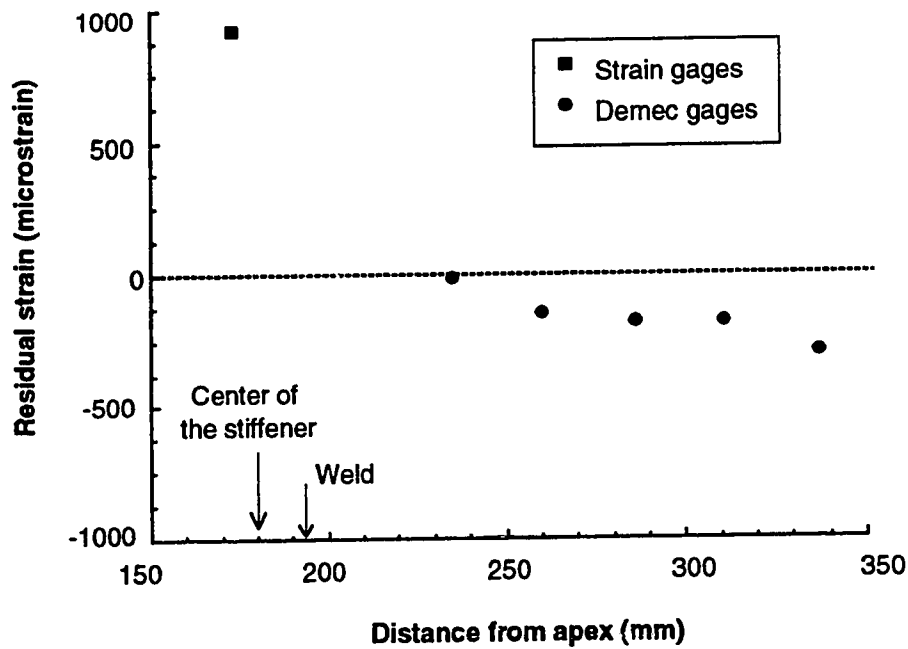


(b) Cross-sectional view

Figure 3.6 Specimen SB3a: measured initial imperfections ($a = 30$)



(a) In the shell between stiffeners



(b) In the shell outside the stiffened area

Figure 3.7 Specimen SB2: measured residual strains

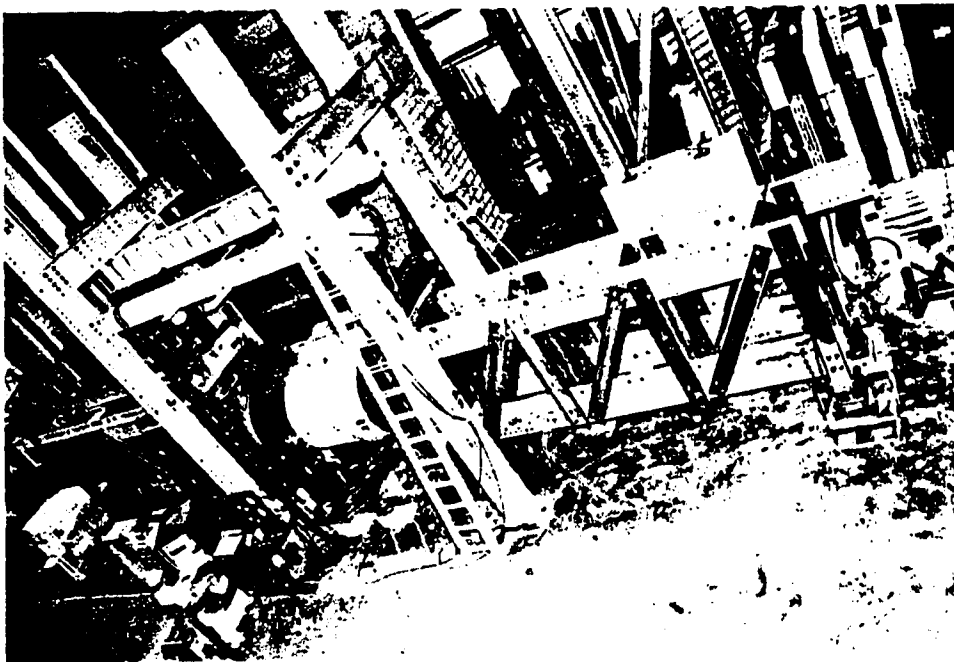
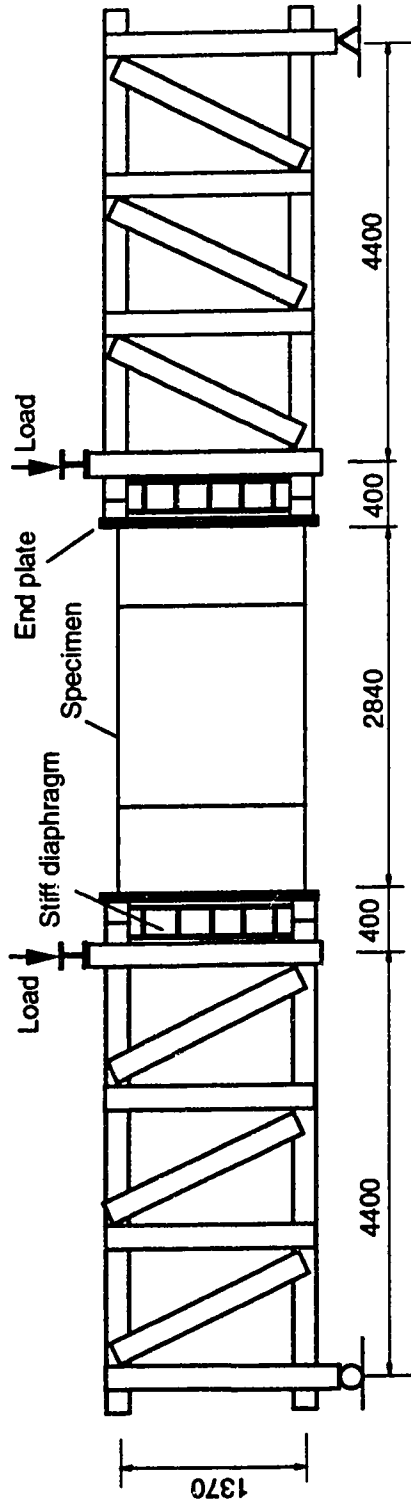
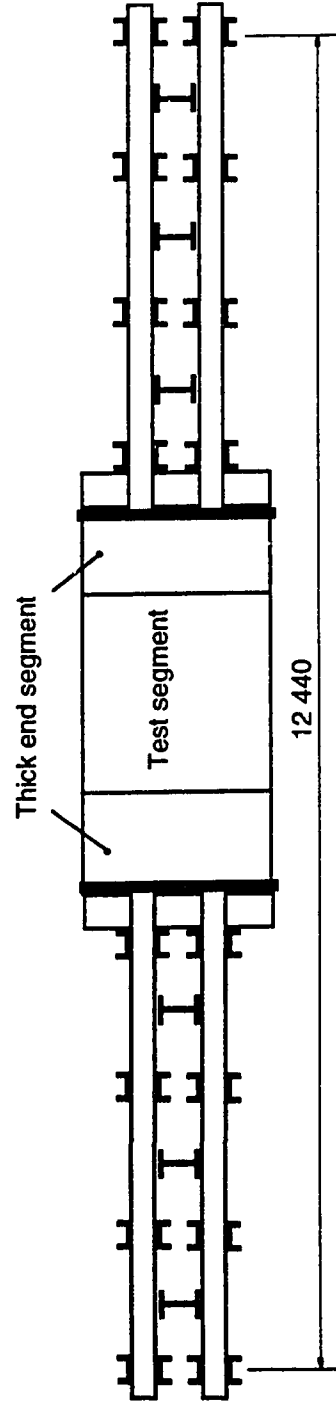


Figure 3.8 Test set-up: overview

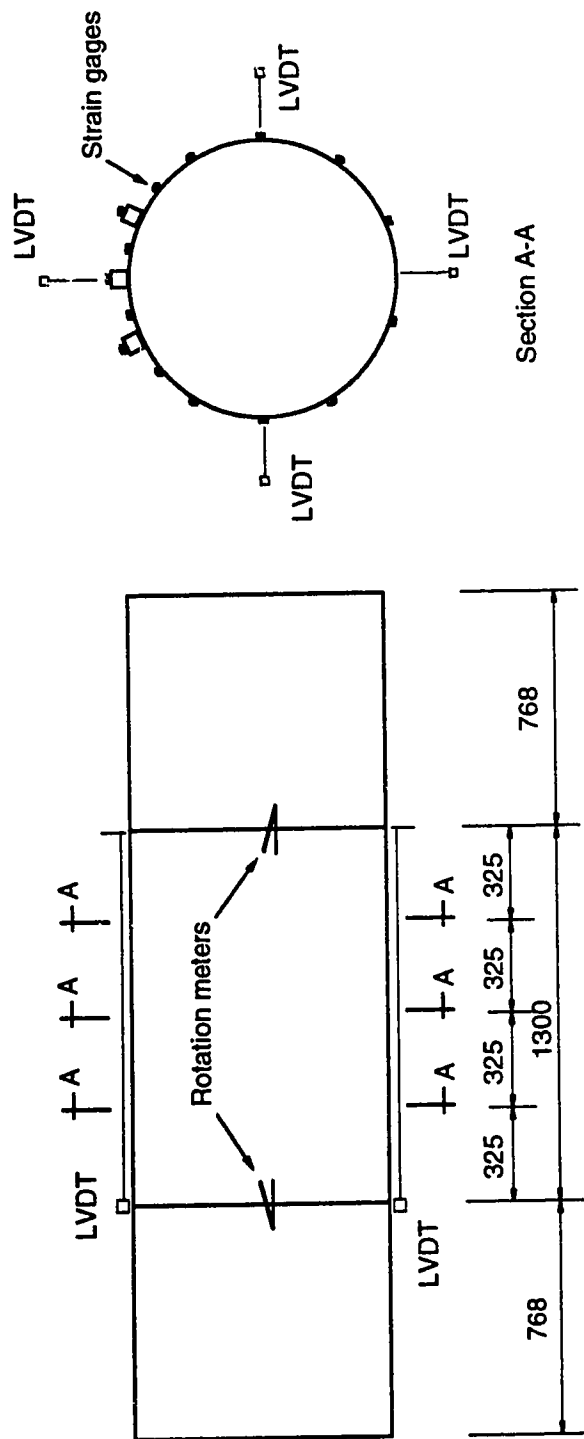


(a) Elevation view



(b) Plan view

Figure 3.9 Test set-up: the composite beam (dimensions in mm)



(a) Rotation meters and LVDT's

(b) Strain gages and LVDT's

Figure 3.10 Instrumentation: measurement for displacement and strain
(dimensions in mm)

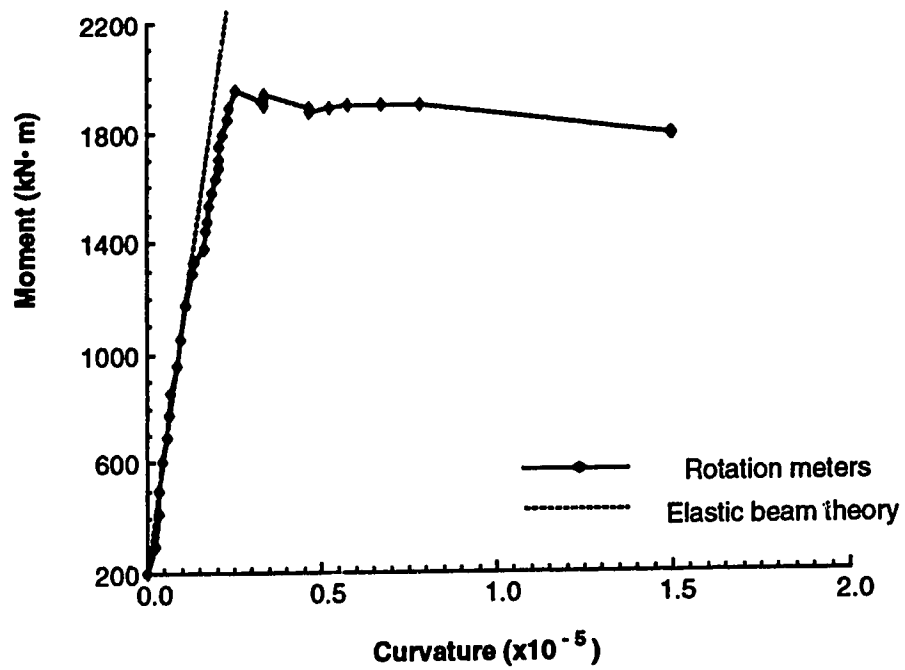


Figure 3.11 Specimen SB2: moment versus curvature response



Figure 3.12 Specimen SB2: deformed shape

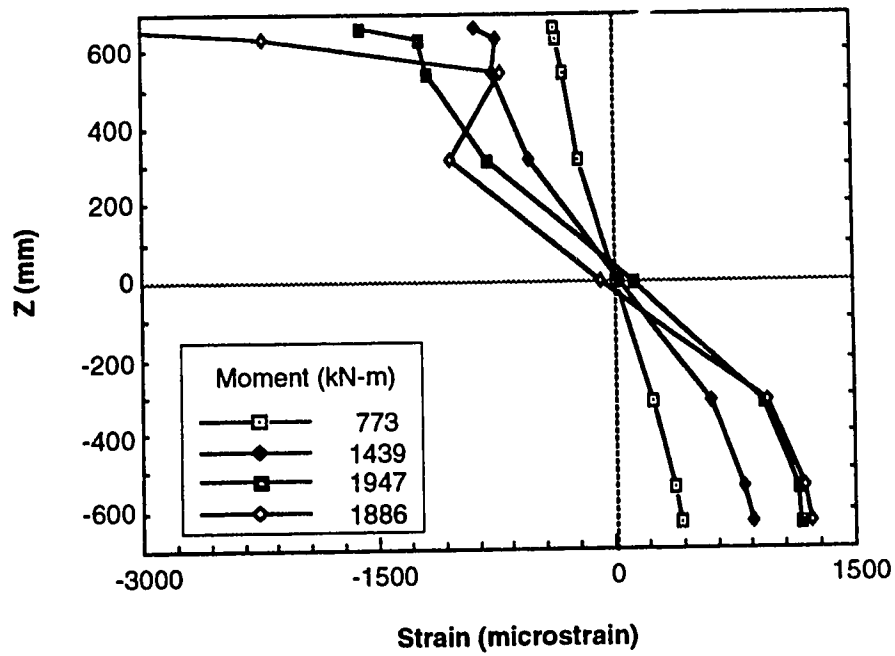


Figure 3.13 Specimen SB2: strain distribution

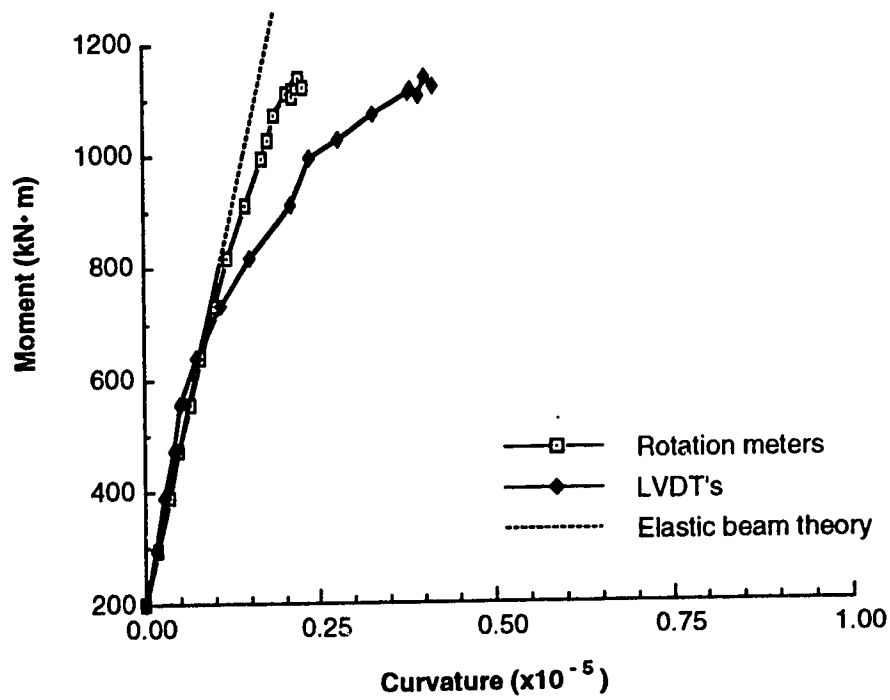


Figure 3.14 Specimen SB3a: moment versus curvature response

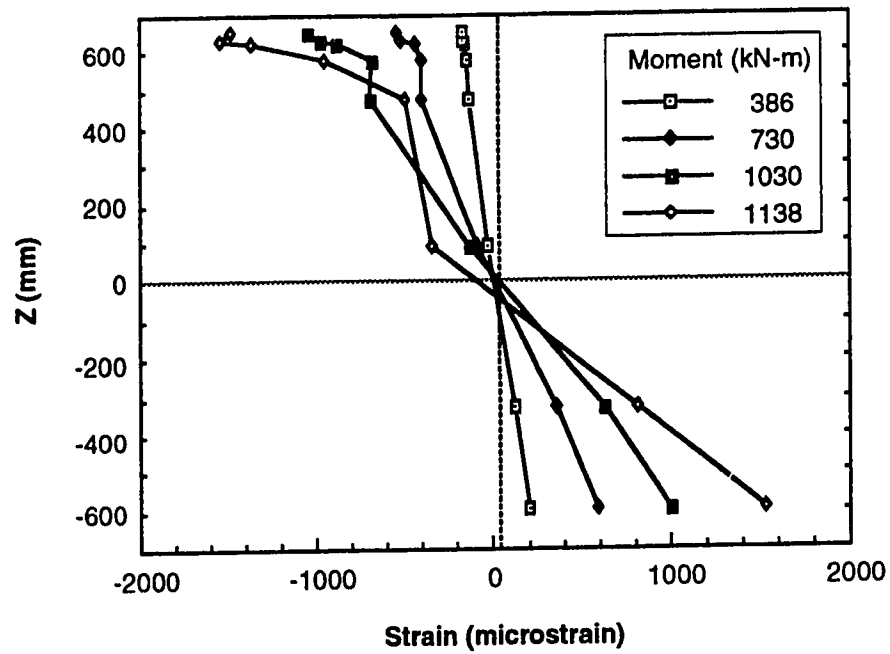


Figure 3.15 Specimen SB3a: strain distribution

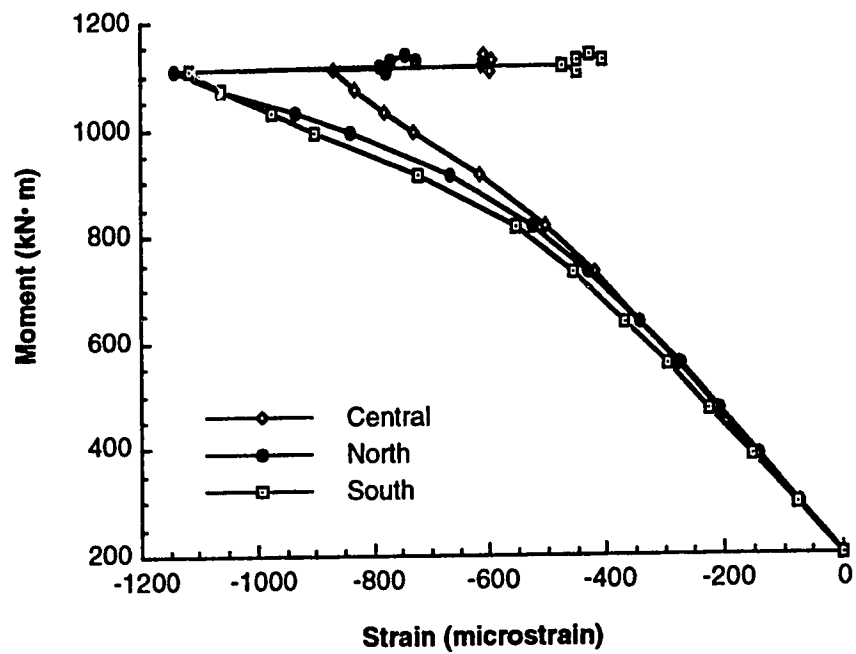


Figure 3.16 Specimen SB3a: moment versus compressive strain at different cross-sections

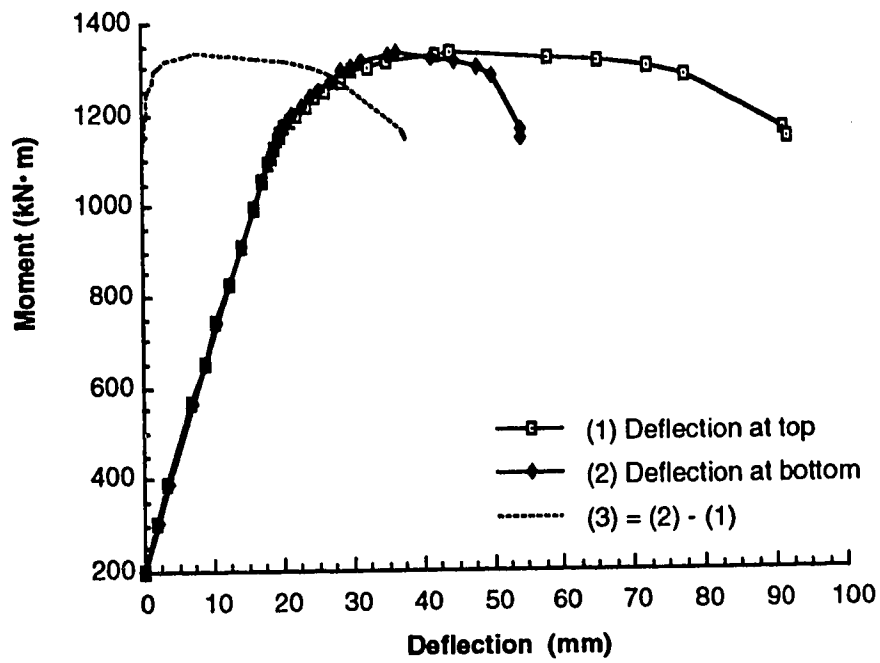


Figure 3.17 Specimen SB3b: moment versus deflection response

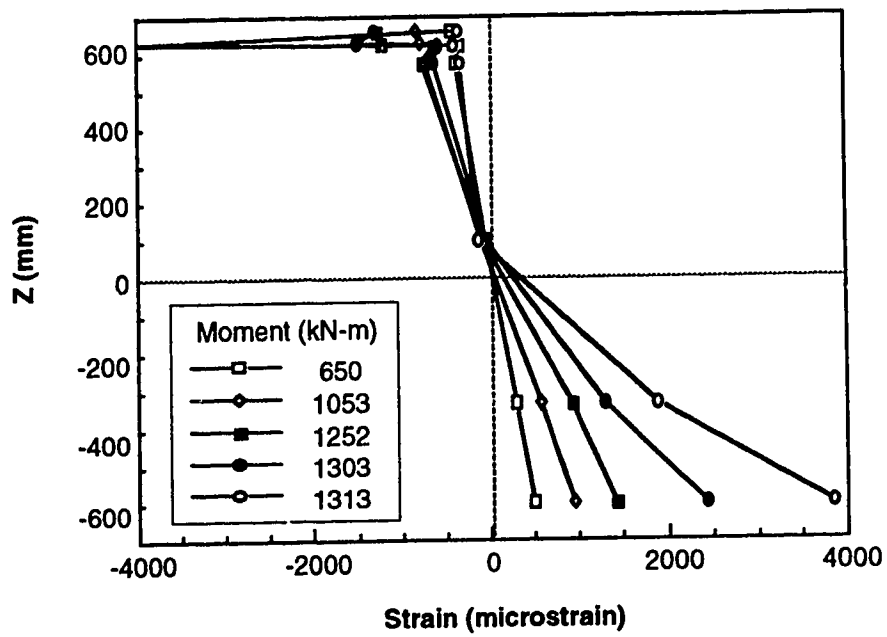


Figure 3.18 Specimen SB3b: strain distribution



Figure 3.19 Specimen SB3b: buckles in the stiffened area

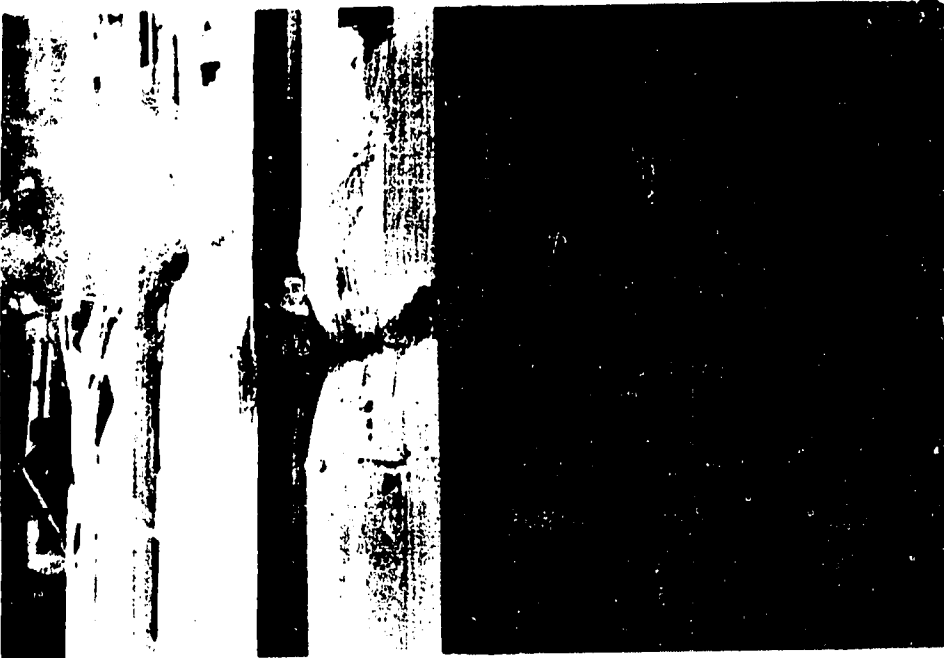


Figure 3.20 Specimen SB3b: deformed stiffeners and shells

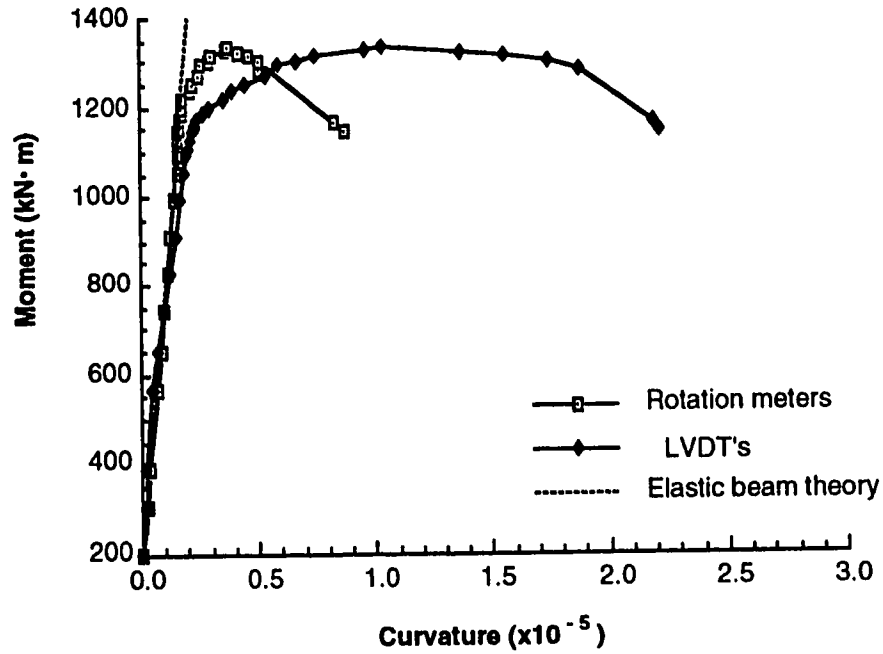


Figure 3.21 Specimen SB3b: moment versus curvature response

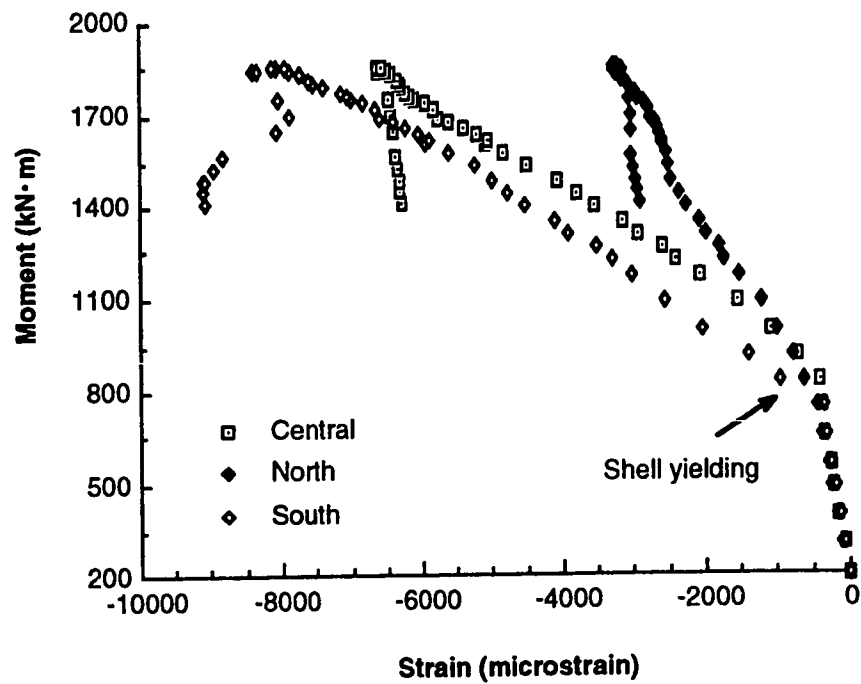


Figure 3.22 Specimen SB4: moment versus compressive strain
at different cross-sections

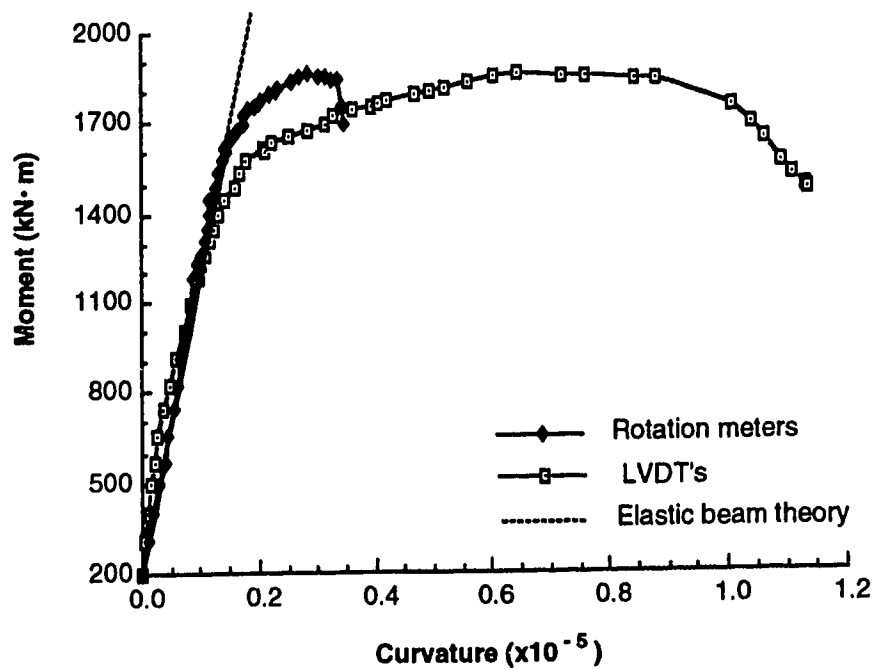


Figure 3.23 Specimen SB4: moment versus curvature response

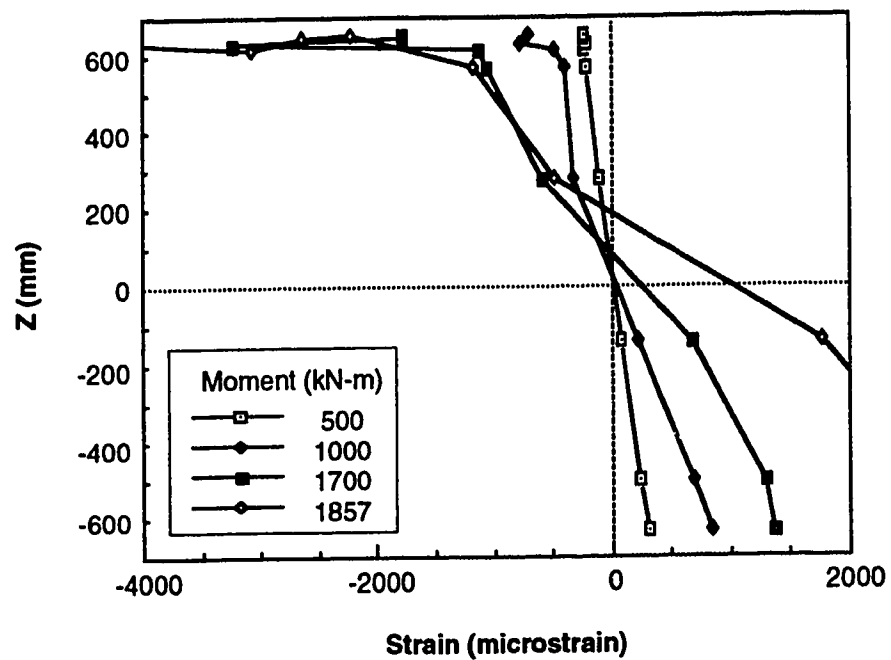


Figure 3.24 Specimen SB4: strain distribution

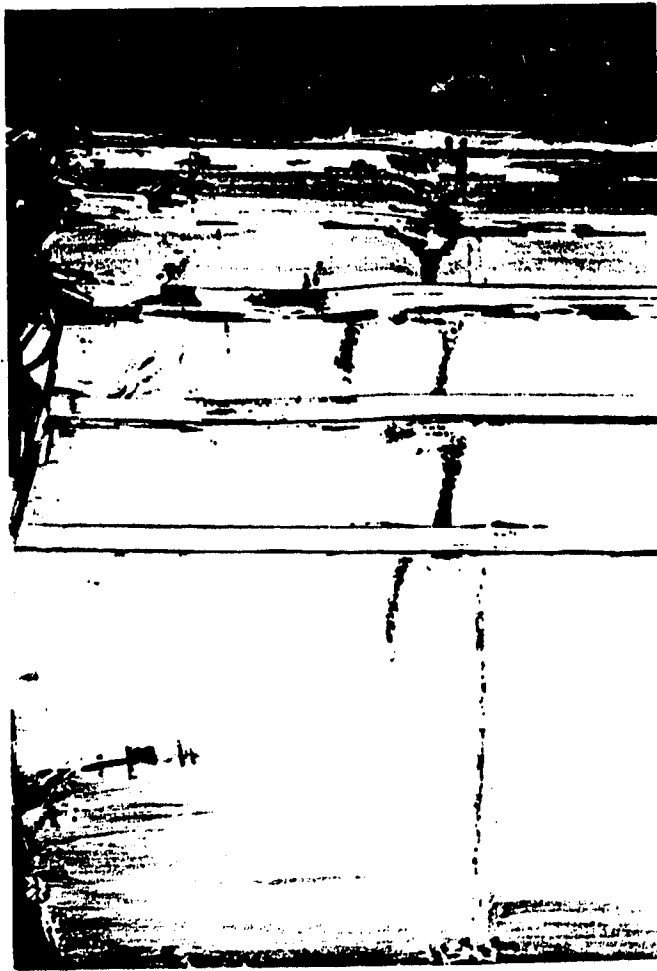


Figure 3.25 Specimen SP4: deformed shape

CHAPTER FOUR

NUMERICAL SIMULATION OF EXPERIMENTS

4.1 General

The numerical simulation of complicated structural behavior, such as the inelastic buckling of stiffened cylindrical shells, has been made possible by the most recent development of nonlinear finite element method. Widely available modern computers, such as workstations, greatly reduce the cost and time of computing. Since large-scale experiments of cylindrical shells are relatively expensive, finite element analysis provides an economic and efficient alternative. Additionally, finite element solutions give detailed description of the failure process. Good accuracy can be expected because not only are the geometrical and material nonlinearities included, but initial imperfections and residual stresses can also be incorporated. However, the validity of a sophisticated finite element model can only be established by comparison with the results of physical tests.

The finite element study presented here was developed in order to establish a finite element model that can predict experimental results. Subsequently, this model is applied to an extended numerical analysis (Chapter Five) so that a database suitable for a parametric study can be generated. As experimentation is a unique method to verify the analysis, the simulation of experiments is the first and crucial step in the numerical phase of this investigation. The four large-scale tests reported previously in Chapter Three and the one done by Bailey and Kulak (1984) were used for this purpose. All the computations involved were carried out on Sun SPARC and ELC workstations using the NISA program, which will be briefly reviewed in this chapter.

This chapter consists of two parts. In the first part, the geometry and the boundary conditions of the finite element model are described. The incorporation of initial imperfections and residual stresses is also discussed. The second part presents the simulation of the test specimens and their material. The results of the numerical analysis are compared with that from physical tests.

4.2 NISA Program

The NISA (Nonlinear Incremental Structural Analysis) program is a nonlinear finite element program coded in the FORTRAN 77 language (Häfner *et al.* 1981, Stegmüller 1984). It was originally written at the University of Stuttgart in Germany, and later modified at the University of Alberta. The program, which has simple and straightforward input and output format, is oriented for research and development purposes. The availability of its FORTRAN source code provided an opportunity for further modification. During this study, a series of changes have been made to meet the special needs of this project, including modification of the subroutines for material models and improvement of the computing efficiency on work stations. However, no major developmental work has been involved.

(There is another finite element program also named NISA, Numerically Integrated Elements for System Analysis. It is a commercial software distributed by the Engineering Mechanics Research Corp. in Michigan. Even though both are called NISA, these two software packages were independently developed, and their features and theoretical background are significantly different.)

The NISA program used at this University provides various types of elements. To model the cylinder and the stiffeners, three-dimensional degenerated plate-shell elements (Ramm 1980a, Ramm and Matzenmiller 1986) with four or sixteen nodes were employed. Each node has five degrees of freedom; three for translation and two for flexural rotation. Reduced numerical integration was used because it proved to be efficient and free of shear or membrane locking during the preliminary tests of these elements. A Simpson integration rule was applied through the shell thickness to account for nonlinear stress distributions. Three-dimensional beam elements have also been used to reproduce the boundary restraints of the experimental set-up.

The geometrical nonlinearity was handled using the total Lagrangian formulation provided in NISA. The inelasticity of structural steels was approximated with bi-linear (elastic-perfectly plastic or elastic-plastic hardening) or tri-linear (different hardening moduli in two inelastic stages) curves. During this study, the von Mises yield criteria and associated flow rule were adopted for metal plasticity. The hardening behavior was described using an isotropic strain-hardening model. Such a model gives satisfactory

results for metal structures unless a large portion of material is subjected to reversal loading. In the latter case, a kinematic hardening model would be more appropriate.

NISA offers different choices for the solution strategy (Ramm 1980b). In this analysis, the displacement control approach, along with the standard Newton–Raphson iteration method, was chosen for its robustness and the efficiency exhibited during computation. The degree of freedom to be controlled was the rotation of the cross-section at the end of a cylinder, namely the ϕ_y rotation of the beam nodes. The convergence was controlled by the displacement criteria

$$\|dU\|_2 < \varepsilon_1 \|\Delta U\|_2 \quad (4.1)$$

in which dU is the change of displacement increment during iterations and ΔU is the total displacement increment in the current load step. The notation $\|\cdot\|_2$ represents the Euclidian norm of the vector included in the notation. The tolerance, ε_1 , was set to be 1%.

4.3 Finite Element Model

4.3.1 The Cylinder

The displacement field for a cylindrical shell was discretized using sixteen node bi-cubic shell elements. A three-by-three Gaussian integration rule was used over the surface and a five-point Simpson integration was carried through the thickness. There are five displacements at each node (Figure 4.1): U_x , U_y , and U_z are translations along axes x , y and z , ϕ_x is the rotation of the normal (\underline{n}) about the x axis, and ϕ_θ is the rotation of \underline{n} about the tangent to the circumference (\underline{t}), which is in the y - z plane.

It was learned through preliminary examination that the fineness of the mesh is critical for an accurate solution. Models with a coarse mesh tended to be very stiff, and could fail at unrealistically high load levels. Therefore, the size of elements has to be limited in the area where buckling may develop. For instance, the experimental results from the 5 mm thick cylinder (specimen SB2) indicated an average half-wave length of about 73 mm along the longitudinal axis, while its width along the circumference was usually dominated by the spacing between stiffeners. Thus, it was necessary that the element size be less than 220 mm in the longitudinal direction in order that buckling waves could be closely approximated by the cubic displacement field.

In order to reduce the storage size in computation, only one quarter (half of the length and half of the cross-section) of the cylinder was modeled (Figure 4.2). Symmetrical boundary conditions were assumed along the cut off edges. For example, the following degrees of freedom were restrained at the longitudinal edges (where $y = 0$):

- (1) the translation perpendicular to the longitudinal plane of symmetry (x - z plane), i.e. the y -displacement;
- (2) the rotation of the normal about the longitudinal axis (x -axis), i.e. the ϕ_x rotation.

Similarly, the x -displacement and the ϕ_θ rotation were restrained at the midspan cross-section, where the y - z plane was assumed to be a plane of symmetry. Other displacements at the edges remained free. These conditions are summarized in Table 4.1, and are also illustrated graphically on Figure 4.3.

The symmetric restraints described above imply that the cut off edges are the peaks or valleys of shell buckling waves. Even though a perfect cylinder under pure bending would demonstrate such symmetries, it will not necessarily be the case for a fabricated imperfect cylinder. However, since the size of the buckling waves are relatively small compared with the dimensions of the large diameter cylinder, a small discrepancy in locating the buckling waves will not significantly change the buckling behavior. Consequently, the overall results should not be substantially different because of the assumption of symmetry.

In order to exclude rigid body movement in the z direction, a support was placed near the neutral axis at the cross-section of the rigid end (Figure 4.3). It should be noted that all the above boundary restraints allow full freedom to the deformation modes of the cross-section (ovalization, local buckling, etc.) everywhere except at the built-in rigid end.

4.3.2 The Stiffeners

Four node shell-plate elements were used to discretize the walls of the HSS stiffeners. To avoid membrane and shear locking, one point reduced integration was employed except at the very end, where the elements were fully integrated at two-by-two

points to exclude zero energy modes. Similar to the sixteen node element, five points through the thickness were used for Simpson integration.

Among the various types of shell elements available, some have six degrees of freedom at each node and three of the six are rotations. This makes it easy when two surfaces meet at an angle. However, the four node and sixteen node shell elements in NISA have only five degrees of freedom at each node: two rotations and three translations. Among the two rotations, ϕ_θ is defined in the local coordinate system of the element to which the node is bound. At the corner of stiffeners, where two wall elements meet at a right angle, the ϕ_θ rotations of the two elements do not represent the same rotation—their directions are 90° apart (Figure 4.4).

To resolve the inconsistency of ϕ_θ at the corners, a dual node model was proposed. As shown in Figure 4.4, there are two overlapped nodes, for example nodes 1 and 2, at each corner. To ensure a continuous displacement field, the U_x , U_y , and U_z translations of the dual nodes were coupled, as were the ϕ_x rotations. This implied that the included right angle at the corner would remain so during deformation. The ϕ_θ rotations of the two nodes were left uncoupled, since they were physically independent of each other. Where the bottom side of the stiffener meets the shell surface, the U_x , U_y and U_z of the shell node (node c in Figure 4.4) are also coupled with those of stiffener nodes (nodes a and b), while ϕ_x and ϕ_θ of the shell node remained independent of those of the stiffener nodes.

In order to test the validity of the dual node model, it was used to analyze the bending and torsion of thin-walled members. The predictions were in accurate agreement with the theoretical results of thin-walled beams. Meanwhile, another model with a single node at the corner failed to produce consistent results. This is because the combination of the ϕ_θ rotations in the two elements meeting at a right angle forced the stiffness coefficients of unrelated degrees of freedom to be wrongly associated together. Consequently, the stiffness matrix was miscalculated and the resistance of the structure was overestimated.

4.3.3 The Rigid End

In the test set-up described in Chapter Three, the end of the cylinder was welded to a thick steel plate that was heavily stiffened. During deformation, such an arrangement maintained the circular shape of the cylinder and also helped to keep the end cross-section planar. In order to duplicate such a rigid end in the finite element model, a network of

rigidly connected three-dimensional beam elements was placed at the end cross-section (Figure 4.2). Some of these beams ran radially from the center to the shell edge, while others joined the neighboring nodes circumferentially. Large stiffness was assigned to these beams so they would provide high rigidity relative to the shell.

Every beam node has six degrees of freedom: three translations (U_x , U_y and U_z) and three rotations (ϕ_x , ϕ_y and ϕ_z), all defined in the global coordinate system. It is apparent that U_x , U_y , U_z and ϕ_x match those of the shell elements. However, ϕ_y and ϕ_z do not exist in the shell elements. This causes problems when a beam element joins a shell element at a single node. The stiffness for different degrees of freedom, such as ϕ_y of the beam element and ϕ_θ of the shell element, will be mistakenly combined together when assembling the stiffness matrix. In a way similar to that used for the dual node model for the stiffeners, the problem was solved by using two overlapped separate nodes, one for the beam element and one for the shell element, wherever two such elements interface. The U_x , U_z and ϕ_x of both nodes were coupled, which meant that the corresponding displacements, say U_x , from the two nodes were set to be equal. Because no lateral translation was allowed at the end cross-section, U_y was restrained. The ϕ_y rotations of all beam nodes were coupled: thus the whole cross-section could have a unique rotation and still remain in a plane. The remainder of the degrees of freedom were set to be free. The results of these end restraints were satisfactory. In most cases, the deviation from the best-fit plane was less than 1% of the total displacement U_x throughout the loading history.

4.3.4 Loading

In the numerical model, loading of the specimen proceeded by application of a bending moment to the cross-section at the rigid end. The moment was represented by a set of work-equivalent nodal forces. The nodal forces required to produce a unit bending moment were predetermined. During the numerical analysis, the moment was applied by increasing the nodal forces proportionally.

The work-equivalent forces (\mathbf{P}) were calculated as

$$\mathbf{P} = \int_A \sigma_x \mathbf{N}_x dA \quad (4.2)$$

which was derived from the work-equivalent relation

$$\delta U_x^T \mathbf{P} = \int_A \sigma_x \delta U_x dA \quad (4.3)$$

This sets the virtual work of the load \mathbf{P} equal to that of an equivalent stress distribution σ_x acting on the cross-section. In Equations 4.2 and 4.3, the integration domain A is the cross-sectional area and N_x is the shape function of the displacement field, U_x . The distributed stress σ_x was formulated according to the classic beam theory using

$$\sigma_x = \frac{M}{I_y} (z - z_0) \quad (4.4)$$

in which M is the bending moment, I_y is the moment of inertia about the y axis, and z_0 refers to the z -coordinate of the neutral axis.

By using the work-equivalent forces, the local effect that may result from a large single concentrated load can be avoided. In the analysis, it was found that the application of work-equivalent forces helped the end cross-section to maintain a plane.

The direction of these nodal forces was kept constant along the x axis. Because of the rotation of the end cross-section, the moment arms of these forces, i.e., the vertical distance between the forces, shortened slightly as load was applied. However, the effect on the bending moment was found to be negligible. Since the end rotation of short cylinders was relatively small, the change of the moment arms resulted in less than 0.1% difference in the bending moment.

4.4 Initial Imperfections

In finite element analysis, the geometrical imperfections are usually incorporated by locating the nodes along the imperfect profile of the structure. Nevertheless, there are several alternative ways of using the imperfection data. Premier buckling modes (Pinkney *et al.* 1983, Petrick 1985, and Mok and Elwi 1986) and trigonometric functions (Chryssanthopoulos *et al.* 1991a and 1991b) have been used to extract imperfections from measured data. However, the procedure employed here uses the imperfections actually measured from specimens fabricated in accordance with standard industrial practice. The errors contained in the raw data were eliminated through a process developed for imperfection data analysis (Section 3.2.3).

During this investigation, a FORTRAN program named IGI (Implementation of Geometric Imperfections) was developed and used to prepare the input of imperfections. It first interpolates the measured or assumed initial imperfections at the nodal positions of the finite element mesh, then adds these imperfections to the perfect profile to produce an imperfect cylinder. Since the imperfections of stiffeners are less crucial than shell imperfections and they are difficult to measure, no measurements or assumptions have been made for the imperfections of stiffeners. In this model, the stiffeners were simply attached to the imperfect shell surface.

Since only one-quarter of the cylinder was modeled, it was decided that the imperfections of the part with the largest out-of-roundness values (Type (c) imperfections, as cataloged in Chapter Three) should be used. Averaging the imperfections of four quarters does not seem rational because it may smear randomly distributed imperfections. Nevertheless, numerical results using imperfections from different parts of the cylinder gave the same results, both for the buckling mode and for the failure load.

4.5 Residual Stresses

As examined in Chapter Three, the residual stresses resulting from the welding of stiffeners to the shells were of significance. They were, therefore, incorporated into the finite element model. Since the test measurements only gave the residual stresses at selected points in the most critical area, the following assumptions were made to describe the overall distribution in the compression zone.

- (1) The compressive and tensile residual stresses in the shell between the stiffeners were uniformly distributed;
- (2) The residual stresses in the stiffener, caused by welding of the stiffener to the shell, were similar to those in the shell, but with compression at the top and tension at the bottom. The side walls of the stiffeners were assumed to be free of residual stresses.

These assumptions are shown in Figure 4.5, where σ_{rt} is the tensile residual stress, σ_{rc1} is the compressive residual stress in the stiffened shells, and σ_{rc2} is the compressive residual stress outside the stiffened area.

A distributed fictitious temperature loading was used to produce the initial strains necessary to set up the required residual stresses in the shell and stiffeners. Orthotropic expansion coefficients were assigned to the material so that residual stresses were generated in the designated direction. This method has been described in principle by Roman and Elwi (1990) and by Obaia *et al.* (1991). The temperature distribution must be chosen such that the corresponding stresses are self-equilibrating. In this manner, temperature changes will not result in a redistribution of stresses.

However, such a process introduced additional initial deformations. As acknowledged by other investigators (Hu 1991), these deformations should be eliminated for the following reasons. First, deformations under the fictitious temperature loading are apparently different from the residual deformations due to the welding process. This is because the constitutive model used was the same as that outlined in Section 4.2. Neither the phase change during welding nor the thermal elastic-plastic behavior of steels were included in the analysis. Secondly, the measured or assumed initial imperfections generally already include the residual deformations introduced simultaneously with the residual stresses.

During the experimental phase of this investigation, the measurement of initial imperfections was performed after the welding of stiffeners. Thus, the measured cylinder was the one with residual stresses and corresponding deformations. To reproduce such a process, the finite element model prior to loading should be built with residual stresses and measured imperfections, which should include the deformations due to the welding process. Using this idea, the deformations due to the simulation of residual stresses were computed from a trial run. This pattern was then subtracted from the assumed imperfect profile so that it could offset the corresponding deformations when the artificial temperature field was imposed, and, thus, yield a profile which matched the measured imperfections.

The procedure used here, which is somewhat more complicated than that used by Roman and Elwi (1990), can be described as follows:

- (1) Calculate the fictitious temperature distribution (T) at the stiffened area from the residual stresses distribution as

$$T = - \frac{\sigma_r}{\alpha_T E} \quad (4.5)$$

where σ_r is the measured or assumed residual stress, E is Young's modulus, and α_T is the coefficient of thermal expansion for structural steel ($\alpha_T = 1.17 \times 10^{-5} / ^\circ\text{C}$).

- (2) Work out the overall distribution of the temperature so that the self-equilibrating conditions

$$\int_A T \, dA = 0 \quad (4.6)$$

and

$$\int_A T \, z \, dA = 0 \quad (4.7)$$

can be satisfied. Here, A is the cross-sectional area, and the z -coordinate is the distance of an element dA to the y axis. Equations 4.6 and 4.7 indicate that the resultant forces, the axial force and the moment, must be zero for every cross-section.

- (3) Apply the temperature loading and perform the trial run using NISA. The temperature will produce stresses σ_T and displacement U_T . If the agreement between σ_T and the designed distribution is not satisfactory, modify T and redo steps (1) to (3).
- (4) Subtract U_T from the imperfect profile. Then reapply the temperature distribution to the new geometry and carry on the analysis.

The procedure described above produces a finite element model which has a specified residual stress distribution and initial imperfections matching the measured profile. As an example, in Figures 4.6 and 4.7 the simulated residual stresses for the model of specimen SB2 are compared with the measurements taken in the laboratory. The measured tensile residual stress ($0.6\sigma_y$) is taken as the average level underneath stiffeners, even though a localized tensile yield may exist near the weld.

4.6 Numerical Results

In order to examine the validity of the proposed finite element model, it was used to predict the results of large-scale physical experiments. Results of five tests were involved in this study: four from the experiments of the current investigation, SB2, SB3a, SB3b and SB4, and one, SB1, from a test reported earlier by Bailey and Kulak (1984). The initial imperfections and welding residual stresses measured from the test specimens were incorporated into the simulation. Dimensions of the models were the same as the average values recorded in the test specimens (Tables 2.1 and 3.1).

4.6.1 Test SB2

The shell material of specimen SB2 was taken as elastic-perfectly plastic in the range below the maximum strains recorded in the analysis. The coupon test shown in Figure 3.2 demonstrated a long yield plateau before hardening ($\epsilon > 2\%$), which could hardly be reached at the time of failure. The output of finite element results showed that the highest strain level at maximum moment was 1.8% and it occurred only at localized areas such as the tops of buckling waves.

The small size HSS stiffeners used in the test exhibited a strain-hardening behavior in stub column coupon tests. This was believed to be a result of the residual stresses and nonuniform material properties induced by the manufacturing process. As shown in Figure 4.8, such a material behavior can be easily approximated by a tri-linear stress versus strain curve. Since in the numerical model the stiffeners were assumed to be of homogeneous material, the tri-linear curve represented its average stress versus strain relationship. In Figure 4.8, E refers to the elastic modulus, σ_{y1} to the initial yield stress and σ_{y2} locates the stress point between two different inelastic stages. The hardening moduli for these stages are represented by E_{h1} and E_{h2} . Table 4.2 lists the values of these parameters.

The moment versus curvature response from both the physical test and the numerical analysis is shown in Figure 4.9. All of the curvatures were measured at the same cross-section, where the test and thick end segments joined, but their definitions were somewhat different. The rotation meters were mounted at the mid-depth of the cross-section and the change of rotation angles were used to calculate the curvature. The

numerical and the LVDT curves were calculated from the top and bottom displacements. However, the LVDT at the top of the specimen was damaged at an early stage of this test. Even so, the curves from the test and numerical analysis show the same pattern of behavior: a linear portion through the initial loading history is followed by a small onset of nonlinear part, then a sharp peak corresponding to the shell buckling, and finally a mild descending portion after the ultimate point. The ultimate moment from the finite element analysis is 2007 kN·m. This is only 3% higher than the test result (1947 kN·m).

The similarity between the finite element solution and the test result can also be observed from the buckling mode of SB2. Figure 4.10 is a plot of the deformed model at the ultimate moment. Parameter a is the scale factor of displacements. The largest shell buckles can be seen outside the stiffened area, near the girth weld joining the thick end segment to the test segment. Both the location and shape of buckles agree with those observed in the physical test (Figure 3.12).

4.6.2 Test SB3a

The 3 mm thick plate used for specimen SB3a did not show a yield plateau in the stress versus strain curve of the coupon test (Figure 3.2). Instead, the curve climbs up immediately after the yield point as hardening develops. In the range of $\epsilon < 3\%$, these characteristics were expressed by a bi-linear elastic-plastic hardening curve, as shown in Figure 4.11. The mean value of the hardening modulus was 2370 MPa according to the coupon tests. For the HSS stiffeners, the average stress versus strain behavior was described by a tri-linear relation, like that of specimen SB2. Values of the parameters defining the curve are included in Table 4.2.

The finite element model of specimen SB3a incorporated the initial imperfections and welding residual stresses taken from the laboratory measurements. Both indicate that the 3 mm thick shell had more severe imperfections and higher welding residual stresses than did the 5 mm thick specimen (SB2).

In a fashion similar to that observed in SB2, specimen SB3a also failed at the onset of compression buckling of the shell in the shell outside the stiffened area. Figure 4.12 shows the comparison between the moment versus curvature behavior obtained from the test and the numerical analysis. As mentioned in the previous section, the numerical curve should correspond to the test curve calculated from the LVDT readings. However, the

finite element model appears to be stiffer than the tested cylinder in the inelastic range. The model reached an ultimate moment of 1233 kN·m, which is 8.3% higher than that achieved during the test (1138 kN·m). The numerical results show a long plateau near the ultimate point. For the test curve, however, the post-peak portion is not available since the testing was terminated as soon as the load started to drop.

The failure mode of the numerical model was consistent with the test observation. Large shell buckles in the shell outside the stiffened area of the shell can be seen in Figure 4.13. Moreover, there are also several shell buckles between stiffeners, which were also observed in the test, indicating that the buckling load of the stiffened area was not far away from the shell buckling load outside the stiffened area. The most significant waves were in the vicinity of the girth weld between the thin shell and the thick segment.

4.6.3 Test SB3b

After testing SB3a, this cylinder was repaired and two additional stiffeners were added. This modified specimen was then tested as SB3b. In the numerical study, however, the model of SB3b was prepared as a virgin specimen. The geometry, material properties, geometric imperfections and residual stresses measured from SB3a were used in building the model of specimen SB3b. The finite element analysis was not able to include the complicated strain history from SB3a to SB3b.

The moment versus curvature response of SB3b is presented in Figure 4.14. It can be seen that the finite element curve traced the experimental behavior closely. The ultimate moment obtained in the numerical analysis was 1353 kN·m, which is 1.5% higher than the test result of 1333 kN·m. The buckled model shown in Figure 4.15 is very similar to that observed in the test specimen: buckling waves occurred across the stiffened area and the buckles with the largest amplification took place near the girth weld between the test and end segments. The numerical analysis duplicated the general buckling mode identified in the experiment.

4.6.4 Test SB4

The test segment of specimen SB4 was built from a 3 mm thick cylinder. Since the fabrication process of the tube was identical to that of SB3a, it was assumed that the initial imperfections and residual stresses were the same as those measured for specimen SB3a.

The material properties of the 3 mm thick steel plate were different from those of SB3a, however, since it was supplied from different stock. A typical elastic-plastic stress versus strain curve of hot-rolled steel was obtained from the tension coupon test (Figure 3.2), and it was approximated by a bi-linear elastic-perfectly plastic material model in the analysis since most part of the material would not reach the hardening stage before the ultimate point.

Figure 4.16 shows the numerical and experimental moment versus curvature behavior. The finite element model predicted a capacity of 1802 kN·m after plasticity and buckling were well developed. Compared with the failure load of 1857 kN·m, the finite element solution was 3% lower. The failure predicted by the numerical analysis is plotted in Figure 4.17, in which the buckles of the shell and stiffeners are primarily in the stiffened area, indicating failure in general buckling. This failure mode was the same as observed in the test specimen.

4.6.5 Test SB1

This test, which had been conducted in another test program at the University of Alberta (Bailey and Kulak 1984), was reviewed in detail in Chapter Two. The measured imperfections of the specimen were analyzed using the program IGI and included in the model. The welding residual stresses were assumed to be the same as SB2 because of the similarity between the shell thickness of SB1 and SB2. Stub column test curves of the HSS stiffeners were not available: only the yield strength was reported by the investigators. However, all the stiffeners in SB1 and SB2 were made from CSA G40.21 350W steel, and the dimensions and the yield strength of those in SB1 were close to what was measured in SB2. Therefore, the material properties of the HSS stiffeners in SB1 were assumed to be the same as those in SB2, and the tri-linear stress versus strain curve used in modeling SB2 was applied to SB1. The shell material was taken to be elastic-perfectly plastic as the coupon tests indicated.

The ultimate moment of the finite element model was 3130 kN·m, which was 2% higher than that achieved during the test. The moment versus curvature results are plotted in Figure 4.18. A substantial increase of load can be observed after yielding and buckling. The buckling shape in Figure 4.19 duplicated the experimental behavior of specimen SB1: the stiffeners and shells deformed simultaneously in a general instability failure.

4.7 Summary

A finite element model of a longitudinally stiffened cylinder subjected to bending was built up using a nonlinear incremental large deformation program, NISA. Three dimensional degenerated plate-shell elements were used for both shells and stiffeners. A dual node model was proposed in order to avoid the improper assembly of the stiffness matrix at the locations where plate-shell elements joined at right angles. This occurred at locations such as the corners of stiffeners or where different types elements were joined together, such as the beam and shell elements at the rigid end. The geometry and material aspects have been discussed in detail. The model incorporated both initial imperfections and residual stresses.

The numerical model was applied to five large-scale fabricated steel cylinders and the results were compared with those obtained in the physical tests. The geometry, imperfections, residual stresses, and the anticipated failure mode varied from one specimen to the other. Despite these differences, numerical analysis identified the same buckling modes as were observed in the tests. The load versus displacement behavior of the numerical models was in good agreement with those obtained from the test results. The discrepancy between the predicted ultimate moments and the test results varied from -3% to 8%, as shown in Table 4.3.

Table 4.1 Symmetric Boundary Conditions

Edge	Restrained DOF	Free DOF
$x = 0$ (midspan cross-section)	U_x, ϕ_θ	U_y, U_z, ϕ_x
$y = 0$ (longitudinal plane of symmetry)	U_y, ϕ_x	U_x, U_z, ϕ_θ

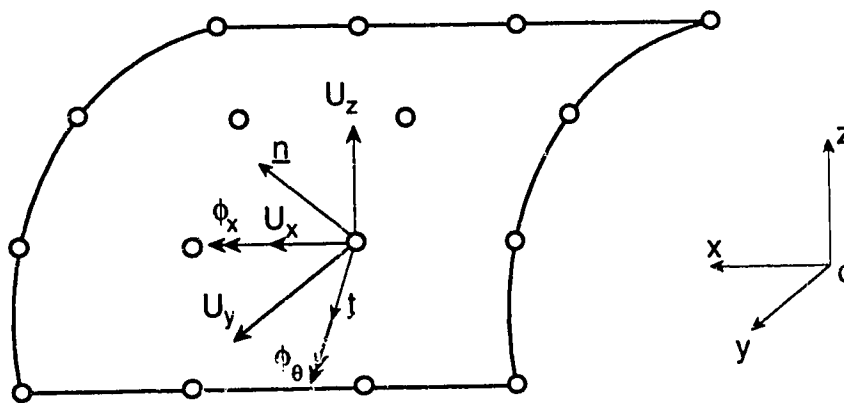
Table 4.2 Parameters for the Material Model of HSS Stiffeners

Test	σ_{y1} (MPa)	σ_{y2} (MPa)	E (MPa)	E_{h1} (MPa)	E_{h2} (MPa)
SB2	328	483	209×10^3	267×10^3	2920
SB3a; SB3b	420	520	214×10^3	8990	914
SB4	397	500	193×10^3	149×10^2	1090

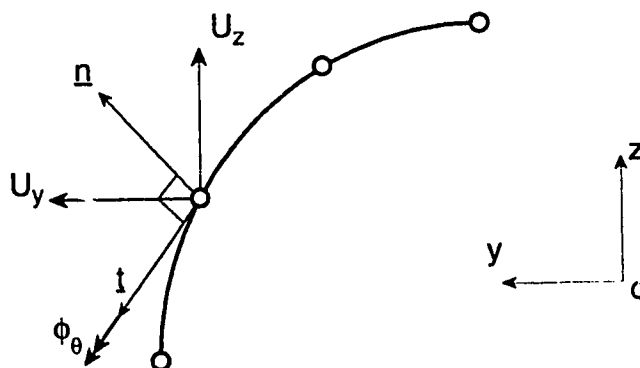
Table 4.3 Comparison of Numerical Analysis and Physical Tests

Test	Ultimate moment (kN·m)		
	(1) Finite element	(2) Experimental	(3) = (1) / (2)
SB2	2007	1947	1.031
SB3a	1233	1138	1.083
SB3b	1353	1333	1.015
SB4	1802	1857	0.970
SB1	3133	3068 ^a	1.020

^a adapted from Bailey and Kulak (1984)



(a) Displacement components at each node



(b) Cross-sectional view

Figure 4.1 Degrees of freedom of the plate-shell element

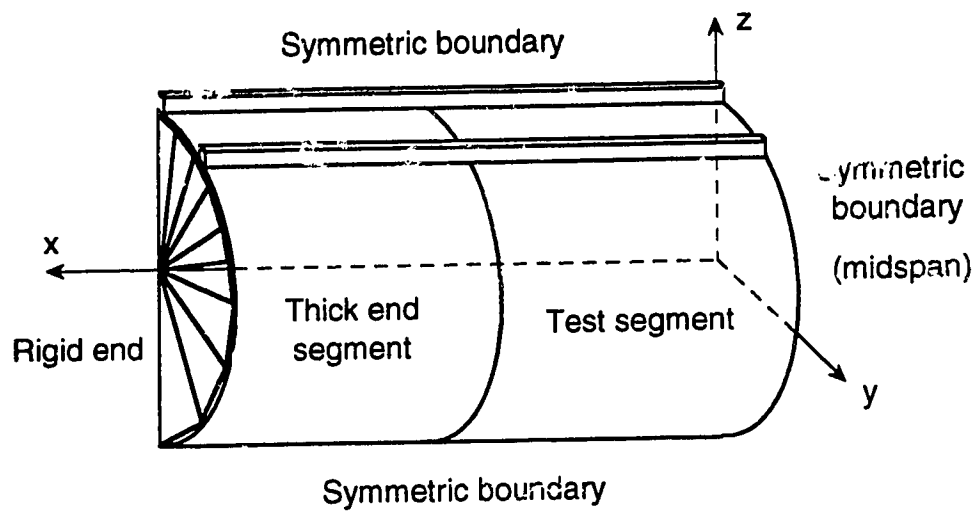
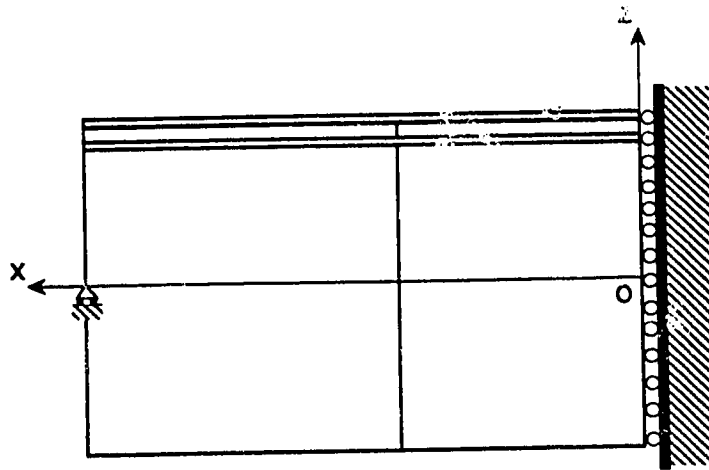
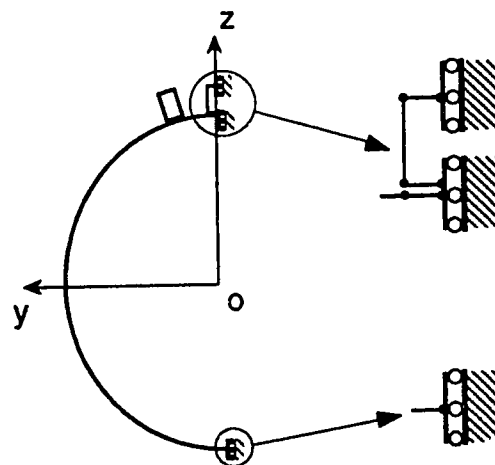


Figure 4.2 Schematic of the finite element model



(a) Side View



(b) Cross-sectional view

Figure 4.3 Boundary conditions for the finite element model

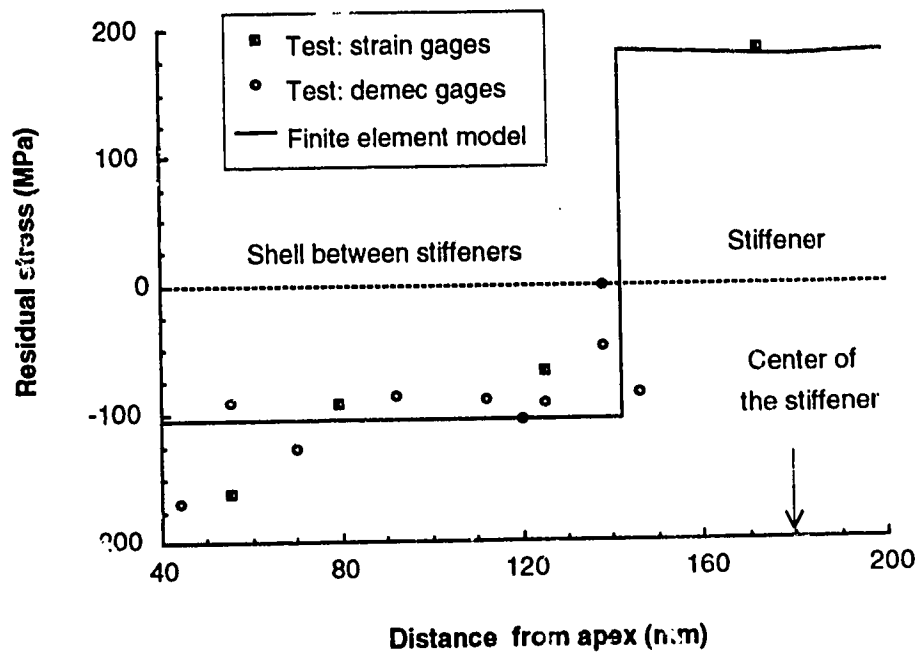


Figure 4.6 Comparison of residual stress distribution for SB2: shell between stiffeners

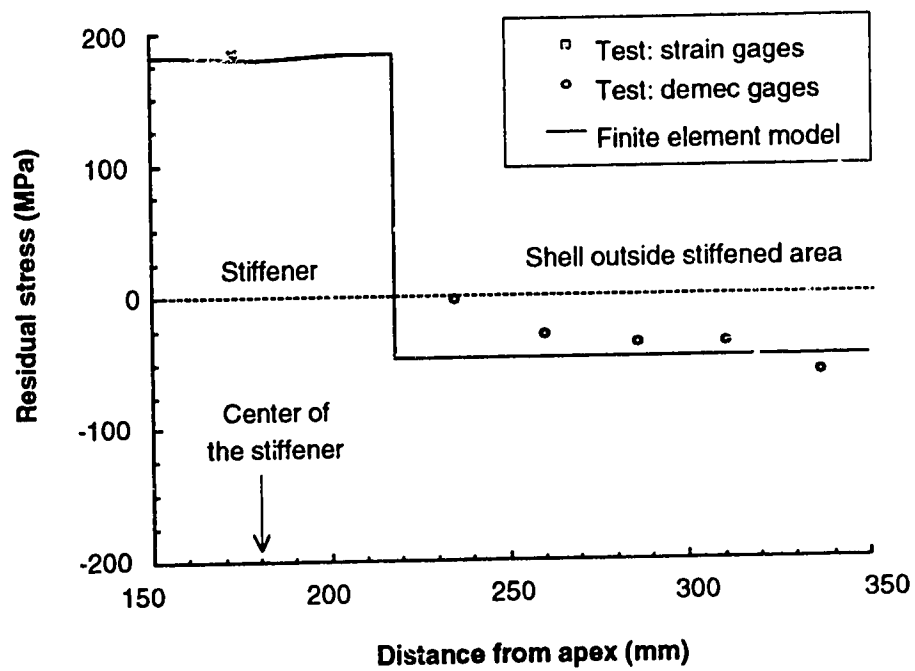


Figure 4.7 Comparison of residual stress distribution for SB2: shell outside the stiffened area

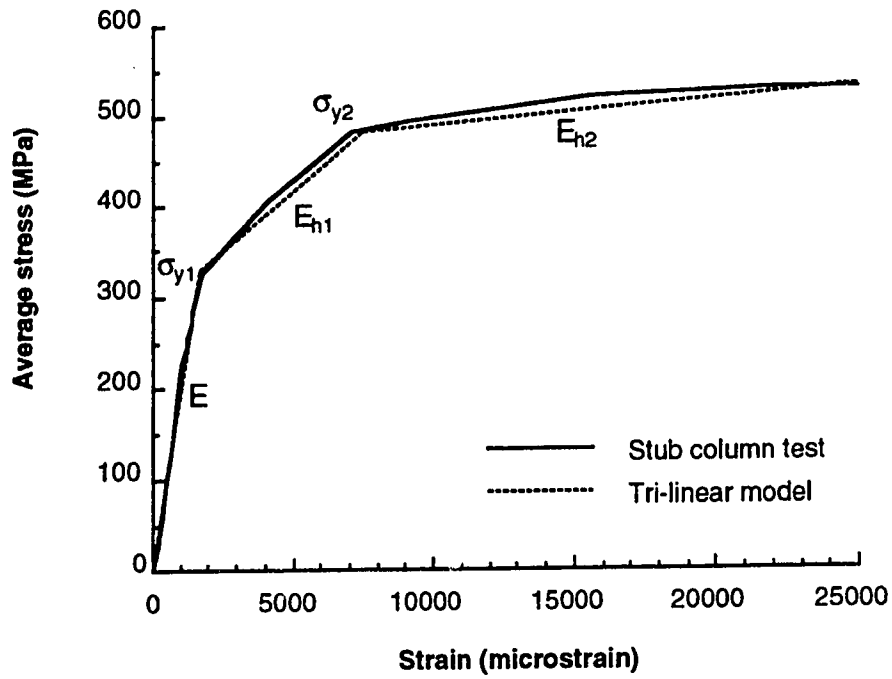


Figure 4.8 Material model for HSS stiffeners of SB2

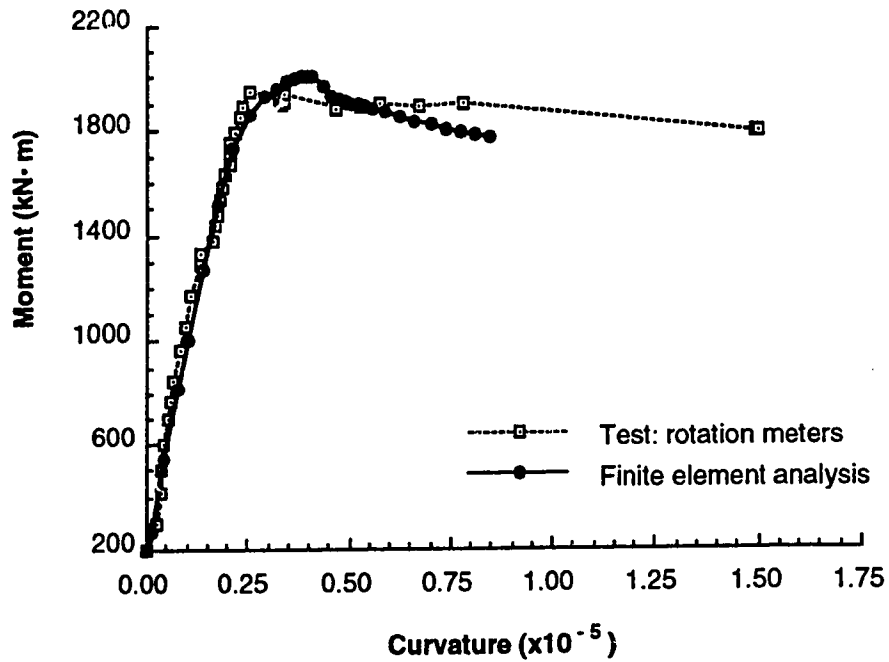


Figure 4.9 Moment versus curvature response of test SB2

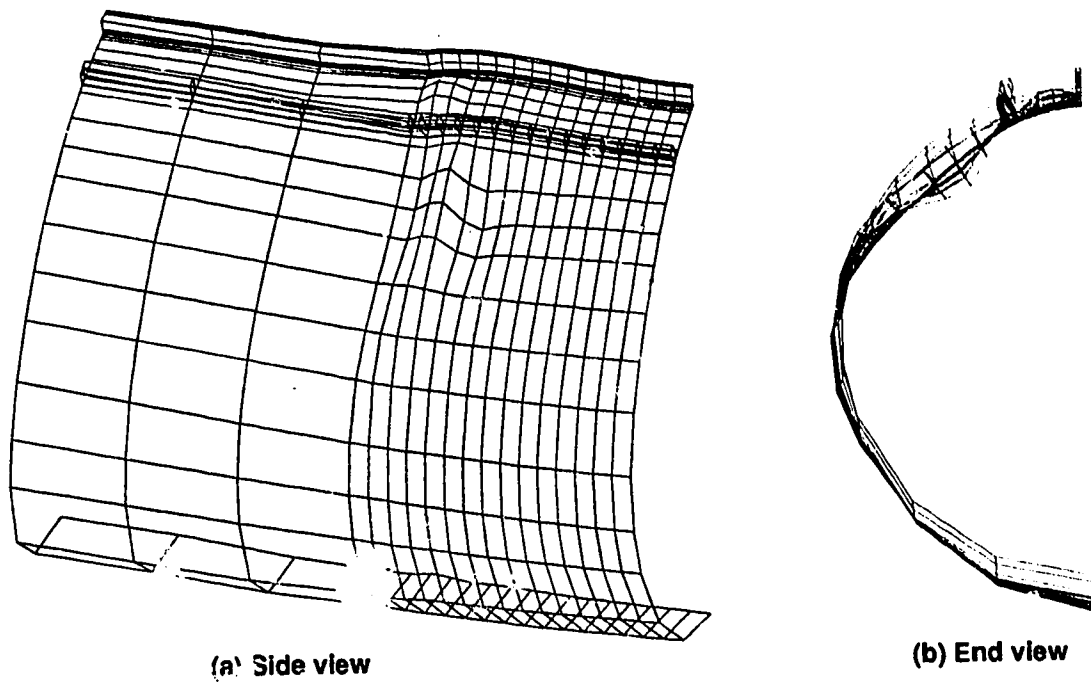


Figure 4.10 Deformed shape of SB2 ($M=M_u$, $a = 30$)

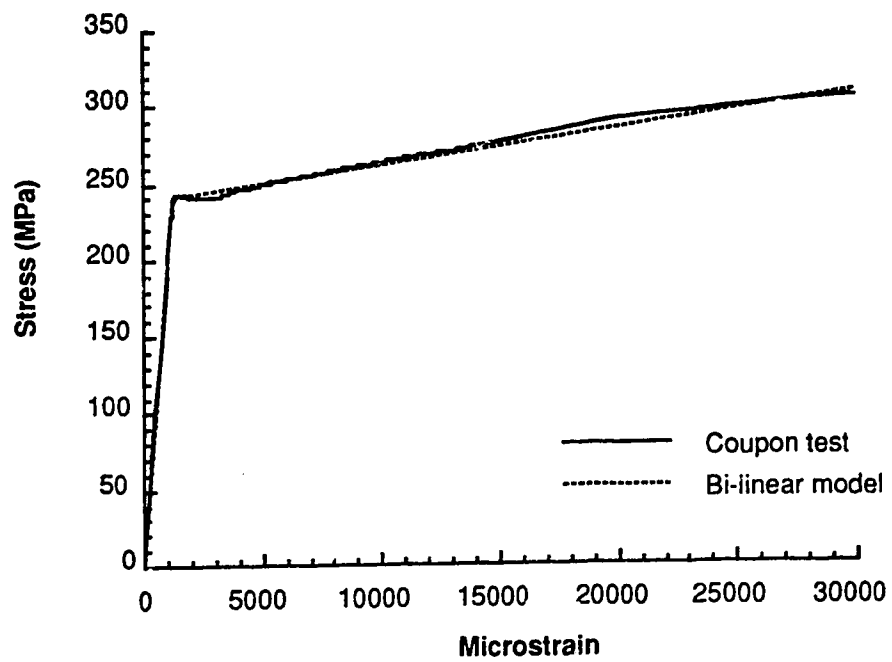


Figure 4.11 Material model for shell of SB3a and SB3b

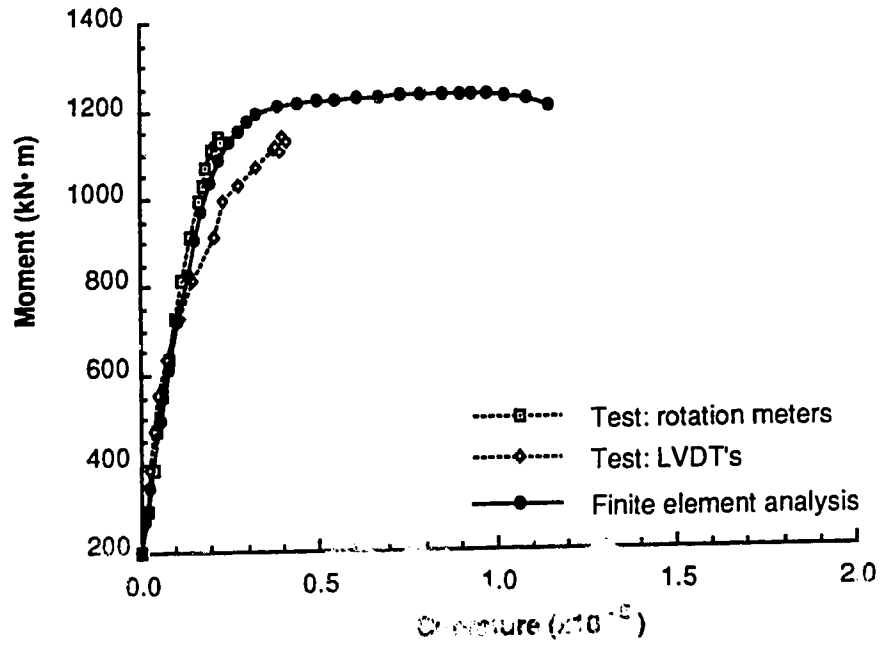


Figure 4.12 Moment versus curvature response of test SB3a

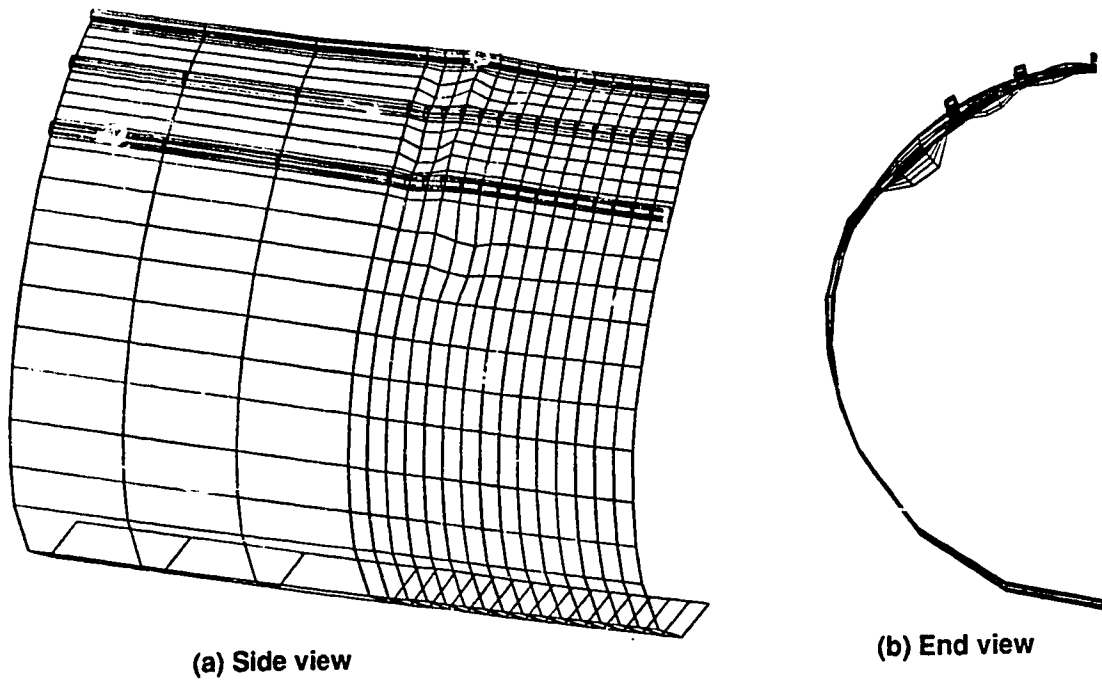


Figure 4.13 Deformed shape of SB3a ($M = M_u$, $a = 10$)

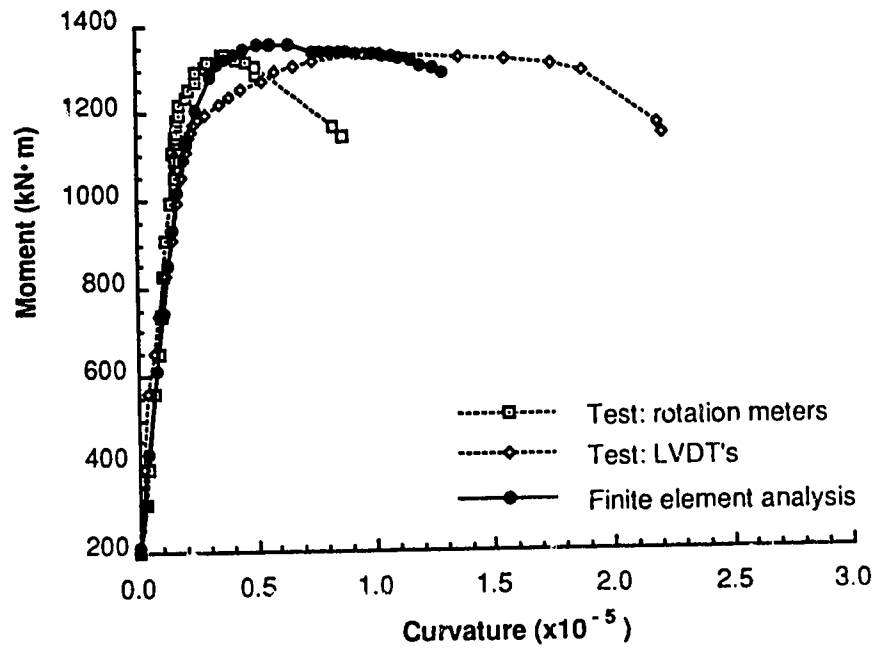


Figure 4.14 Moment versus curvature response of test SB3b

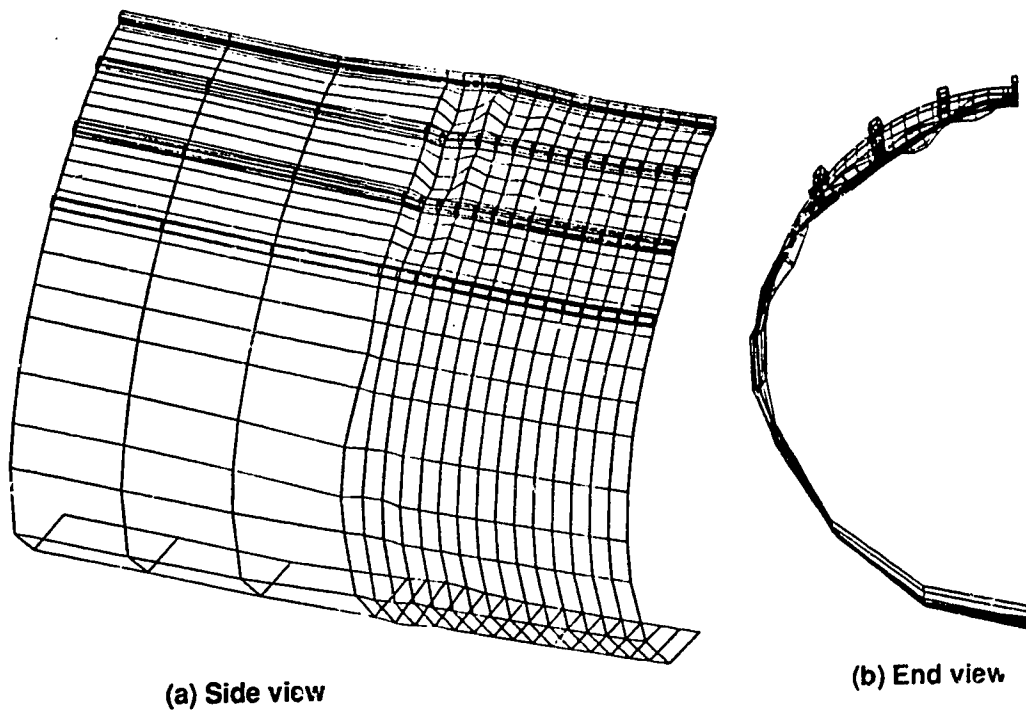


Figure 4.15 Deformed shape of SB3b ($M = M_u$, $a = 30$)

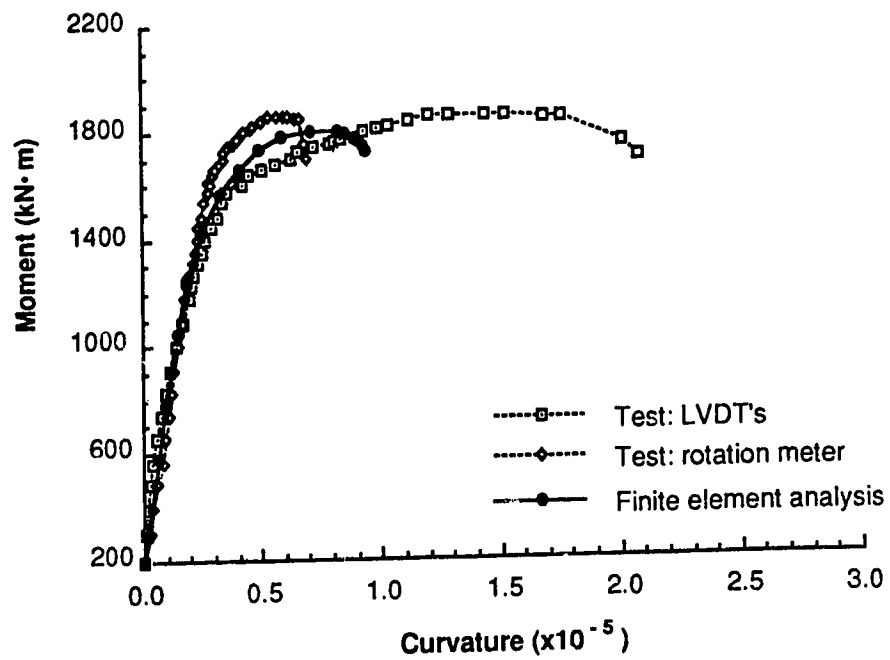


Figure 4.16 Moment versus curvature response of test SB4

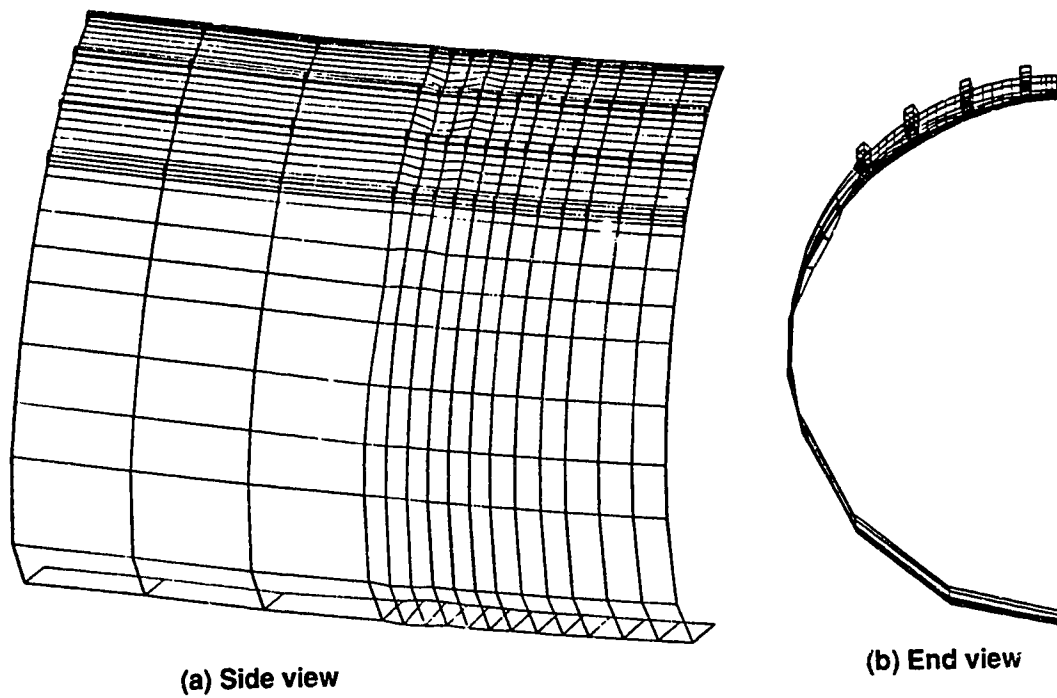


Figure 4.17 Deformed shape of SB4 ($M = M_u$, $a = 30$)

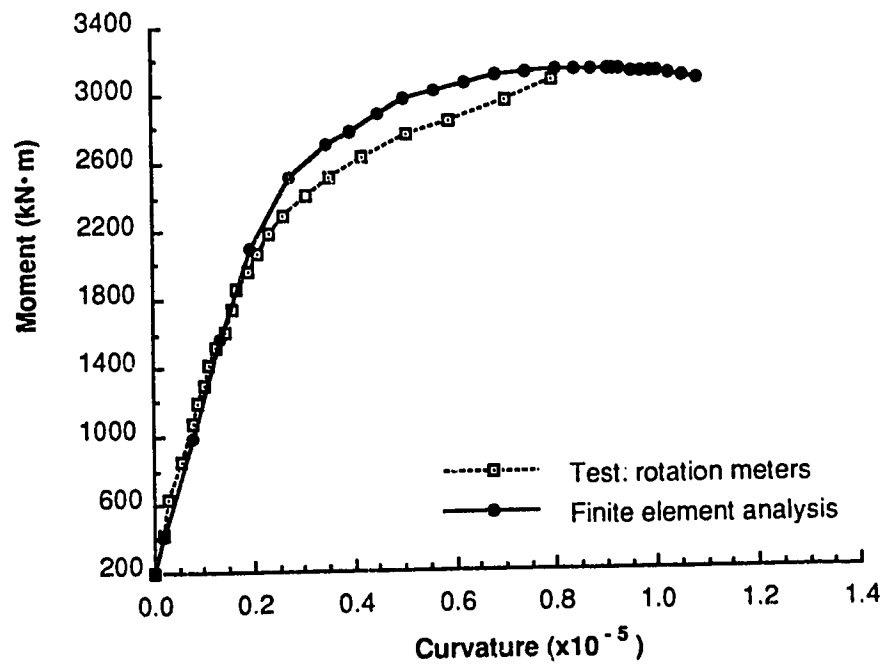


Figure 4.18 Moment versus curvature response of test SB1

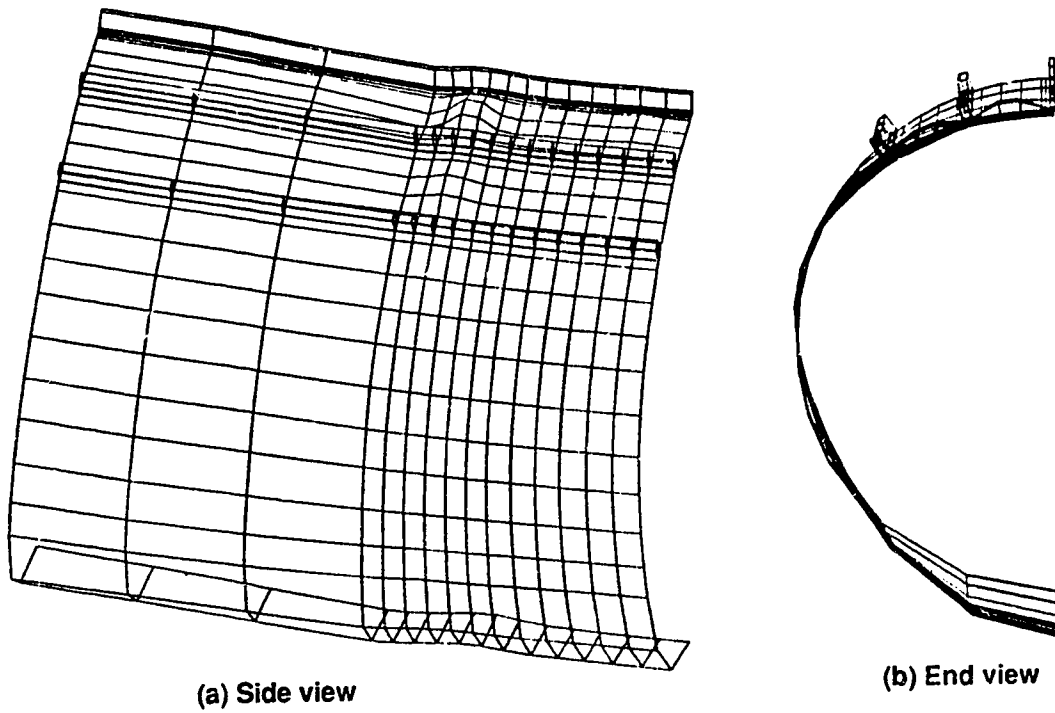


Figure 4.19 Deformed shape of SB1 ($M=M_u$, $a = 15$)

CHAPTER FIVE

FINITE ELEMENT ANALYSIS FOR PARAMETRIC STUDY**5.1 General**

Large-scale testing of physical specimens is the most direct and reliable approach for examination of the behavior of structural components. Such tests are expensive, however, and it is unusual to be able to test a large enough number of specimens so as to adequately examine the parameters involved. A more practical approach is first to establish the validity of a proposed method of analysis on the basis of physical tests that represent reasonable bounds to the problem, and then to further explore the effect of the different parameters using the analytical tools.

The situation just described applies to fabricated steel cylinders that use longitudinal stiffeners—there are relatively few test results available, even including those carried out in the study reported herein. However, the numerical simulation of the large-scale experiments presented earlier shows that finite element analysis is capable of accurately predicting the bending behavior of thin-walled longitudinally stiffened cylinders. Thus, finite element analysis will be used to explore the parameters involved, principally the geometry of the cylinders and stiffener arrangements. Cylinders with broad shell panels between stiffeners and those with R/t ratios above 200 are of special interest in this numerical study.

The finite element model employed herein was essentially the same as that developed in Chapter Four and used in the simulation of the experimental work. However, some modifications were made to suit the range of parameters. Based on examination of the sources and patterns of initial imperfections and residual stresses, the measured initial imperfections and residual stresses of specimen SB2 were modified and then used for the cylinders of the numerical study. Thirteen cylinders were analyzed for the purpose of parametric study. To explore the effect of residual stresses and initial imperfections, some of these cylinders were reanalyzed with different levels of residual stresses and initial imperfections.

5.2 Selection of Parameters

The most crucial geometric parameters of a longitudinally stiffened cylinder subjected to bending are the radius-to-thickness ratio (R/t), the angle covered by the stiffeners (Φ), and the ratio of stiffener spacing to shell thickness (s/t). The failure mode and the load capacity of the cylinders are controlled mainly by these parameters.

The R/t ratio is important because it reflects the resistance of cylindrical shells to local buckling. With an increase of R/t , which is equivalent to a decrease of the curvature, the out-of-plane stiffness of a curved panel of a given circumferential width is reduced. Moreover, in the case of bending, a large R/t ratio causes a nearly uniform distribution of compressive stress in the most highly stressed panels. This leads to a lower level of buckling stress than would occur in a shell with a higher stress distribution gradient resulting from a small R/t ratio. In this study, cylinders in three groups with different R/t ratios were analyzed. The values selected were 120, 240 and 360: these are considered to be in the range of industrial structures.

The parameters Φ and s/t reflect the stiffening of the shell. The specimens in the physical experiments had a relatively small spacing between stiffeners as compared to the shell thickness ($s/t = 38$ to 57). Because the panels between the stiffeners were thereby relatively narrow, general buckling, which involves both the shell and the stiffeners, became the dominate failure mode in the stiffened region and shell buckling between stiffeners was excluded in such an arrangement. The failure modes of these specimens were, therefore, solely dependent on the angle Φ . Cylinders with small angles ($\Phi = 33^\circ$ for the 5 mm thick specimen SB2 and $\Phi = 64^\circ$ for the 3 mm thick specimen SB3a) failed in shell buckling outside the stiffened area. Those having broad angles ($\Phi = 76^\circ$ for the 5 mm thick specimen SB1 and $\Phi = 89^\circ$ and 95° for the 3 mm thick specimens SB4 and SB3b) reached a high ultimate moment based on general buckling.

Large s/t values (up to 108) were used in the parametric study in order to observe the behavior of broad shell panels. Meanwhile, the selection of Φ values had to satisfy the limitation that the number of stiffeners must be an integer and that identical values of s/t and Φ were desirable for different R/t values. Two angles, 51.6° and 77.3° , were selected in order to compare the effect of Φ . The 51.6° angle appeared to be close to the boundary between buckling inside the stiffened area and buckling outside the stiffened area for a 5 mm cylinder, while the 77.3° angle guarantees failure within the stiffened area.

Other parameters that could also affect the behavior and capacity of a stiffened cylinder are the shell thickness and the size of stiffeners. The test results indicated that the shell thickness (t) might contribute to the normalized moment capacity, expressed as the ratio of the ultimate moment over the plastic moment. A 5 mm thick cylinder with the same R/t ratio may exhibit a higher moment ratio than its 3 mm counterpart, especially for the case of local shell buckling. This is due to the high levels of residual stresses and imperfections that were found in the 3 mm specimen (SB3a) from laboratory measurements. The thickness of fabricated cylinders used for conveyor galleries is usually in the range of 5 to 9 mm. Considering that imperfections and residual stresses measurements were available for a 5 mm thick specimen (SB2), the thickness of 5 mm was chosen for all cylinders in this study.

The cylinders selected for the numerical analysis and their parameters are listed in Table 5.1. They are in three groups, associated with the different R/t ratios. Within each group, there are two angles of Φ , and two types of stiffener spacing for each value of Φ . Such an arrangement provides an opportunity to observe the effect of different parameters. All of the twelve specimens in the three groups use the same size stiffeners (HSS 50.8 x 25.4 x 3.18). Nevertheless, cylinder S25, which is similar to S22 in all aspects except that the stiffeners are of small size (HSS 25.4 x 25.4 x 2.54), was added to explore the significance of stiffener size, *per se*.

5.3 Configuration

Longitudinally stiffened cylinders used in practice have long spans in the range of 15 to 20 times the diameter. The boundary conditions of a failed region would be provided by substantially intact shell and stiffeners. It would thus be desirable to model full length cylinders. However, limitations on memory size and CPU time expectations on a workstation computer would not allow this. Therefore, short models with controlled boundary conditions would have had to be used in the parametric study.

On a preliminary basis, two cylinders (S24a and S24b) were analyzed in order to observe the behavior of a short cylinder without thick end segments. These two cylinders were identical to S24 in all aspects except that they did not contain the thick end segments. Both S24a and S24b have rigid beam elements attached to their ends, similar to those described in Section 4.3.3. The difference between S24a and S24b is in the axial stiffness

of the beam elements. In S24a, it was reduced to zero so that the shape of the end cross-section can deform in its plane. The axial stiffness was defined to be nearly rigid in the case of S24b.

Figures 5.1 and 5.2 show the failure modes of S24a and S24b, in which the displacement is amplified by the scale factor a . For both cylinders, the failure occurred at the end edge where the nodal forces were applied. Due to the flexibility of the cross-section, the buckling deformation of S24a (Figure 5.1) was localized at the loaded edge of the compression zone. The maximum moment was 4152 kN·m, which is only 71% of the capacity of S24 (5846 kN·m). For S24b, when the shell at the compression zone buckled the rigid round shape forced the rest of the cross-section to deflect with the buckled shell at the top (Figure 5.2). Such an interaction strengthened the end portion artificially and the cylinder reached a failure load of 6396 kN·m, which is 9.4% higher than that of S24.

The failure modes of both S24a and S24b are not desirable because local buckling occurred at the loaded edge where the continuity of the shell disappears. The applied nodal forces were formulated according to beam theory (Equation 4.5); these forces are significantly different from the internal forces that exist in a continuous shell. For a short cylinder without thick segments, the only way to account for the continuity is to apply a set of work-equivalent nodal forces formulated from shell theory. In addition, these forces must be able to redistribute themselves when the stiffness changes because of material and geometrical nonlinearities. Such a procedure involves complicated iterations and is impractical to incorporate into an analysis.

In order to avoid the failure patterns observed in S24a and S24b, the beam stresses applied at the end must be transformed into shell forces. A thick segment can perform such a transformation and its stiffness can prevent local buckling near the edge. It was, therefore, decided that the configuration of the test specimens described in Chapter Three and Four is best suited for the parametric study. In this configuration, a short test span is bounded by two thick shell segments. Loads and boundary conditions are applied to the ends of the thick segments.

It is interesting to note that in the early experimental investigations of large diameter fabricated cylinders (Stephens *et al.*, 1982), the short specimens used for preliminary tests were designed without thick end segments and, consequently, the failure occurred at the loaded edge. To avoid such failure patterns, thick end segments were used in later experiments at the University of Alberta.

5.4 Numerical Model

Similar to the model shown in Figures 4.2 and 4.3, the selected configuration of the finite element model used herein has a 7.5 mm thick end segment and a rigid end cross-section. The length of each of the central and end segments is equal to the radius of the cylinder and only one-quarter of the cylinder is modeled. The boundary conditions are the same as those used for the simulation of experimental work. The shells and stiffeners are discretized using sixteen node and four node degenerated plate-shell elements. Rules of numerical integration similar to those described in Section 4.3 are also applied to these elements.

Since a fine mesh is needed to simulate the local buckling behavior, a large number of nodes are required to discretize a stiffened cylinder, especially when it has a large diameter or many stiffeners. However, the total number of degrees of freedom has to be limited according to the capacity of the computer. As a result, a fine mesh was used only in the test segment near its conjunction with the thick segment, that is, where the local buckling is most likely to occur. The mesh elsewhere, particularly in the thick segment, was relatively coarse so that the size of the stiffness matrix could be reduced.

Hot-rolled structural steel as typically used in industry was chosen to be the cylinder material. It has a yield stress of 300 MPa, which is the same as the nominal yield stress of CSA G40.21 300W steels. Young's modulus was taken as 200 000 MPa. The stress versus strain behavior was assumed to be elastic-perfectly plastic.

The HSS stiffeners had nominal dimensions of 50.8 x 25.4 x 3.18 and were used for all cylinders except for S25, which had stiffeners of a smaller size (HSS 25.4 x 25.4 x 2.54). The average stress versus strain curve of the stiffener material was assumed to be the same as that measured from the stiffeners used in test SB2 (Figure 4.7).

5.5 Initial Imperfections

The measured imperfections in the test specimen SB2 were found to have fundamental patterns similar to those reported for large diameter stiffened cylinders ($R = 4500$ mm) fabricated for offshore structures (Dwight 1982). Because of the similarities between specimen SB2 and the cylinders of this study in shell thickness and

fabrication process, the imperfections of SB2 were used as a basic model for all cylinders in the parametric study. However, some modifications were made to suit the differences in radius and stiffener spacing.

As discussed in Chapter Three, there are three types of imperfections. Type (a) imperfections (out-of-straightness) mainly arise from the deflection due to the weight of the cylinder when only the ends are supported. The shrinkage of circumferential girth weld is the major cause of the variation of radii, which is categorized as Type (b) imperfections. These two types of imperfections are essentially functions of the radius. Taking the example of Type (b) imperfections, which are more influential on local buckling than Type (a) imperfections, the amplitude of imperfections are linearly proportional to the radius, assuming that the shrinkage is in proportion to the length of the weld.

Out-of-roundness, or Type (c) imperfections, refers to the local shell deflection from the profile of a perfect shell in the cross-sectional view. These imperfections are the combined consequence of ovalization and the fabrication procedure (cold-forming, longitudinally seam welding, and welding of stiffeners). Since interior frames were installed at each end of the test specimens to maintain the circular shape of the cross-section (Section 3.2.1), ovalization due to the distributed shell weight is less significant than are the imperfections arising from fabrication. In the process of fabrication, cold-forming and longitudinal seam welding give the cylinder a pear shape, as shown in Figure 3.4. Additionally, the stiffener welding introduces circumferential waves having a wave length which matches the stiffener spacing. These waves also coincide with shell buckling waves. The deformation is also concentrated in the compression zone. Therefore, this portion is considered the most critical of Type (c) imperfections for shell buckling and general buckling. Since the residual deformation is associated with the size of weld and thickness of the parent material, the magnitude of the imperfections that arise from stiffener welding may be assumed to depend on the shell thickness and weld size, and to be independent of the radius.

To summarize, the following assumptions were made in the determination of the initial imperfections in the cylinders of the parametric study.

- (1) Type (a) and Type (b) imperfections are in proportion to the radius of the cylinder.

- (2) The magnitude of Type (c) imperfections depends only on the shell thickness. However, the width of circumferential waves in the stiffened area, induced by stiffener welding, varies according to the spacing between stiffeners.

Based on these assumptions, the imperfection data of SB2 were divided into three categories and then processed separately. Types (a) and (b) were amplified in accordance with the radius of the model. The magnitude of Type (c) imperfections was the same as that of SB2 because the nominal shell thickness of all models was identical to that of SB2. However, in the stiffened area, the imperfections of Type (c) were circumferentially scaled from SB2 to the model in terms of the stiffener spacing of the model. In this way, the circumferential waves resulting from stiffener welding could match the stiffener spacing of the model. Following this process, the individual results were superimposed to produce initial imperfections for the finite element models of the parametric study.

5.6 Residual Stresses

The various sources of residual stresses were examined in Chapter Three. The longitudinal residual stress resulting from stiffener welding was found to be the most significant effect in the compression zone, where local buckling may take place. As was done in the finite element models used for the simulation of the experiments, only this part of residual stresses was considered in the parametric study. The distribution pattern of residual stresses proposed in Section 4.7 for test simulation was also adopted herein.

Since the nominal shell thickness and the stiffener size of specimen SB2 were identical to those of the cylinders used for the parametric study and the welding procedure was assumed to be the same, the measured residual stresses from SB2 were applied to the numerical models after some modification. As reported in Chapter Three, the measurements of the 5 mm thick specimen, SB2, identified the average compressive residual stress at about 35% of the yield stress in the stiffened panel and at about 15% of the yield stress outside the stiffened area. The strain gages, which were mounted on the inner surface of the shell underneath the stiffeners before welding, measured the resulting tensile residual strain at about 60% of the yield strain.

The tensile residual stress is known to be controlled by the shell thickness and the size of the weld (Faulkner 1977). For cylinders which share the same shell thickness, size of stiffeners and welding procedure, like SB2 and the cylinders of the parametric study,

the distribution of tensile residual stresses should be similar in each case. Meanwhile, the compressive residual stresses, existing in the shells inside as well as outside the stiffened region, must act to balance the tensile stresses. The compressive stresses outside the stiffened region would not be significantly affected by different stiffening patterns. However, the compressive residual stresses in the stiffened panels varies with the stiffener spacing. Previous research (Masubuchi 1980, Faulkner 1977) indicated that the compressive residual stress in the stiffened panels is inversely proportional to the spacing, s . For a large spacing, the lower bound appears to be the stress level outside the stiffened area, which in SB2 was 15% of the yield stress.

For the purpose of this study, the tensile stress (σ_{rt} in Figure 4.5) and the compressive stress in the shell outside the stiffened area (σ_{rc2}) were assumed to be the same as those of SB2. The compressive residual stress in the shell between stiffeners (σ_{rc1}) was assumed to vary according to stiffener spacing (s , in mm) as

$$\sigma_{rc1} = (0.15 + \frac{36}{s}) \sigma_y \quad (5.1)$$

For $s = 180$ mm, $\sigma_{rc1} = 0.35\sigma_y$, which corresponds to the level measured in SB2. As s increases, σ_{rc1} decreases and approaches $0.15\sigma_y$ when s becomes very large.

5.7 Buckling Behavior

The results of finite element analysis showed that all cylinders listed in Table 5.1 failed by compressive buckling in the stiffened area. However, within this region two buckling modes, general buckling and shell buckling between the stiffeners were observed. Figures 5.3 to 5.14, in which the displacement is amplified by the scale factor a , show the buckled shapes of the 12 cylinders in the three R/t groups. Large buckles in the stiffened area, which usually are in the vicinity of girth weld joining the two segments, are observed in the deformed shapes.

5.7.1 Curvature and Displacement

Figures 5.15 to 5.26 are the moment versus curvature and moment versus displacement graphs for selected cylinders, and they represent the different failure modes explicitly. The curvature was calculated from the U_x displacements at the top and bottom of

the cylinder at the cross-section joining the two segments. Since the deformed cross-section may not be in a plane, the calculated curvature does not carry the same definition of curvature as in a classic beam. It serves as an one-dimensional index to measure the rotation capacity of the central thin cylinder, which is a three-dimensional shell. For convenience of comparison, the moment versus curvature graphs for the cylinders in a given R/t group are drawn to the same scale.

The nodes used for the displacement curves are either at the top or at the bottom of the largest buckling waves. The amplitude of the largest buckle of the stiffeners, the shell between stiffeners, and the shell outside the stiffened area are described by three nodes of each cylinder. However, the three nodes may not be in the same cross-section since the wave length of stiffeners is greater than that of the shells and the two types of waves are not synchronous.

The displacement in these graphs was calculated as

$$d = ((U_y - U_{y0})^2 + (U_z - U_{z0})^2)^{1/2} \quad (5.2)$$

where U_y and U_z are the total displacements at the current load level, and U_{y0} and U_{z0} are the initial displacements resulting from the temperature loading which imposes residual stresses. As defined in Equation 5.2, d is the y - z plane projection of the overall displacement in the three-dimensional space. It consists of two components: overall beam deflection and local shell deflection related to the buckling. The first part dominates the earlier stage of the loading history, while the large increase in the later stage reflects the second part.

5.7.2 Failure Mode

The buckling mode, general buckling or shell buckling in the stiffened area, can be identified by examining the moment versus curvature and the moment versus displacement behavior. As will be discussed later, the characteristics of the moment versus curvature behavior are significantly different in the two failure modes. Such differences also exist in the moment versus displacement curves. Since both the stiffeners and the shell are involved in the general buckling, the development of local deflections of stiffeners and shells are nearly simultaneous. However, in the case of shell buckling, the displacements of the stiffeners become noticeable much later, and they are much smaller than those of the shell.

Figures 5.17 and 5.18 of cylinder S21 show typical behavior for the general buckling case. The responses of moment versus curvature or moment versus displacement depart from the linear curve about half-way towards failure. A significant load increase exists between the onset of buckling and the ultimate point. Before and after the ultimate load point, the rising and descending rates are relatively mild. In addition, the deflections of the stiffeners and of the shell between stiffeners take place almost simultaneously. The behavior of S13 (Figure 5.15) and S31 (Figures 5.23 and 5.24) show that they also fall into the category of general buckling.

The cylinders with broad panels or large R/t ratios, such as cylinder S24, are more likely to fail in shell buckling between stiffeners. In Figure 5.21(a), the moment versus curvature response of S24 is essentially linear up to failure. The response in the vicinity of the ultimate point is illustrated to a large scale in Figure 5.21(b), and it shows that the curve turns downwards sharply after the ultimate load is reached. Failure immediately follows the onset of buckling. The moment versus displacement curves (Figure 5.22 with illustrated detail near the ultimate point) show that buckling deformation is concentrated in the shell between stiffeners. This can also be found from the buckled shape of the cylinder (Figure 5.10). For failure by shell buckling, the deformation corresponding to the ultimate load is much smaller than that observed in the general buckling case. For S24, the curvature at the ultimate point is only 47% of that of S21, which failed in general buckling, even though the elastic flexible stiffness of the two cylinders is only 6% different. It is evident that failure by shell buckling is an abrupt and non-ductile phenomenon.

Similar behavior to that of S24 can be found in the responses of S14 (Figure 5.16), S23 (Figures 5.19 and 5.20), and S33 (Figures 5.25 to 5.26): they also failed by shell buckling. However, there are some differences in behavior among these cylinders because of different R/t and s/t ratios. These ratios reflect the shell stiffness and the support provided by the stiffeners, respectively. Failure of cylinders with small R/t or s/t ratios, such as S14 and S23, is less abrupt than that of S24 and S33, for example. Because of yielding and large deformation, a short, nonlinear portion exists before the ultimate point is reached. Additionally, the descending rate after the peak point is more gradual than that of S24 and S33 because of the interaction with the stiffeners. Even so, the sharp turning at the ultimate distinguishes the moment versus curvature behavior of shell buckling from that of general buckling, which exhibits a gradual and ductile pattern.

The ultimate capacity and failure mode for each of the cylinders examined in this parametric study are summarized in Table 5.2. Of the twelve cylinders in the three R/t groups, seven failed in general buckling. These seven cylinders have relatively small values of s/t . The capacity varied from 79% to 91% of the plastic moment, depending on the different parameters. The other five cylinders failed in shell buckling in the stiffened area, which is a reflection of their broad shell panels. The capacities in this category ranged between 53% to 78% of the full plastic moment.

5.8 Effect of Residual Stresses and Initial Imperfections

The initial imperfections and residual stresses described in Sections 5.5 and 5.6 were incorporated into the analysis of the cylinders listed in Table 5.2. To study their effect on the capacity of the models, some cylinders were subsequently reanalyzed with different residual stresses and initial imperfections.

The effect of compressive residual stresses is shown in Table 5.3. Listed are the ultimate moments of cylinders S12 and S22 for different residual stress levels. An increase of σ_{rc1} , the compressive residual stress in the shell between stiffeners, from $0.15\sigma_y$ to $0.35\sigma_y$ results in a reduction up to 1.4% in the bending capacity. Here, the values $0.15\sigma_y$ and $0.35\sigma_y$ are the lower and upper bounds of compressive residual stresses in the shell between stiffeners according to the measurements taken in SB2. As shown in Table 5.2, these two models (S12 and S22) failed in general buckling, and the ultimate loads were about 80% of the plastic moment. The results of Table 5.3 show that for the cylinders with a general buckling failure mode, the ultimate capacity is not sensitive to the level of the compressive residual stress in the stiffened panels.

Table 5.4 presents the results of additional analysis of test specimen SB2. The levels of residual stresses have various values in the three cases. An increase in the tensile residual stress by $0.1\sigma_y$ and a simultaneous reduction of the compressive residual stress by $0.05\sigma_y$ results in an increase in the ultimate load of about 6%. Additionally, a change of $0.1\sigma_y$ in the tensile residual stress has little effect on the capacity. Most of the 6% effect arises from the change of the compressive residual stress. The results of Table 5.4 shows that cylinders like SB2, which failed by shell buckling immediately after initial yield, are somewhat more sensitive to residual stresses than those that fail in general buckling.

The eight cylinders in the groups of $R/t = 120$ and 240 have also been analyzed without any initial imperfections present. Surprisingly, the ultimate moment points of the perfect cylinders were approached and then passed without any difficulties in the analysis. This is probably due to the presence of residual stresses. The behavior and failure mode were very much the same as those with initial imperfections. For the cylinders that failed in general buckling, the buckling waves of the perfect cylinders initiated at an early stage and were amplified as the load increased, in a manner very similar to their imperfect counterparts. The absence of the initial imperfections resulted in an increase in the bending capacity, which varied from 1% to 7% compared to the models with initial imperfections. The sensitivity is lower than that of elastic unstiffened shells. This is probably due to the inelasticity caused by the residual stresses, and due to the presence of longitudinal stiffeners (Hutchinson and Amazigo 1967). It should also be mentioned that the comparison is between the nonlinear ultimate load analyses, not between the bifurcation analysis and initial post-buckling analysis. Differences between the latter pair are expected to be more substantial.

5.9 Summary

In order to expand the data base collected from experimental research, cylinders with a wide range variation of parameters were analyzed using the finite element model established in Chapter Four. The parameters studied include the geometry and the stiffener arrangement of the cylinders. The measured initial imperfections and welding residual stresses of the test specimen were applied to the numerical models by mapping procedures. A discussion of the configuration of the finite element model was presented with the results of preliminary analysis.

Different buckling modes were found by examining the moment versus curvature and moment versus displacement behavior. The failure mode and ultimate capacity were identified and summarized. The cylinders that failed in general buckling exhibited good ductility. A relatively abrupt failure behavior is observed in the cases where shell buckling occurred. The effects of residual stresses and initial imperfections have also been studied. A further discussion of the effect of parameters (R/t , s/t , Φ , etc.) will be presented in the following chapter.

Table 5.1 Cylinders for the Parametric Study

Specimen	R/t	s/t	Φ (degree)	N ^a
S11	120	54	77.3°	4
S12	120	54	51.6°	3
S13	120	81	77.3°	3
S14	120	108	51.6°	2
S21	240	54	77.3°	7
S22	240	54	51.6°	5
S23	240	81	77.3°	5
S24	240	108	51.6°	3
S31	360	54	77.3°	10
S32	360	54	51.6°	7
S33	360	81	77.3°	7
S34	360	108	51.6°	4
S25	240	54	51.6°	5

^a Number of stiffeners.

**Table 5.2 Capacity and Failure Mode of Cylinders for
the Parametric Study**

Specimen	M_u (kN·m)	M_p (kN·m)	$\frac{M_u}{M_p}$	Failure mode
S11	2321	2542	0.91	general buckling
S12	2262	2477	0.91	general buckling
S13	2078	2447	0.85	general buckling
S14	1852	2370	0.78	shell buckling
S21	7960	10009	0.80	general buckling
S22	7680	9708	0.79	general buckling
S23	6499	9635	0.67	shell buckling
S24	5846	9288	0.63	shell buckling
S31	16526	22344	0.74	general buckling
S32	15757	21692	0.73	general buckling
S33	12776	21556	0.59	shell buckling
S34	11027	20750	0.53	shell buckling
S25	6404	9206	0.70	general buckling

Table 5.3 Effect of Compressive Residual Stress

Specimen	σ_{rc1} / σ_y	M_u (kN·m)	$\frac{M_u}{M_p}$
S12	0.35	2241	0.905
	0.28	2262	0.913
	0.15	2277	0.919
S22	0.35	7641	0.787
	0.28	7680	0.791
	0.15	7744	0.798

Table 5.4 Effect of Tensile and Compressive Residual Stresses

Specimen	σ_{rt} / σ_y	σ_{rc1} / σ_y	σ_{rc2} / σ_y	M_u (kN·m)	$\frac{M_u}{M_p}$
SB2	0.50	-0.40	-0.20	1898	0.975
	0.60	-0.35	-0.15	2007	1.031
	0.70	-0.35	-0.15	2018	1.036

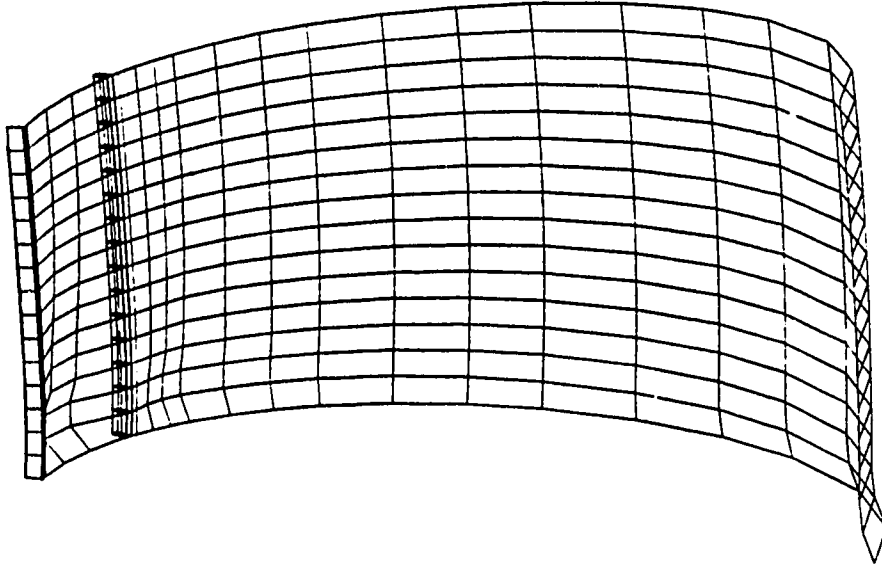


Figure 5.2 Deformed shape of S24b ($a = 50$)

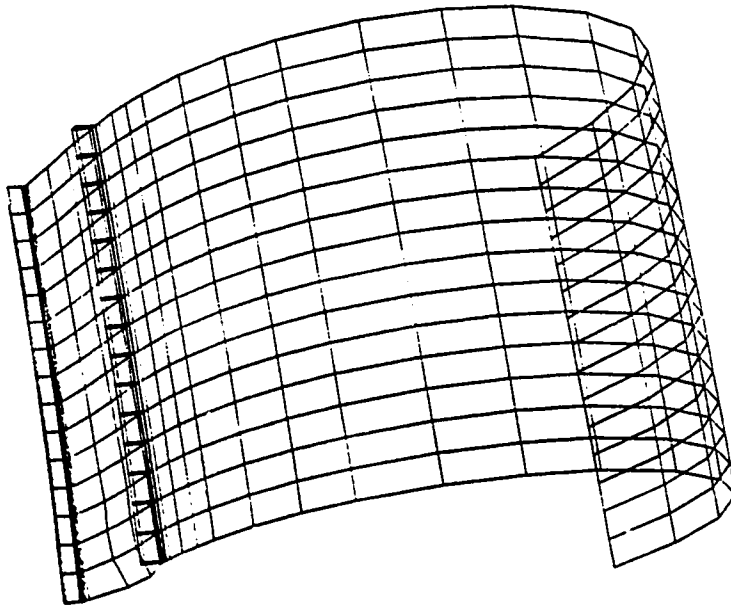


Figure 5.1 Deformed shape of S24a ($a = 50$)

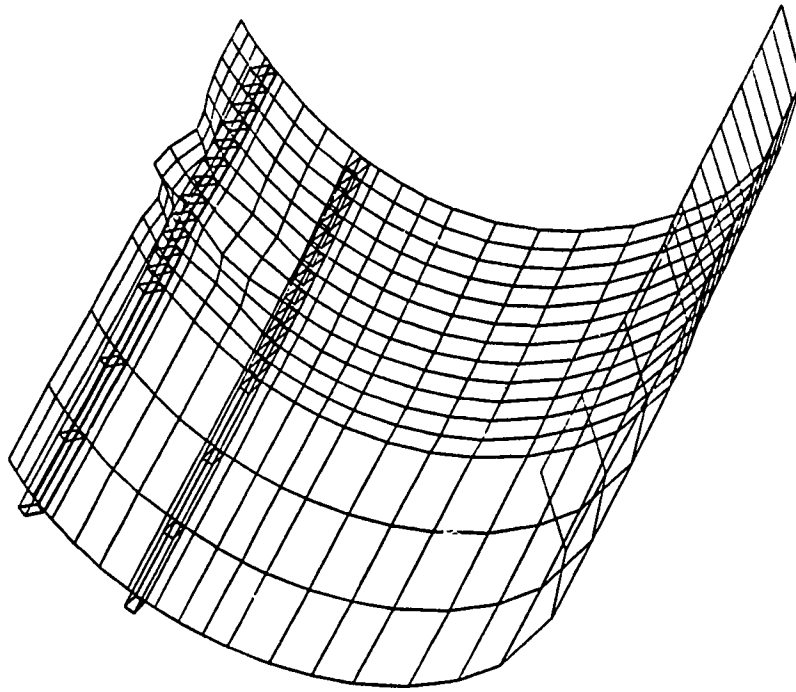


Figure 5.3 Deformed shape of S11 ($a = 10$)

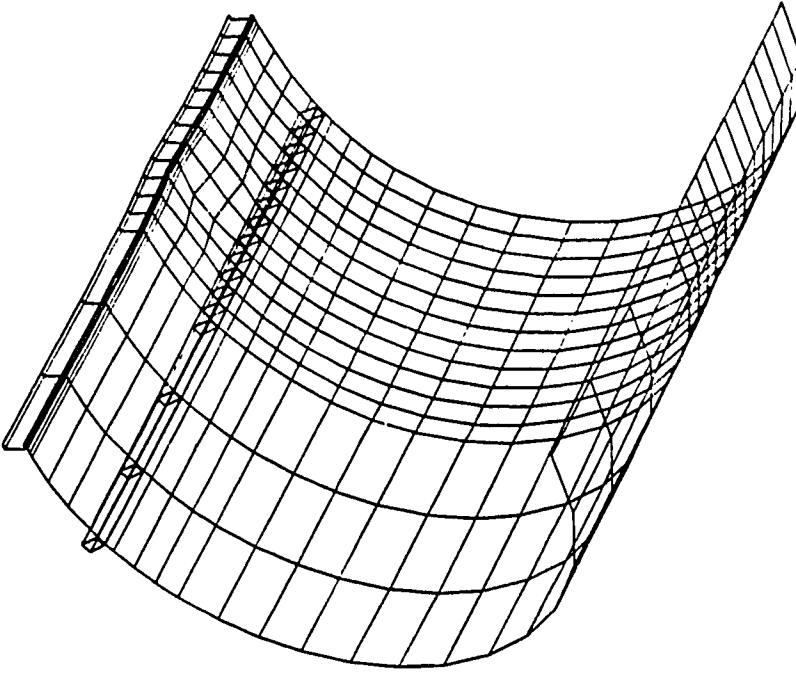


Figure 5.4 Deformed shape of S12 ($a = 10$)

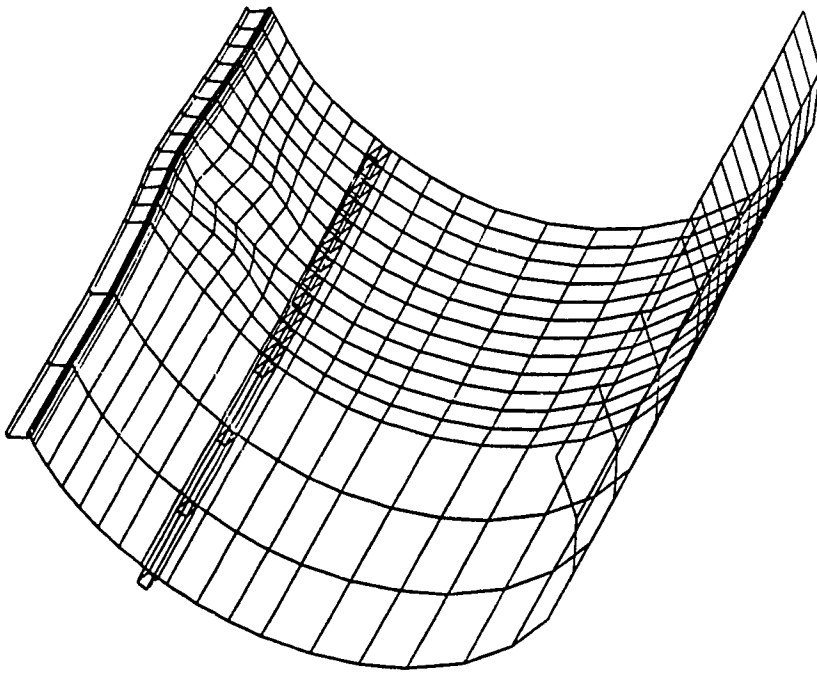


Figure 5.5 Deformed shape of S13 ($a = 10$)

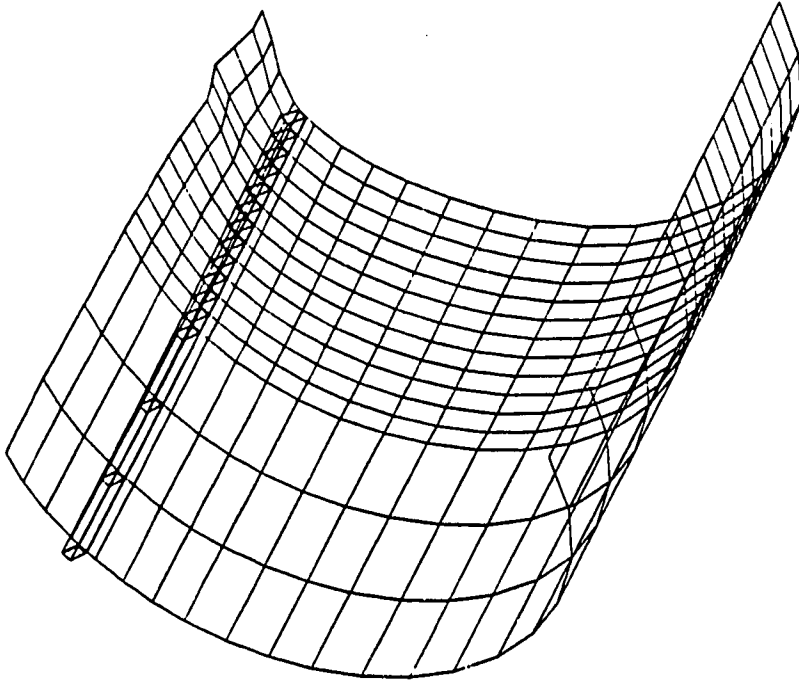


Figure 5.6 Deformed shape of S14 ($a = 10$)

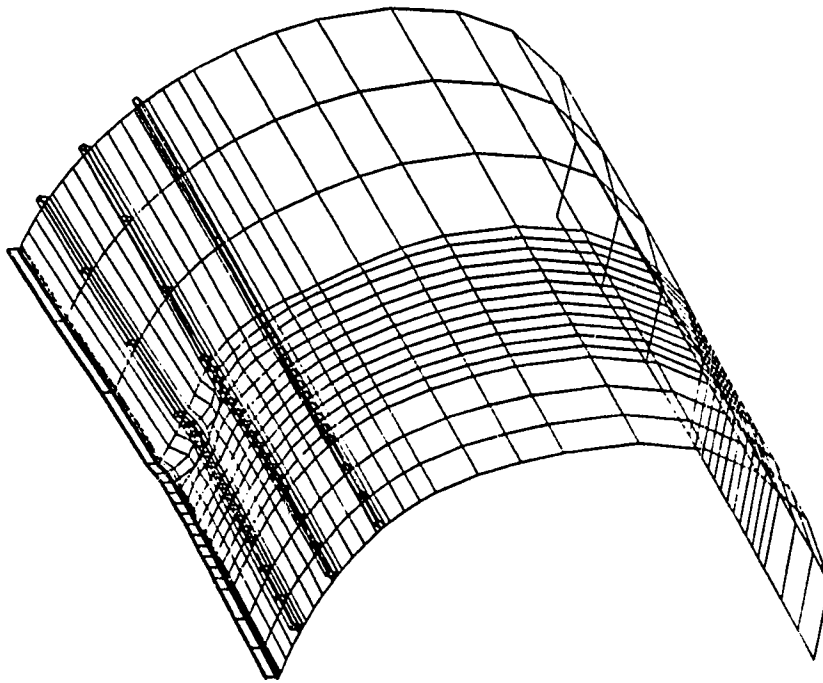


Figure 5.7 Deformed shape of S21 ($a = 10$)

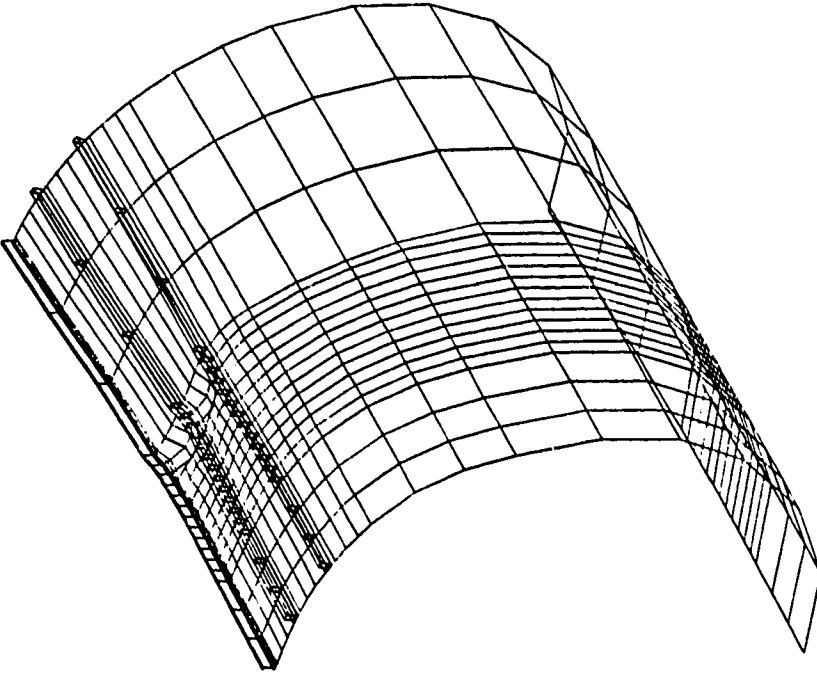


Figure 5.8 Deformed shape of S22 ($a = 10$)

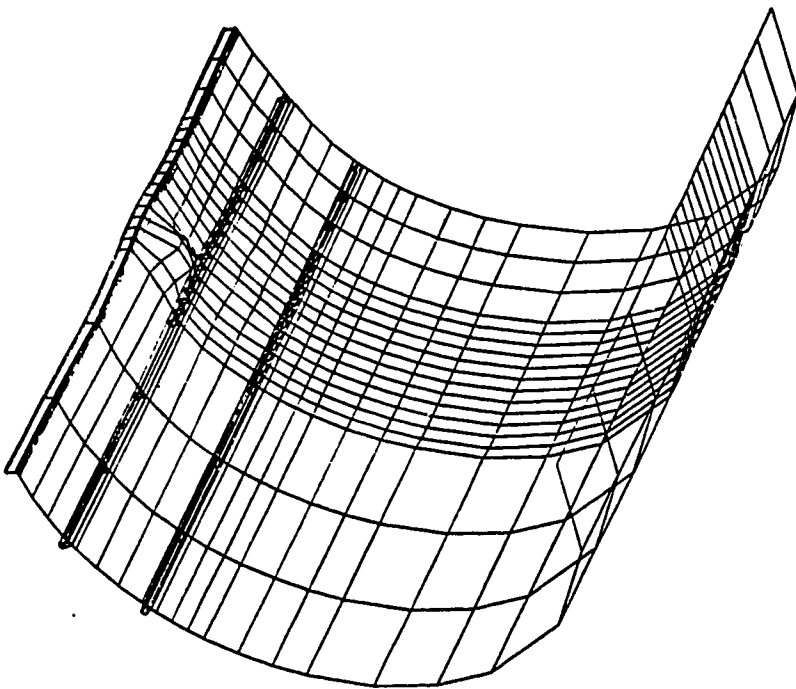


Figure 5.9 Deformed shape of S23 ($a = 10$)

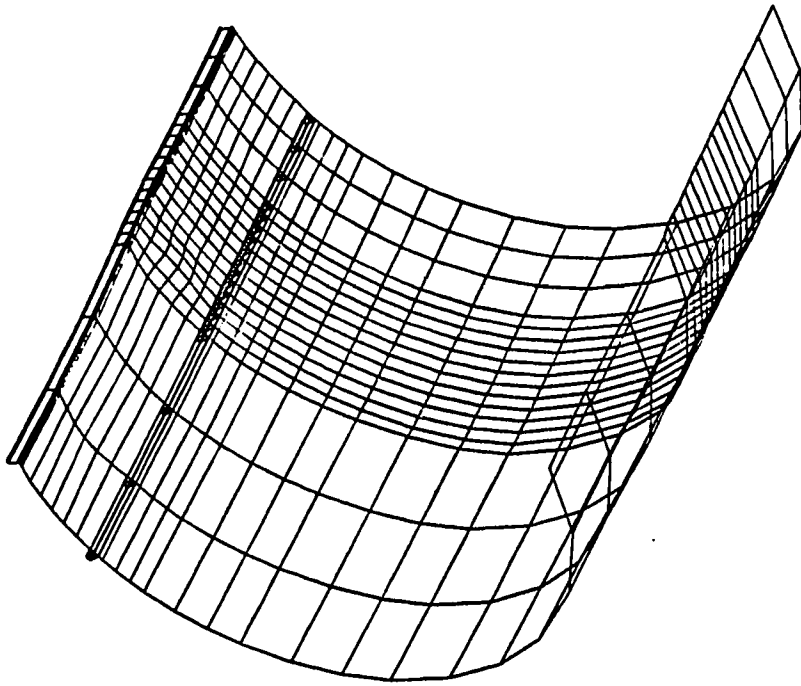


Figure 5.10 Deformed shape of S24 ($a = 30$)

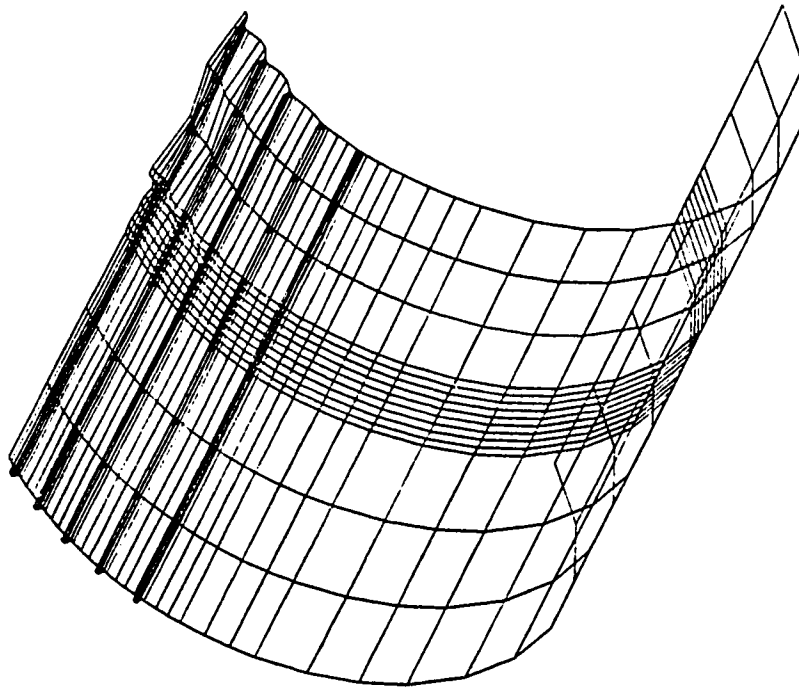


Figure 5.11 Deformed shape of S31 ($a = 10$)

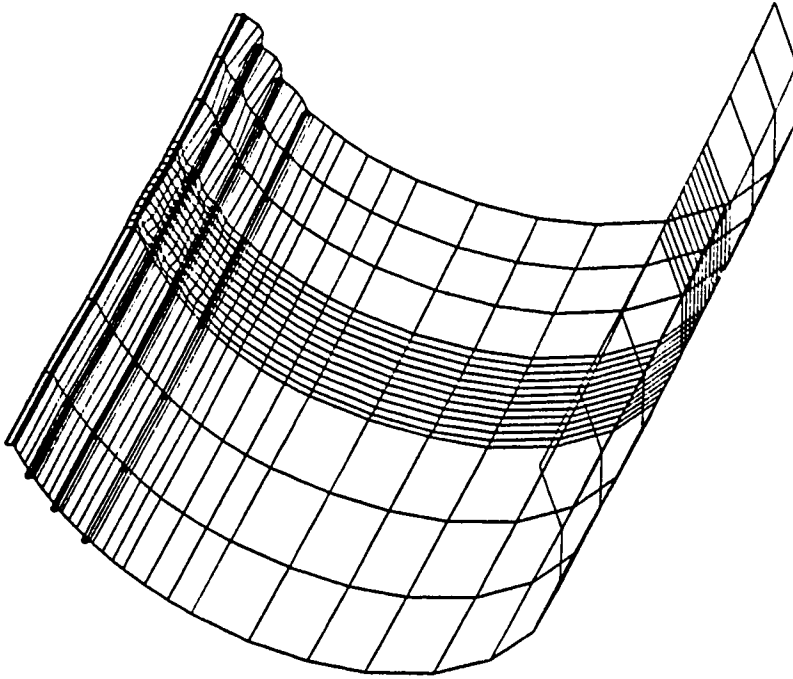


Figure 5.12 Deformed shape of S32 ($a = 30$)

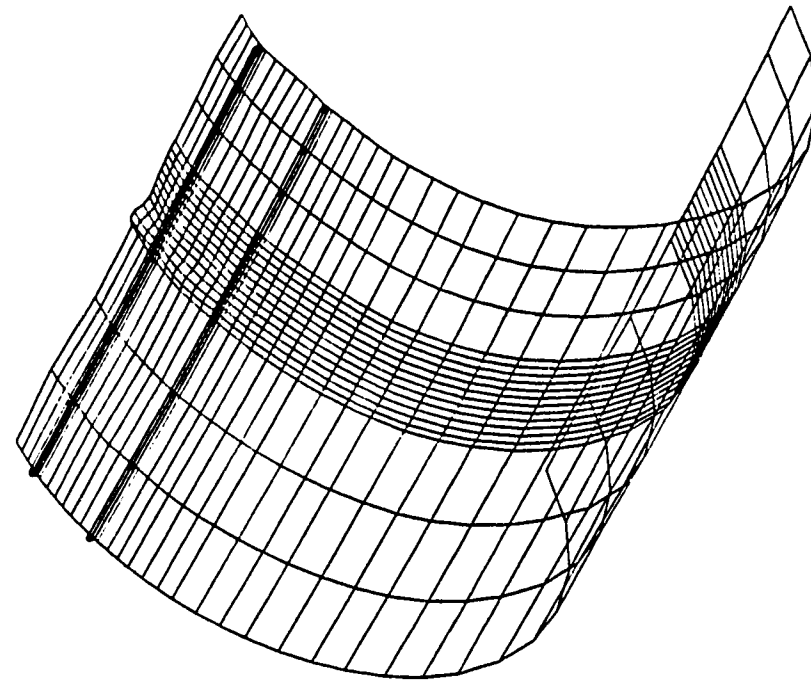


Figure 5.14 Deformed shape of S34 ($a = 50$)

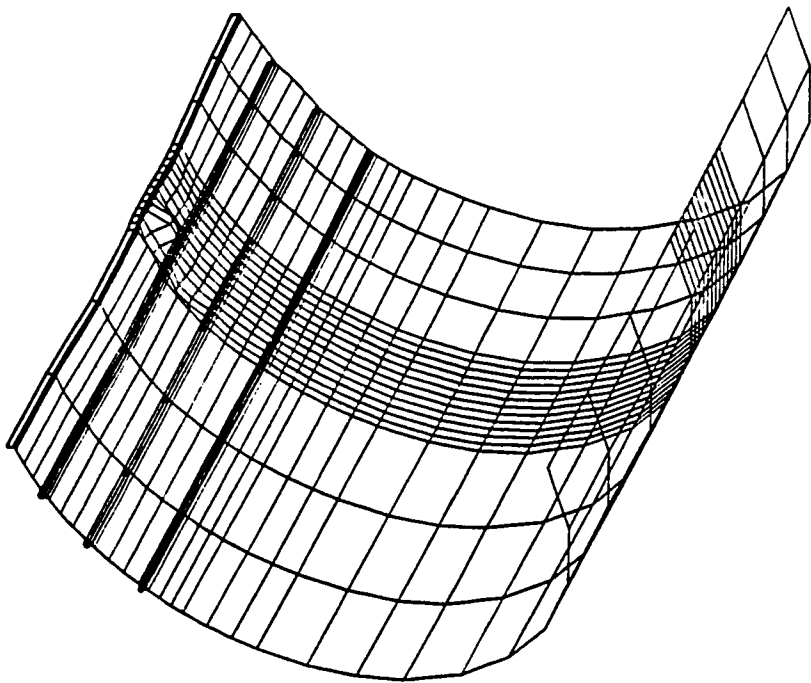


Figure 5.13 Deformed shape of S33 ($a = 30$)

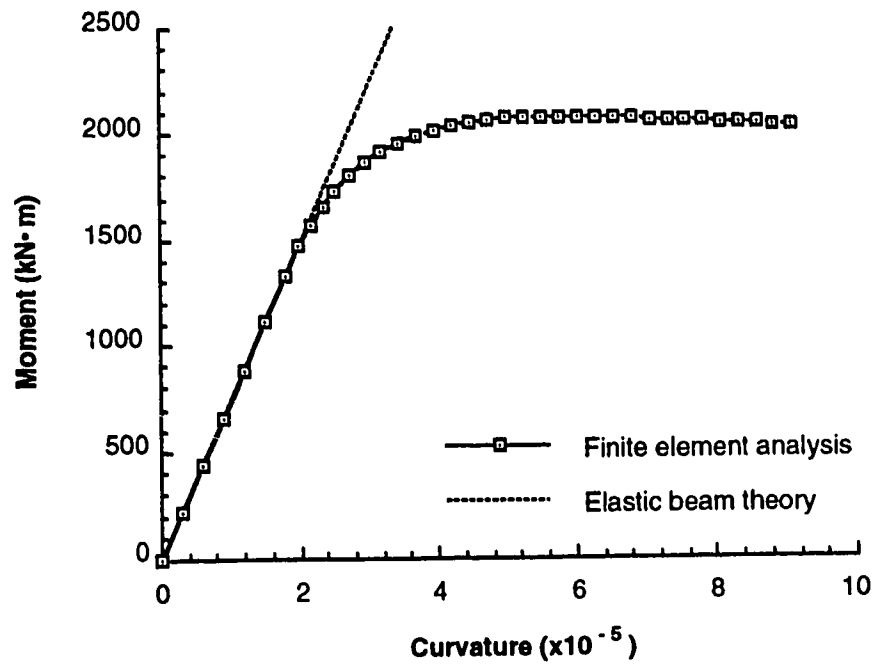


Figure 5.15 Moment versus curvature response of S13

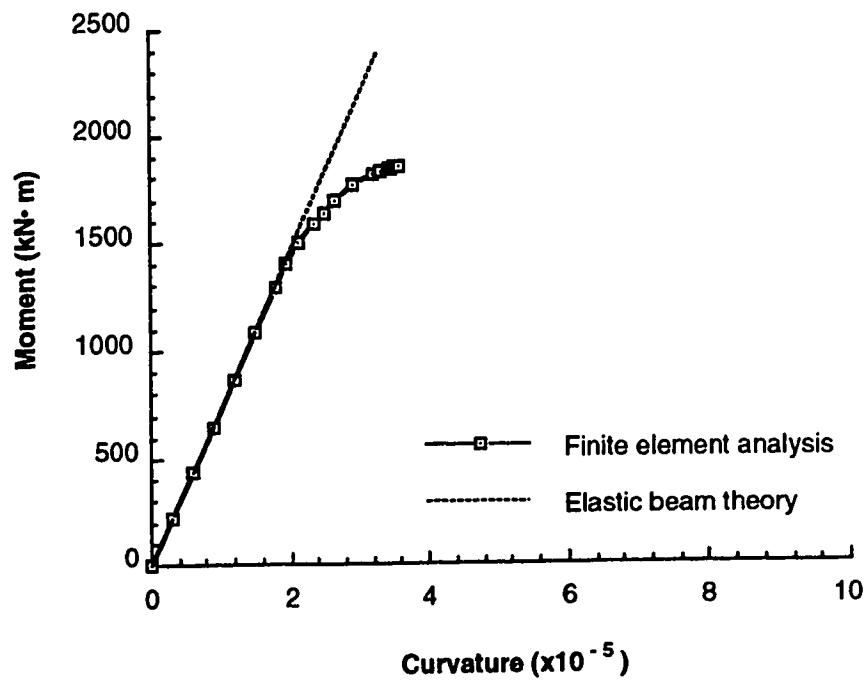


Figure 5.16 Moment versus curvature response of S14

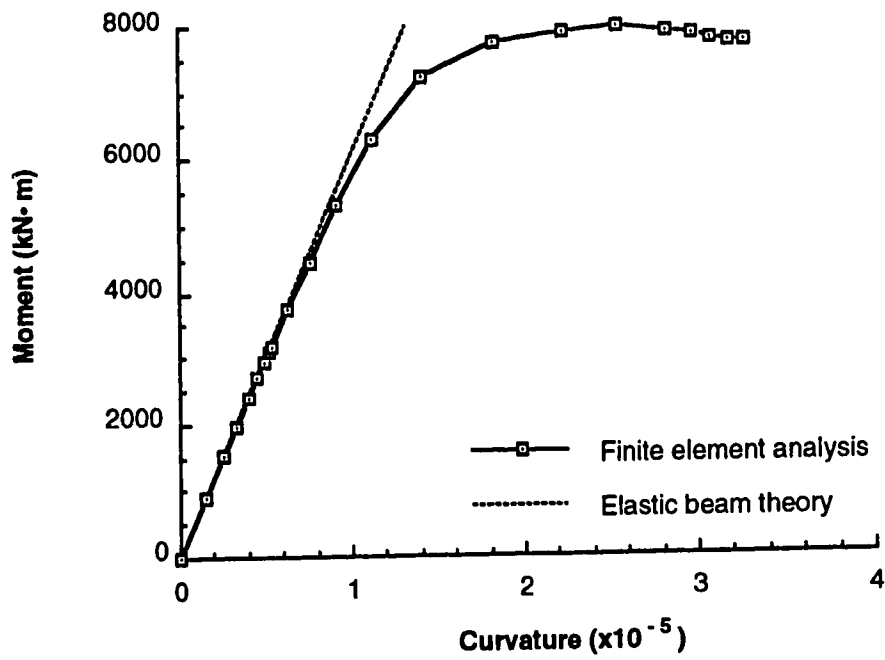


Figure 5.17 Moment versus curvature response of S21

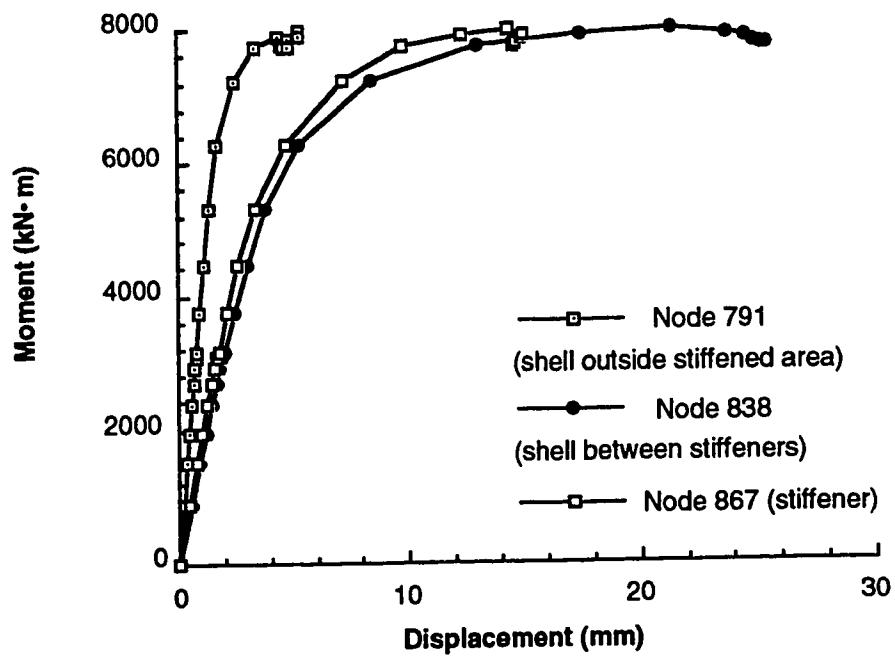


Figure 5.18 Moment versus displacement response of S21

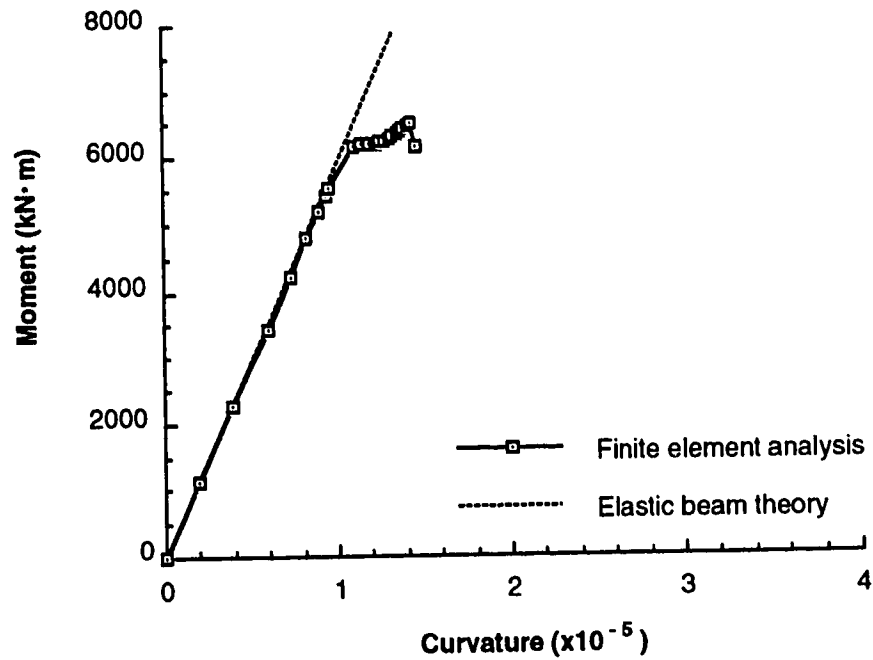


Figure 5.19 Moment versus curvature response of S23

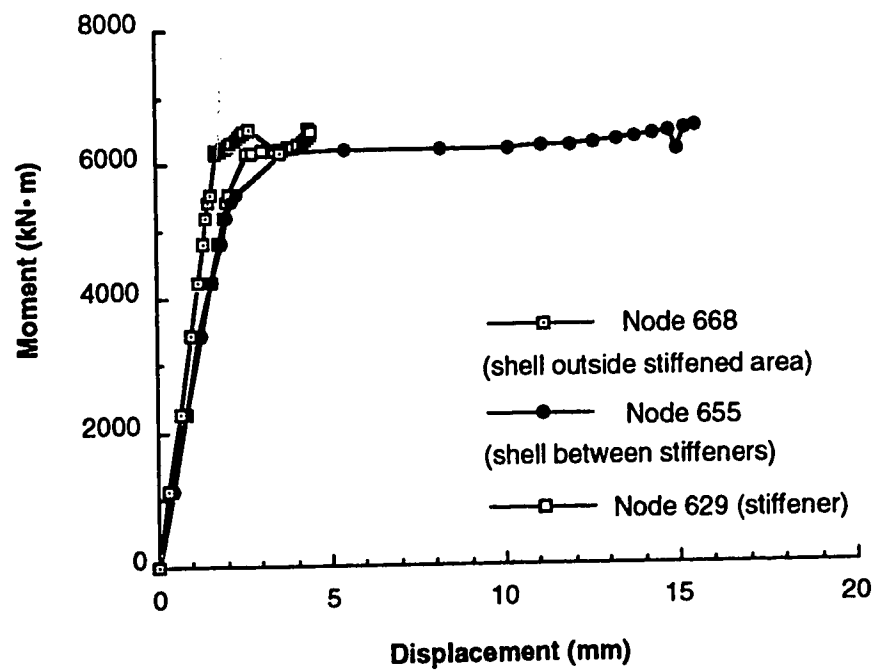
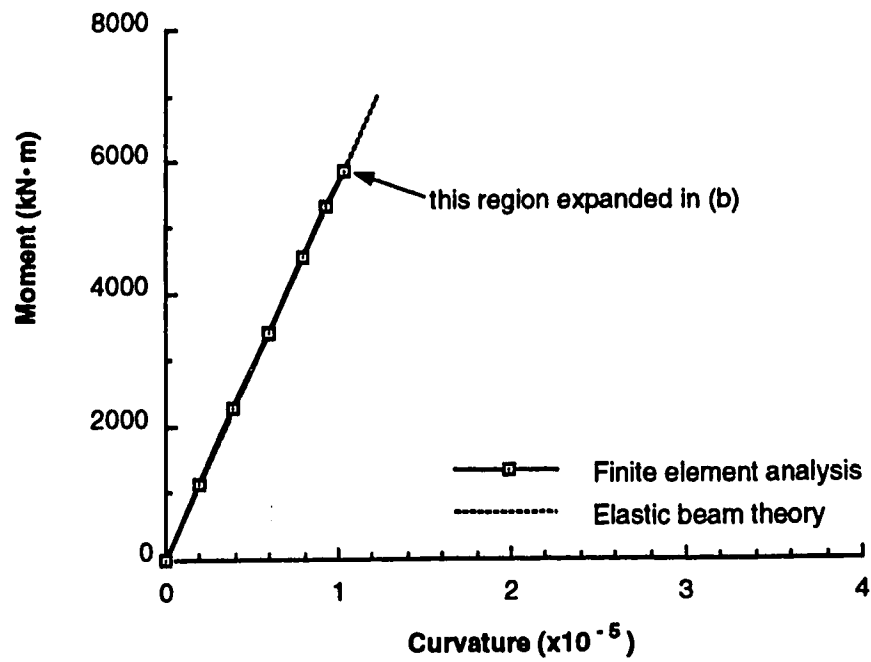
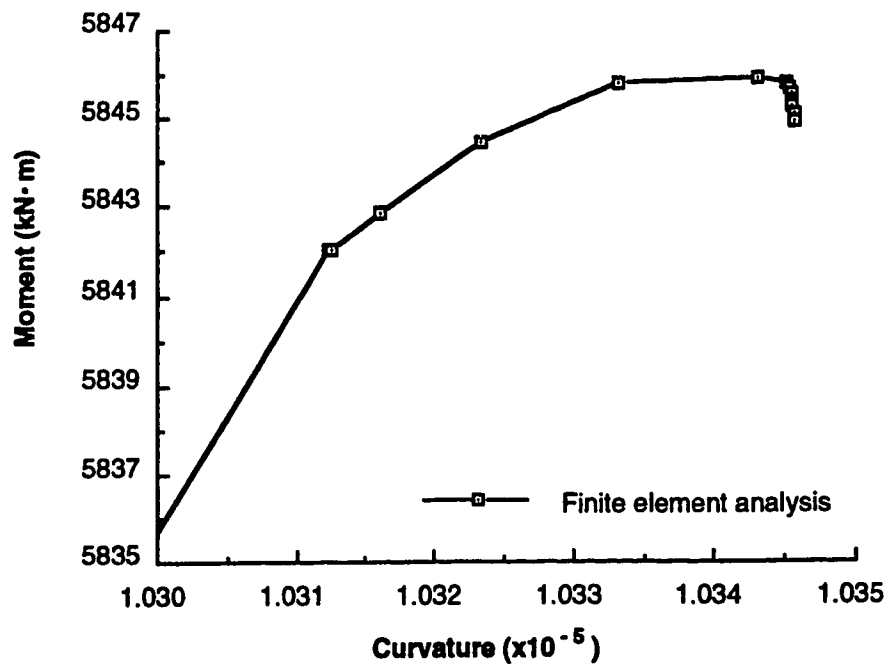


Figure 5.20 Moment versus displacement response of S23

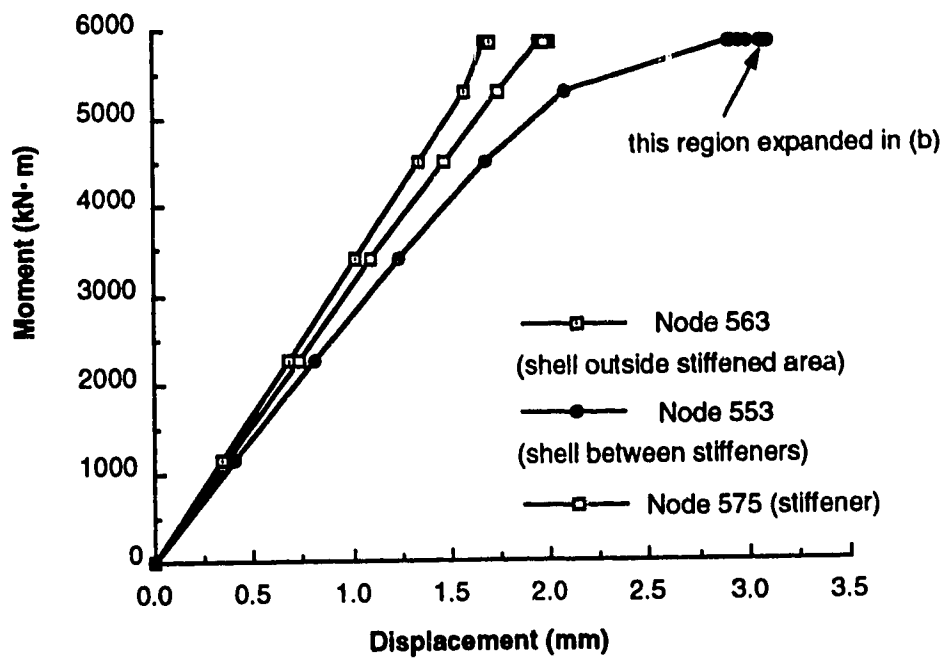


(a) Full range

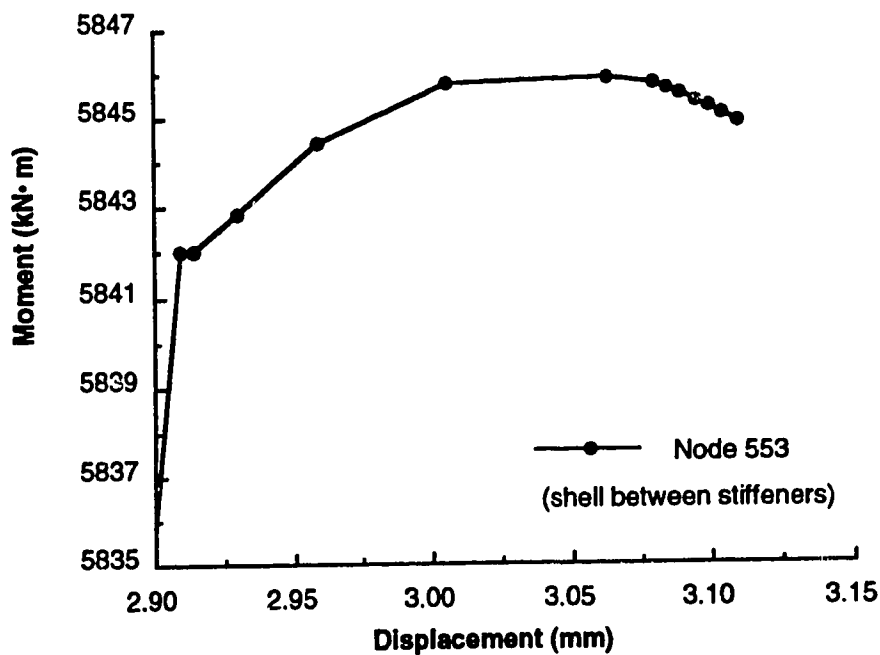


(b) Near the ultimate point

Figure 5.21 Moment versus curvature response of S24



(a) Full range



(b) Near the ultimate point

Figure 5.22 Moment versus displacement response of S24

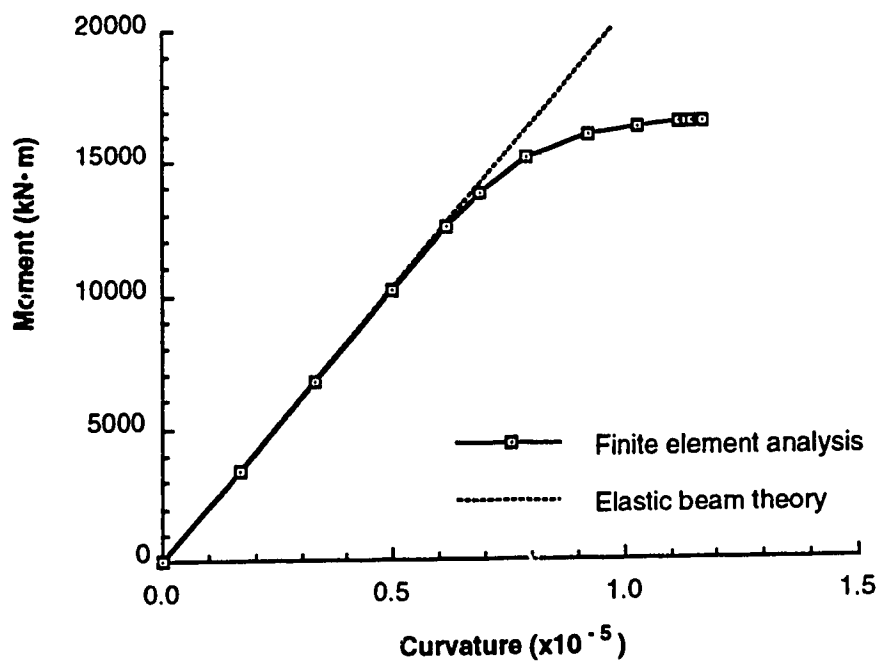


Figure 5.23 Moment versus curvature response of S31

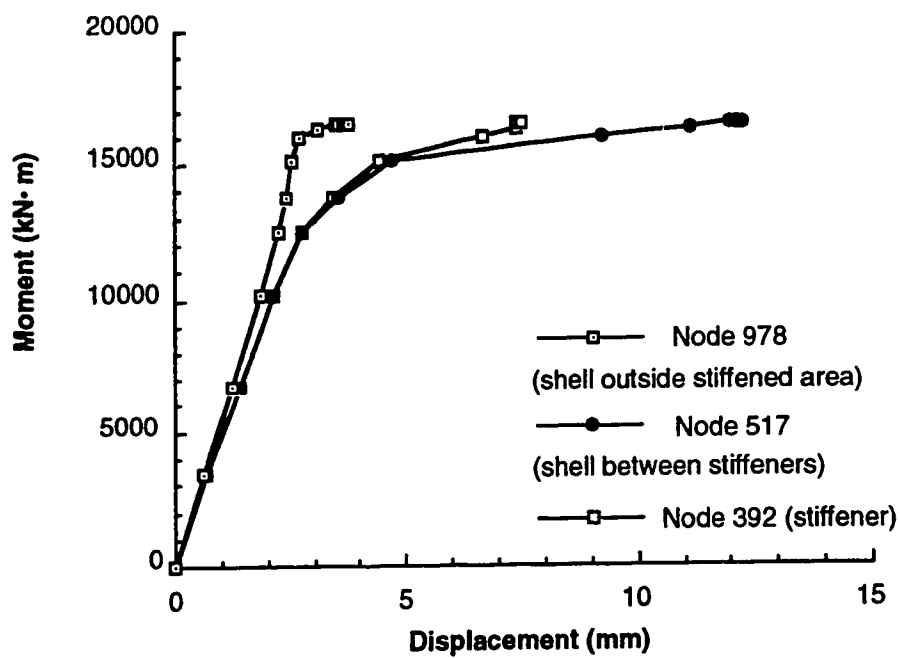
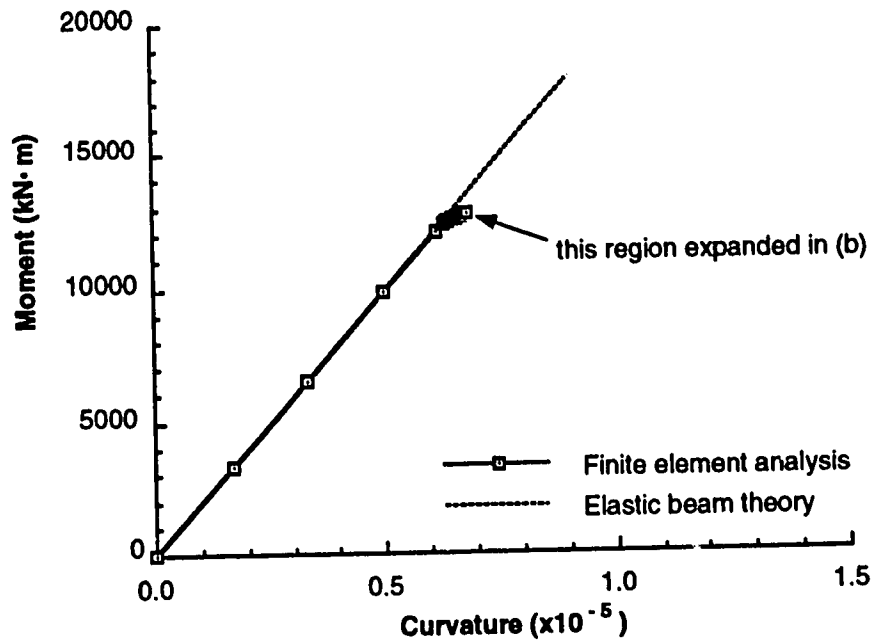
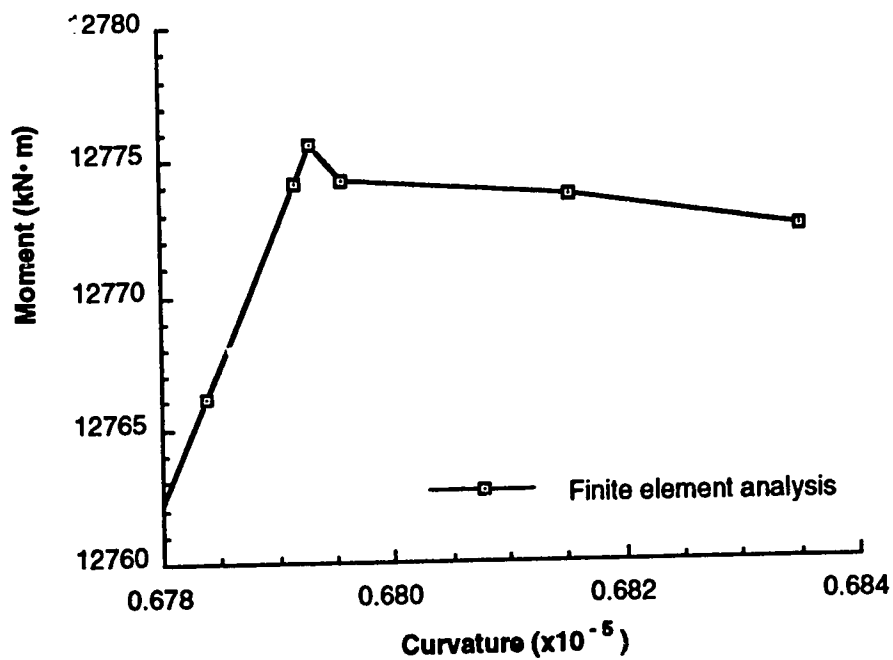


Figure 5.24 Moment versus displacement response of S31



(a) Full range



(b) Near the ultimate point

Figure 5.25 Moment versus curvature response of S33

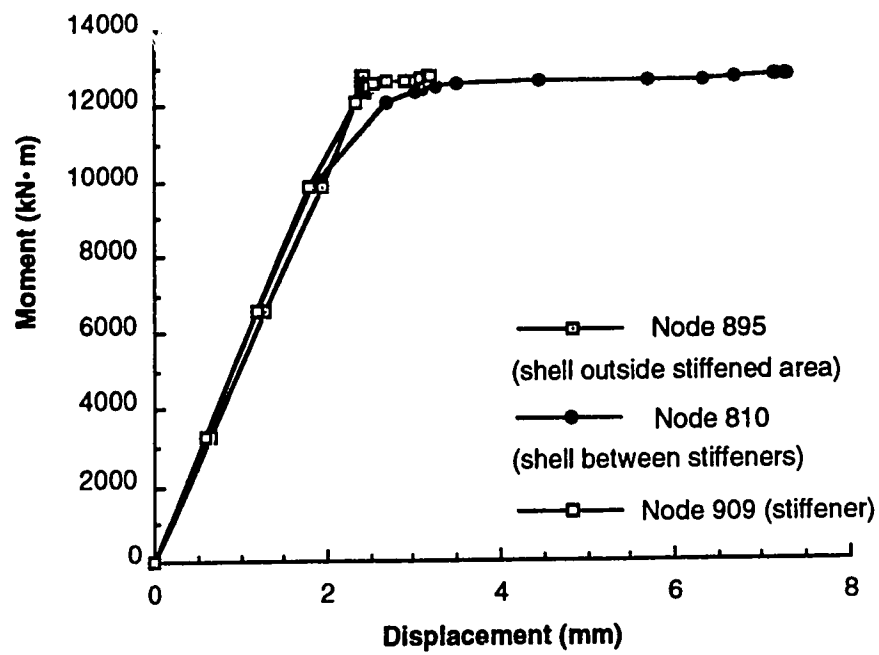


Figure 5.26 Moment versus displacement response of S33

CHAPTER SIX

DESIGN FOR BENDING CAPACITY**6.1 General**

Current design procedures for longitudinally stiffened cylinders subjected to bending significantly underestimate the load-carrying capacity, as will be shown later by comparison with the test and finite element results. The prime reason for the conservatism is the lack of experimental data. Consequently, the available analytical models cannot be verified by physical tests. Design codes conservatively apply the rules for stiffened cylinders under axial compression to their flexural counterparts. This is based upon the similarity of unstiffened cylinders loaded in bending or in compression. In addition to being conservative, the complexity of the current procedures for the general instability case is not especially suitable for design purposes. Moreover, a designer may also find that the allowable stress method used in current design guidelines for shell structures is not compatible with the limit state design approach that is now generally accepted in structural design.

Following an evaluation of existing design provisions, the experimental and numerical results reported in the preceding chapters are used to examine the effect of the parameters on the failure mode and load-carrying capacity. On the basis of the parametric study, a set of design equations for the flexural strength of longitudinally stiffened cylinders is proposed and a procedure is recommended for the design of the longitudinal stiffeners themselves. The proposed design equations define the bending capacity corresponding to different failure modes. The issue of multimode interaction is also discussed in this chapter since it is an important concern in current design standards.

6.2 Evaluation of Existing Design Provisions

Most of the current design criteria for longitudinally stiffened steel cylinders subjected to bending are found in offshore structural design codes, and they were reviewed in detail in Chapter Two. The provisions in API (1987), ASME (1986) and ECCS (1988) guidelines are very similar, except for some minor differences in calculating the knockdown factors. All of them use the same equation as the standard approach for general

buckling. Additionally, the formula for unstiffened shell buckling is modified in a similar manner to analyze shell buckling between stiffeners. Other design standards, such as those of DNV (1987) and CSA (1992), are even more conservative. The comparison made in Chapter Two using test SB1 (Bailey and Kulak 1984) shows that a high degree of conservatism is present in all codes for the capacity prediction based on general instability failure.

The API guideline (API 1987) is chosen here to compare the experimental and numerical results of this study. Tests SB2 and SB3a, which buckled outside the stiffened area, are not included in this comparison. The rules given by API are only applicable to cylinders with stiffeners covering the whole circumference, and thus shell buckling outside the stiffened area is not considered.

The results of the comparison are presented in Table 6.1. For the ten cylinders that failed in general buckling, the API guideline gives a capacity that is between 18% and 55% below the experimental and numerical results. For the case of shell buckling between the stiffeners, the estimated capacity is 10 to 20% less than that predicted using the finite element study. On average, the discrepancy is -29% for general buckling and -16% for shell buckling. (It should be mentioned that the safety factor specified in the API guideline has not been applied in the calculation of $M_{u \text{ API}}$ in Table 6.1, which is the moment capacity given by API.)

In computing the quantity $M_{u \text{ API}}$, it was assumed that the stiffeners uniformly cover the whole circumference. Of course, for the cylinders studied herein, only part of the compression zone was stiffened. The assumption was made because the design guidelines cited make no provision for cylinders with only part of circumference longitudinally stiffened. Such an assumption generally results in an increase in $M_{u \text{ API}}$ and thus lessens the difference when compared to the test and numerical results.

All of the current design procedures first provide an estimate of the shell buckling stress and then use this stress to predict the failure moments. A large portion of the discrepancy between the predicted moments and the results generated herein arises from the process of converting the shell buckling stress into a bending moment.

First, the moment is calculated according to the linear beam theory

$$M_u = \sigma_u \pi R^2 t_e \quad (6.1)$$

in which $(\pi R^2 t_e)$ is the elastic section modulus (S) and t_e is an equivalent thickness of a stiffened shell. Since it is required by the design specifications that $\sigma_u \leq \sigma_y$, M_u can never exceed the yield moment, which is usually more than 20% lower than the plastic moment for a stiffened cylinder of large diameter. Equation 6.1 assumes an elastic failure and defines the failure as the moment at initiation of buckling. However, a stiffened cylinder in bending behaves in a different way when it fails by general buckling. As was observed in both the experimental and numerical studies, ultimate failure in bending usually takes place well after the initiation of general buckling. This is in contrast to the case of axial compression. In the case of bending, stress redistribution allows the moment to continue to increase after yield and initial buckling. Inelasticity is adequately developed over the cross-section for a typical general buckling case, and the ultimate moment can be more than 90% of the fully plastic moment.

Secondly, the equivalent shell thickness t_e in Equation 6.1 is defined by the codes as

$$t_e = \frac{A_s + s_e t}{s} \quad (s_e \leq s) \quad (6.2)$$

where A_s is the cross-sectional area of a stiffener, s is the stiffener spacing, and s_e is an effective stiffener spacing, which takes the reduced stiffness of buckled shell into account. Equations 6.1 and 6.2 imply that s be reduced to s_e throughout the circumference. Such an approach is appropriate for the case of uniform axial compression, in which the shell may buckle all over the circumference. When subjected to bending, however, shell buckling only occurs at the location of maximum compressive stress: most of the cross-section remains fully effective. Because of an inadequate research base for stiffened cylinders in bending, design codes conservatively reduce s in the same manner for both axial compression and bending.

The above comparison is also shown graphically in Figure 6.1, in which the horizontal axis refers to the row number of Table 6.1. It is apparent that the bending capacity is significantly underestimated by the current design methods, especially for cylinders that fail by general buckling.

6.3 Parametric Study

The purpose of the parametric study is to identify the effect of key parameters on the failure mode and the bending capacity. Based on this examination, bending behavior of stiffened cylinders can be predicted and design approaches can be developed.

The database of the parametric analysis comprises the results of the experimental study in Chapter Three and the finite element analyses in Chapter Five. These cylinders, especially those of the finite element analyses, provide a selection of various parameters covering a broad range of practical values.

6.3.1 Shell Buckling outside the Stiffened Area

Since only part of the circumference in the compression zone, designated by the angle Φ , is longitudinally stiffened, the shell outside the stiffened area may buckle under compression. Experimental observations indicate that such buckling is typically an abrupt failure. The ultimate moment is reached immediately following the shell buckling, with little subsequent increase of load and deformation.

In the physical tests, two specimens, SB2 and SB3a, failed by shell buckling outside the stiffened area. Other cylinders of both the experimental and numerical study exhibited the failure in the stiffened area. It is apparent that the type of failure, whether it is inside or outside the stiffened area, is primarily dependent on Φ and R/t . Other parameters affecting the failure mode include the ratio of stiffener spacing to shell thickness, s/t , and the compressive residual stress outside the stiffened area, σ_{rc2} . The s/t ratio controls the capacity of the stiffened panel. When this capacity is high because of a small s/t value, the failure is more likely to occur in the shell outside the stiffened area, and vice versa. A high level of σ_{rc2} will promote shell buckling outside the stiffened area. The influence of s/t and σ_{rc2} can be taken into account by modifying Φ as

$$\Phi_1 = 0.35 \frac{\sigma_y}{\sigma_{rc1}} \Phi \quad (6.3)$$

where σ_{rc1} is the compressive residual stress in the shell between the stiffeners and 0.35 is the σ_{rc1}/σ_y ratio measured from the 5 mm thick test specimen, SB2. The σ_{rc1}/σ_y ratio is

chosen for use in Equation 6.3 because it reflects both s/t and σ_{rc2} . The dependence of σ_{rc1} on s in a 5 mm thick cylinder can be found in Equation 5.1. The residual stresses σ_{rc1} and σ_{rc2} are indirectly related because both are dependent upon the shell thickness in the same manner, and they act together to balance the tensile residual stress. Therefore, Φ_1 is a modification of the angle Φ that reflects the influence of other parameters such as s/t and σ_{rc2} .

The properties of all the cylinders investigated in this study are plotted in Figure 6.2 in terms of the radius to thickness ratio (R/t) and the equivalent angle (Φ_1). A boundary is drawn by judgement between the two failure patterns by a solid line, and the upper and lower bounds of the failure region limits are represented by dashed lines. For a cylinder of given R/t , the Φ_1 value determines where buckling will occur. The cylinders to the left side of the line failed by the shell buckling outside the stiffened area, while those on the right side had a failure in the stiffened area. The limit lines pass close to SB3a and S32 because the deformed shapes (Figures 4.13 and 5.12) showed that the two failure modes were nearly concurrent in these two cylinders. Buckles appeared both inside and outside the stiffened area in these cases. Figure 6.2 shows that the angle Φ_1 mainly controls the failure pattern with given residual stress distribution and stiffener arrangement (spacing and stiffness of stiffeners). The failure mode is also affected by the R/t ratio: the required Φ_1 increases for large R/t values if a failure in the stiffened area is desired. This is due to the fact that a larger R/t ratio results in a more uniform distribution of compressive stress, which in turn promotes local shell buckling outside the stiffened area. In Figures 5.4 and 5.12, the deformed shape of S32 (R/t ratio of 360) shows larger buckles outside the stiffened area relative to those of S12, which is identical to S32 except the latter has a small R/t ratio of 120.

The spacing to thickness ratio (s/t) also explicitly affects the failure mode, as observed in Figure 6.3. Of the four finite element models in each R/t group, the ones with the smallest values of s/t and Φ , S32, S22 and S12, are the closest in the group to the boundary. This is because when the stiffened area is strengthened by a small s/t , it is possible that the failure will be shifted to the shell outside the stiffened area. Cylinders that are heavily stiffened over a small angle Φ are the most likely to fail in shell buckling outside the stiffened area. Test specimen SB2 ($s/t = 38.1$, $\Phi = 32^\circ$) is a typical example.

It is also observed from the case of test SB3a that a high level of compressive residual stress in the shell outside the stiffened area (σ_{rc2}) increases the possibility of shell buckling in that region. Specimen SB3a failed in shell buckling outside the stiffened area

because of the high welding residual stresses in the 3 mm thick shell, even though the stiffened angle was large (63.5°).

Once it is established that shell buckling will occur outside the stiffened area, its capacity is reflected by a number of parameters. A small angle Φ or a large R/t ratio will result in a relatively uniform distribution of compressive stress, which promotes shell buckling and lowers the ultimate moment. The level of residual stress also influences the capacity. However, the arrangement of stiffeners (spacing and stiffness) is not very influential when shell buckling takes place outside the stiffened area. Previous research on unstiffened tubes, such as the design formulas proposed by Stephens *et al.* (1982), can be employed to predict the buckling strength in the shell outside the stiffened area.

6.3.2 Failure in the Stiffened Area

When buckling took place within the stiffened area, two types of failure were observed during the experiments and the finite element analyses. These were general buckling and shell buckling failures. The sixteen cylinders in this category are plotted in terms of the stiffener spacing to shell thickness ratio, s/t , and the radius to thickness ratio, R/t , in Figure 6.3. The general buckling and shell buckling modes divide Figure 6.3 into two zones. Some of the cylinders in the general buckling zone are overlapped because they have identical values of s/t and R/t . For example, S21, S22, and S25 are shown by the same data point because they all have $s/t = 54$ and $R/t = 240$. They are different in other ways, however. For example, both the angle (Φ) and the size of stiffeners vary.

The straight line in Figure 6.3 separates the two buckling modes in an approximate way. The key parameter that distinguishes the buckling modes is the spacing ratio s/t . Whether general buckling or shell buckling will occur in this region depends largely on the value of this ratio. However, the R/t ratio indirectly influences such a dependence. As R/t becomes large, the dividing line in Figure 6.3 moves towards small s/t values. It indicates that a close stiffener spacing is required for a cylinder with a large R/t ratio if general buckling is to be guaranteed.

The s/t ratio also affects the bending capacity, expressed by the moment ratio M_u/M_p , the moment at failure non-dimensionalized using the plastic moment. Figures 6.4 and 6.5 display the reduction of the moment ratio as the s/t ratio increases. A large s/t ratio

may not only reduce the general buckling capacity, but also change the failure mode into shell buckling, which usually has a lower capacity than that of the general buckling.

Figure 6.6 demonstrates the effect of R/t on the capacity. The common logarithm of the R/t ratio ($\log_{10}(R/t)$) was found to be the best descriptor for such an effect. As shown in the figure, the decrease in the moment ratio is linearly proportional to the increase in $\log_{10}(R/t)$. The slope of these straight lines is a function of the s/t ratio. The twelve cylinders in Figure 6.6 (cylinders S11 and S12 are coincident because they have identical R/t and M_u/M_p ratios) are all the results of the finite element analysis. Despite the fact that different buckling modes, general buckling or shell buckling, exist among these cylinders, the linear curves seem to be applicable for both modes.

To identify the influence of the angle Φ , cylinders identical in other aspects but with different Φ -values are compared in Figure 6.7 in three R/t groups. It is evident that the ultimate moment ratio (M_u/M_p) is practically independent of Φ as long as the failure is clearly in the stiffened area. For cylinders with different Φ angles, the moment ratio remains almost the same. The decline of M_u for a small Φ is offset by a reduction of the plastic section modulus used to calculate M_p .

Another parameter that affects the bending capacity is the stiffness of the stiffeners themselves. This can be observed by comparing cylinders S22 and S25. The only difference between the two is the size of the HSS stiffeners (50.8 x 25.4 x 3.18 for S22 and 25.4 x 25.4 x 2.54 for S25), which resulted in $M_u/M_p = 0.79$ for S22 and $M_u/M_p = 0.70$ for S25. It is apparent that the St. Venant's torsional constant, J_s , is an influential factor. Since the shell buckling waves cause the stiffeners to twist, the development of shell instability relies on the torsional resistance of the stiffeners.

6.4 Interaction of Buckling Modes in Stiffened Cylinders

Structures with multiple buckling modes, for instance built-up or fabricated structures containing plate or shell elements, exhibit different buckling behavior that depends primarily on the geometry. In such structures, interaction of buckling modes may be present when the buckling loads are nearly simultaneous. The following discussion is directed to the interaction between general buckling and shell buckling in the stiffened area, which is the most significant type of mode interaction in a stiffened cylinder. The purpose of the discussion is to develop a suitable design approach based on the results of large-

scale experiments or their numerical simulation. This design approach is expected to be more efficient and accurate than the current design approach, which is based on the classic buckling analysis.

6.4.1 Classical Buckling Analysis

Conventionally, the critical load of a perfect system, λ_c , is the lowest eigenvalue associated with an eigenvector \mathbf{u} which describes the displacement field of the corresponding buckling mode. Based on this solution, the postbuckling behavior and the imperfection sensitivity of an imperfect system can be found by the technique of initial post-buckling analysis (Hutchinson and Koiter 1970). For a structure with multiple buckling modes, the classical buckling analysis produces the buckling load (λ_i) of each mode (\mathbf{u}_i) individually. The mode with the lowest buckling load is considered to be the failure mode and the related load is the critical load. In such an analysis, different analytical models and displacement fields are used for different buckling modes. Each model involves only one buckling mode and the displacement field of other modes and their interaction are excluded. Taking the example of a stiffened shell, the orthotropic shell model is used for general buckling, and the curved panel model is used for shell buckling.

Figure 6.8 shows the buckling load of a structure with two buckling modes: Mode I and Mode II. The load-carrying capacity is represented by load factor λ , and the geometry of the structure is described by parameter α . The capacity versus geometry characteristics of these two modes I and II are similar to that of the general buckling mode and shell buckling mode, respectively. The capacity curves of the two modes intersect at B, where the buckling modes are simultaneous ($\lambda_I = \lambda_{II}$). For the geometry parameter $\alpha \leq \alpha_B$, the structure fails in Mode I; and when $\alpha > \alpha_B$, Mode II becomes the dominant mode. As the geometry varies, the failure mode changes from one to the other. The curve ABC is the design curve given by the classical buckling analysis, which includes the effect of imperfections. It is noted that there is a discontinuity of slope at the junction of the two curves, point B. This is due to the inconsistency of the analytical method, which uses two totally different models in the vicinity of B. As a result, a sudden change of the failure mode occurs at B, even though the variation of geometry is smoothly continuous.

6.4.2 Mode Interaction

The interaction of buckling modes was first investigated in detail by van der Neut (1968) for built-up columns. Byskov and Hutchinson (1977), and Hui *et al.* (1981) studied the mode interaction in longitudinally stiffened cylinders under axial compression. The analytical method employed in these investigations was similar to that for the initial postbuckling of single mode buckling, except that an interactive displacement field

$$\mathbf{u} = \lambda \mathbf{u}_0 + \xi_i \mathbf{u}_i + \xi_i \xi_j \mathbf{u}_{ij} \quad (i, j = 1, 2, \dots, m) \quad (6.4)$$

is assumed in order to include the nonlinear interaction (Budiansky 1974, Koiter 1976). The indices i and j refer to different buckling modes, and the summation convention of tensors is applicable. The other notation in Equation 6.4 is:

- λ = load factor;
- \mathbf{u}_0 = pre-buckling displacement;
- ξ_i = amplitude of mode i ;
- \mathbf{u}_i = the i th buckling mode;
- \mathbf{u}_{ij} = the secondary-order displacement. When $i \neq j$, it represents the mixed displacement field of modes i and j .

The displacement \mathbf{u} in Equation 6.4 can be used for a structure in which the m buckling modes are simultaneous or nearly simultaneous.

The results of these studies indicated the imperfection sensitivity observed in multimode analysis is much higher than that of classical buckling analysis (single mode analysis) if the buckling modes are nearly simultaneous. The effect of imperfections on multimode interaction is represented by a dashed curve EF in Figure 6.8, which is significantly different from the single mode curve (EBF) in the transition zone. The design curve given by classical buckling analysis, the curve ABC in Figure 6.8, can substantially overestimate the capacity for structures with nearly simultaneous buckling modes. Obviously, a curve like EF should be used for the transition between the two buckling modes.

Needless to say, the assumed displacement field in Equation 6.4 is an approximation, especially when it is applied to stiffened shells. For a cylinder with nearly simultaneous buckling modes of general buckling and shell buckling, the spacing between the stiffeners is of intermediate magnitude, and a model such as a shell panel with discrete stiffeners would be reasonable. This type of analytical model is not available to date, however. The displacement components in Equation 6.4 are either of an orthotropic shell with “smeared-out” stiffeners (for the displacement of general buckling) or of a shell panel (for the displacement of local shell buckling). The former is valid only for closely spaced stiffeners (Walker and Sridharan 1980), and the latter does not include the stiffeners. It is not clear how accurately such a mixed displacement field can represent the deformation of interactive buckling.

Like any other analytical model in shell theory, the multimode analysis for stiffened shells is only available for elastic buckling. Because of the presence of compressive welding residual stresses, stiffened steel cylinders usually fail in the inelastic range, however. Moreover, the inelastic buckling deformation at the ultimate point is so large that the initial postbuckling analysis may bring in errors that are no longer negligible. Because of these limitations, the imperfection sensitivity arising from mode interaction remains uncertain for fabricated large diameter steel cylinders.

6.4.3 Design Considerations

Although calibrated with test results using knockdown factors α and η (Equation 2.2), current design formulae are mainly based on classical buckling theory. Each buckling mode is analyzed individually and the mode interaction is disregarded in the analysis. Because of the uncertainty of the capacity in the transition zone, the guidelines (API 1987, ASME 1986) opt to separate the buckling modes and avoid the issue of simultaneous buckling. Both codes choose shell buckling as the control mode and require that the general buckling load be at least 20% higher than the shell buckling load.

Since shell buckling (Mode II in Figure 6.8) is the only failure mode allowed, the use of other failure modes (e.g. general buckling or Mode I in Figure 6.8) is excluded from design. As shown in Figure 6.8, only $\alpha \geq \alpha_F$ can be used and the range with higher capacity ($\alpha < \alpha_F$) is abandoned in design. Additionally, since the general buckling load is

largely underestimated (Section 6.2), the required stiffener spacing and size for the 20% margin may be excessively conservative.

It is apparent from the above discussion that the “high imperfection sensitivity” of interactive buckling (Byskov and Hutchinson 1977) refers to the comparison with classical buckling analysis, which selects a single buckling mode and ignores the effect of other buckling modes. In reality, however, the behavior of shell buckling and general buckling are always interactive: stiffeners deform with shell buckling and vice versa. As can be seen from the deformed shapes of test specimens and the finite element analyses, other buckling modes participate in the deformation of the governing mode. For the large-scale experiment and its numerical simulation, the results are the response of the structures under real imperfections and residual stresses. This is because no restrictions are imposed on the displacements: the models are inclusive for all buckling modes and their nonlinear interaction. Therefore, for a design curve based on these results, there is no need to exclude simultaneous buckling or to lower the capacity for it.

Figure 6.6 shows the numerical results of cylinders that failed in the stiffened area. The six cylinders with the s/t ratio of 54 failed by general buckling whereas the three with $s/t = 108$ failed by shell buckling. Of the other three cylinders, with $s/t = 81$, the one with $R/t = 120$ showed a general buckling failure and the other two failed by shell buckling. It appears that the linear relationship between the moment ratio, M_u/M_p , and $\log_{10}(R/t)$ is representative of both failure modes. In spite of their different failure modes, the three cylinders of $s/t = 81$ are nearly on the same line which lies intermediate between the lines for $s/t = 54$ and $s/t = 108$. There is no sign that the capacity of a cylinder with simultaneous buckling failure needs to be uniquely described. Instead, with the continuous variation of the geometry, the failure mode seems to transit smoothly from a typical general buckling to a typical shell buckling. Hence, a design curve based on test and nonlinear shell element analysis should be capable of predicting the two failure modes and their transition universally.

6.5 Capacity for the Case of Shell Buckling Outside the Stiffened Area

Using the parametric analysis of the experimental and numerical results, design equations for the bending capacity can now be developed in terms of the two different failure patterns—shell buckling outside the stiffened area and the failure inside the stiffened area.

As was discussed in Section 6.3.1, the parameters that affect shell buckling outside the stiffened area are the R/t ratio and the angle Φ that describes the stiffened portion of the shell. The capacity decreases for large R/t ratios and small Φ angles. In addition, the presence of compressive residual stresses must be considered.

A practical way to establish the bending capacity for this type of failure is to employ the formulas for the buckling of unstiffened cylindrical shells, and then modify them for stiffened shells. The differences that should be accounted for include the gradient of bending stress and the compressive residual stress. The stress gradient in the shell outside the stiffened area is more substantial than that near the apex of an unstiffened cylinder. This stress gradient becomes steep as the angle Φ increases. In addition, the level of residual stresses in longitudinally stiffened cylinders is much higher than it is in unstiffened tubes.

In order to develop a simple procedure which is suitable for design use, the following assumptions are employed.

- (1) The stress in the shell can be approximately calculated using elastic beam theory as

$$\sigma = \frac{M (R \cos\theta - z_0)}{I_y} \quad (6.5)$$

in which I_y is the moment of inertia of the cross-section, including the stiffeners, z_0 is the z coordinate of the neutral axis relative to the center of the cylinder, and θ is the angle between the apex and the location where stress is calculated.

- (2) The buckling stress is calculated at $\theta = \Phi/2$. This is the location of the stiffeners furthest away from the apex, where the compressive stress is the highest in the shell outside the stiffened area.
- (3) The effect of stiffener arrangement (spacing and stiffness) has a negligible effect on the ultimate stress of the shell buckling outside the stiffened area.

The first assumption is an attempt to make the procedure more appealing for practical design since a one-dimensional beam stress analysis will replace three-dimensional shell stress analysis. The use of the elastic sectional properties, I_y and z_0 , in

Equation 6.5 is based on the observation that, for large diameter steel cylinders, shell buckling usually occurs before plasticity is well developed. Most of the cross-section remains in the elastic stage of deformation.

Conventionally, the critical stress of a panel (flat or curved) with non-uniform stress distribution refers to the maximum compressive stress. Thus, the second assumption uses the highest compressive stress in the shell outside the stiffened area, which is about the same as that at $\theta = \Phi/2$, to establish the buckling strength of the shell.

The spacing and the size of the stiffeners influence where the failure will take place—inside or outside the stiffened area. Nevertheless, their significance on the shell buckling stress in the region outside the stiffened portion is far less than other parameters, as was stated in the third assumption. The direct contribution of the stiffener arrangement to the bending strength is reflected in the calculation of the cross-sectional properties such as I_y and z_0 .

There are a number of formulas available for the calculation of the critical stress of unstiffened cylinders. Stephens *et al.* (1982) recommended a set of equations that were based on about 35 axial compression tests, including five large R/t specimens of their own experiments. These equations were also found satisfactory in predicting the bending test results of large diameter unstiffened tubes reported by Stephens *et al.* (1982) and by Bailey and Kulak (1984).

For the material and the R/t range of the cylinders in this study, the equation given by Stephens *et al.* is

$$\frac{\sigma_1}{\sigma_y} = 1.625 + 0.489 \log_{10}(\gamma_s) \quad (6.6)$$

in which σ_1 is the ultimate stress at the extreme compression region of an unstiffened shell, and γ_s is a coefficient defined as

$$\gamma_s = \left(\frac{E}{\sigma_y} \right)^{1/2} \left(\frac{t}{R} \right)^{3/2} \quad (6.7)$$

To apply Equation 6.6 to the shell outside the stiffened area, the presence of compressive residual stresses must be taken into consideration. Yield will initiate at the stress of

$$\sigma_{y2} = \sigma_y - \sigma_{rc2} \quad (6.8)$$

in which σ_{rc2} is the compressive residual stress in the shell outside the stiffened area. In the following derivation, σ_{y2} will be used to replace σ_y in Equations 6.6 and 6.7.

In an unstiffened cylinder, shell buckling under bending occurs at the apex. In a large diameter tube, the stress will be nearly uniform in this region. However, outside the stiffened area of a stiffened cylinder of usual proportions, there is a significant stress gradient in the shell. The favorable effect of the nonuniform stress can be taken into account by modifying the buckling stress σ_1 of Equation 6.6 such that

$$\sigma_u = \sigma_1 \frac{1 + \chi \Phi}{\cos(\Phi/2)} \quad (6.9)$$

in which σ_u is the ultimate stress for shell buckling outside the stiffened area and χ is a linear expression of R/t

$$\chi = 0.10 + 0.0024 R/t \quad (6.10)$$

The constants 0.10 and 0.0024 have been chosen from an analysis of the experimental and numerical results.

The term $(1 + \chi \Phi)/\cos(\Phi/2)$ reflects the difference between the ultimate stress of a stiffened shell, σ_u , and that of an unstiffened shell σ_1 . When $\Phi = 0^\circ$, which is the case of an unstiffened shell, $1 + \chi \Phi/\cos(\Phi/2) = 1$ and $\sigma_u = \sigma_1$, as would be expected. For $\Phi = 180^\circ$, or when half of the circumference is stiffened, $1 + \chi \Phi/\cos(\Phi/2) = \infty$ and $\sigma_u = \infty$. This indicates that this type of failure cannot happen since all of the compression zone is longitudinally stiffened. The failure can only be inside the stiffened area. Thus, Equation 6.9 at least meets the logical boundary conditions of the member capacity.

In summary, the proposed procedure for calculating the ultimate capacity of shell buckling outside the stiffened area is as follows:

- (1) Obtain σ_1 for the unstiffened cylinder from

$$\frac{\sigma_1}{\sigma_{y2}} = 1.625 + 0.489 \log_{10}(\gamma_s) \quad (6.6)$$

where γ_s and σ_{y2} are defined as

$$\gamma_s = \left(\frac{E}{\sigma_{y2}} \right)^{1/2} \left(\frac{t}{R} \right)^{3/2} \quad (6.7)$$

$$\sigma_{y2} = \sigma_y - \sigma_r c^2 \quad (6.8)$$

(2) Calculate σ_u for the outside shell of a stiffened cylinder,

$$\sigma_u = \sigma_1 \frac{1 + \chi \Phi}{\cos(\Phi/2)} \quad (6.9)$$

$$\text{where} \quad \chi = 0.10 + 0.0024 R/t \quad (6.10)$$

(3) Finally, calculate the ultimate moment as

$$M_u = \frac{\sigma_u I_y}{R \cos(\Phi/2) - z_0} \quad (6.5b)$$

The procedure described above was applied to the two test specimens that failed in this buckling mode, SB2 and SB3a. The predicted ultimate moment for SB2 is 1907 kN·m, which is 2% lower than the experimental result of 1947 kN·m. The predicted value of 1198 kN·m for SB3a is 5.3% higher than that measured in the test (1138 kN·m).

Although more than one failure mode exists, the structure will always fail in the mode corresponding to the lowest failure load. This requires that a design approach for one failure mode should not only accurately predict the failure of that mode, but also produce ultimate loads higher than the actual values when failure is in the other mode. Thus, when the equations for shell buckling outside the stiffened area are applied to the cylinders which failed inside the stiffened area, the predicted ultimate moments should be higher than the actual failure loads.

This requirement was found satisfactory when Equations 6.5 to 6.10 were applied to the sixteen cylinders that failed in the stiffened area. The results show that the shell buckling capacity outside the stiffened area varies from 102% (S32) to 202% (S33) of the inside failure capacity. This is also consistent with the behavior observed in Figure 6.2. For example, S32 is close to the boundary between inside and outside failure because its capacities for the two failure modes are nearly the same, and S33 is far away from that

boundary because its general buckling capacity is much lower than that of shell buckling outside the stiffened area.

6.6 Capacity for the Case of Failure in the Stiffened Area

Although the buckling strength of unstiffened shells is usually given by empirical formulas calibrated with experiments, almost all existing design approaches for general buckling of stiffened cylinders use mechanical models, based on either an orthotropic shell theory or a column-plate model. Mechanical models are helpful for understanding the failure mechanism, but they also have some common deficiencies.

First, complexity can hardly be avoided, especially when both shell curvature and inelasticity are to be included. Commonly, the “effective width” of shells between stiffeners and the numbers of buckling waves are computed iteratively. Secondly, when applied to design for bending, a mechanical model usually gives the ultimate stress. This stress is converted into the ultimate moment using linear beam theory. The result of such a conversion is too conservative for general buckling failure, in which the plasticity may be developed over much of the cross-section.

As an alternative, an empirical formula based on the test and finite element results, such as the one proposed following, is in a simple form suitable for design use. It calculates the ultimate moment directly, and is thereby compatible with limit states design.

As mentioned in Section 6.3.2, two buckling modes, general buckling and shell buckling between stiffeners, are possible when failure is inside the stiffened area. Nevertheless, the previous discussion of interactive buckling concluded that the transition between the two modes is smooth. The high imperfection sensitivity in the region of interactive buckling refers to classical buckling analysis, but does not apply to the results of physical test or its numerical simulation. Furthermore, as shown in Figure 6.6, linear curves seem to be capable of representing cylinders that failed in both modes. Therefore, it is possible that the capacity of the two buckling modes can be described by a unified equation.

The bending capacity when failure takes place inside the stiffened area is reflected by several key parameters. As revealed by the parametric study, these key parameters include the R/t and s/t ratios and the stiffness of the stiffeners.

The twelve cylinders shown in Figure 6.6 have the same stiffeners and shell thickness. Differences in their capacity ratio, M_u/M_p , can be attributed to the variation in the R/t and s/t ratios. The figure shows that M_u/M_p can be expressed in terms of $\log_{10}(R/t)$ by a family of straight lines. These lines appear to have a common intersection and their slopes are dependent on s/t . Such a family of curves is found to be

$$M_{u \text{ prd}}^*/M_p = 0.527 \{2.30 - (\log_{10}(s/t) - 0.963) (\log_{10}(R/t) - 1.32)\} \quad (6.11)$$

in which $M_{u \text{ prd}}^*$ denotes the predicted ultimate moment for 5 mm thick cylinders with HSS 50.8 x 25.4 x 3.18 stiffeners. Figure 6.9 shows that Equation 6.11 provides a reasonable representation of the results obtained in the finite element analyses. However, so far the examination includes only the effects of R/t and s/t , and does not account for the influence of different stiffeners.

The geometric parameters of the HSS stiffeners, such as area (A_s), moment of inertia (I_s), and St. Venant torsional stiffness (J_s), were examined. It was found that the St. Venant torsional stiffness provides the best description of the influence of the stiffeners. Figure 6.10 displays the effect of J_s/t^4 on the moment capacity. The test and finite element points are plotted for $M_u/M_{u \text{ prd}}^*$, in which the moment achieved in the physical tests or in the analyses, M_u , is divided by the moment predicted by Equation 6.10, $M_{u \text{ prd}}^*$. This ratio mainly reflects the effect of different stiffener size, since the effect of other parameters is already included in $M_{u \text{ prd}}^*$. The linear curve in Figure 6.10 is

$$M_u/M_{u \text{ prd}}^* = 0.881 + 0.704 \frac{J_s/t^4}{1000} \quad (6.12)$$

Combining Equations 6.11 and 6.12, the flexural capacity when failure takes place in the stiffened area is given by

$$M_{u \text{ prd}}/M_p = 0.371 \left(1.25 + \frac{J_s/t^4}{1000}\right) \{2.30 - (\log_{10}(s/t) - 0.963) (\log_{10}(R/t) - 1.32)\} \quad (6.13)$$

Equation 6.13 defines the ultimate moment in a simple manner. Only three parameters, the ratios R/t , s/t , and J_s/t^4 , are involved. This is a unified equation for the case of failure inside the stiffened area, whether it is by general buckling or by shell buckling.

The predictions of Equation 6.13 are compared with experimental and numerical results in Table 6.2. The mean value of the discrepancy is only -0.4% ; the highest one value is 5.6% , for SB1. The comparison is also shown graphically in Figure 6.11 where the row number of Table 6.2 is used as horizontal axis.

In order to ensure that Equation 6.13 interacts properly with the failure mode of shell buckling outside the stiffened area, test specimens SB2 and SB3a have been checked using Equation 6.13. The results show that the capacity inside the stiffened area is higher than that of shell buckling outside the stiffened area (33% higher in the case of SB2 and 16% higher for SB3a). This is consistent with the fact that these two cylinders failed by shell buckling outside the stiffened area during the physical tests.

6.7 Design Procedure for Longitudinal Stiffeners

It will be necessary in design to establish a stiffener size, spacing (s), and the total angle of the shell that will be stiffened (Φ) in accordance with the required bending capacity, M_u . As the first step, a designer will have to decide whether the failure criterion will be buckling inside or outside the stiffened area. A failure mode inside the stiffened area is recommended because it will have a relatively high M_u/M_p ratio for a given number of stiffeners. In addition to the high capacity, the case of general buckling inside the stiffened area has a ductile failure pattern. On the other hand, the failure outside the stiffened area is usually promoted by heavily stiffening within a small angle Φ .

The design procedures corresponding to the two fundamental failure modes are different since their ultimate moments are given by different equations, as presented in Sections 6.5 and 6.6. The key parameters of the modes are also different: the ultimate moment for failure inside the stiffened area relies on the s/t and J_s/t^4 ratios, while the flexural capacity is largely dependent on the stiffened angle Φ if the failure is outside the stiffened area.

The procedure for selecting the stiffener size, stiffener spacing (s) and the angle Φ for the two failure mode cases can be outlined as follows:

(a) Failure inside the stiffened area.

(1) As indicated in Figure 6.2, the Φ angle needs to be

$$\Phi_1 = 0.35 \frac{\sigma_y}{\sigma_{rc1}} \Phi > 46 + 0.046 R/t \quad (\text{degrees}) \quad (6.14a)$$

or

$$\Phi > (131 + 0.13 R/t) \frac{\sigma_{rc1}}{\sigma_y} \quad (\text{degrees}) \quad (6.14b)$$

so that the shell buckling outside the stiffened area will be excluded. The angle Φ may be increased for a higher flexural capacity.

- (2) The size of stiffeners can be chosen from the range of $J_s = 200t^4$ to $400t^4$ for closed-form thin-walled cross-sections, according to the tests and analysis in this study.
- (3) In order to determine the stiffener spacing s , the plastic moment capacity is estimated using

$$M_p = 1.1 \times 4 R^2 t \sigma_y \quad (6.15)$$

where $4R^2t\sigma_y$ is the plastic moment of the unstiffened cylinder. The coefficient 1.1 is used to account for the difference between stiffened and unstiffened cylinders, according to the cylinders involved in this study. By substituting M_p and the anticipated M_u into Equation 6.13, a preliminary value of s can be obtained. M_p must be recalculated afterwards so that a more accurate value of M_u can then be found using Equation 6.13.

(b) Failure outside the stiffened area.

The experimental and analytical results shown in Figure 6.2 indicate that shell buckling outside the stiffened area may take place when a small Φ angle is to be used, such as

$$\Phi_1 = 0.35 \frac{\sigma_y}{\sigma_{rc1}} \Phi < 26 + 0.074 R/t \quad (\text{degrees}) \quad (6.16a)$$

or

$$\Phi < (74 + 0.21 R/t) \frac{\sigma_{rc1}}{\sigma_y} \quad (\text{degrees}) \quad (6.16b)$$

The capacity for this case can be calculated by Equations 6.5 to 6.9.

Both failure modes must be checked when the angle Φ is between the values given by Equations 6.14 and 6.16. The lowest value of M_u is then taken as the bending capacity of the longitudinally stiffened cylinder.

If the value calculated for M_u is found unsatisfactory as compared with the capacity required, the designer can go back to step (a) or (b) and modify some of the selected parameters. For instance, the s/t ratio may be reduced for a higher failure capacity inside the stiffened area, and the Φ angle can be enlarged to raise the failure capacity outside the stiffened area. Since the capacity equations are simple and only a few parameters are involved, this procedure is easy for implementation.

6.8 Comparison with the Bending Strength of Unstiffened Cylinders

The experimental results of this study (Table 3.4) and the test of a stiffened cylinder by Bailey and Kulak (Section 2.1.1) can be compared with the results obtained by Stephens *et al.* (Table 2.3) for unstiffened cylinders. A remarkable increase of the ultimate flexural capacity, measured here by the moment ratio of M_u/M_p , is observed as a result of stiffening the cylinder longitudinally. For example, specimens B1, SB1, and SB2 have similar material properties and R/t ratios (130 ~ 150). However, the moment ratios for SB1 (general buckling) and SB2 (shell buckling) are 0.89 and 0.73, respectively, compared with a ratio of only 0.48 for the unstiffened specimen B1. Similarly, in the range of R/t close to 200, specimens SB3b and SB4 reached moment ratios of 0.87 and 0.94 (general buckling failures), respectively. These ratios are more than twice that of the unstiffened specimen B2, for which $M_u/M_p = 0.42$. Specimen SB3a has a moment ratio of 0.77, even though it failed by shell buckling.

The difference in capacity between longitudinally stiffened and unstiffened cylinders can be further developed by comparing the stiffened cylinders used in the numerical analysis and unstiffened cylinders that have the same material properties and R/t ratios. This comparison is shown in Table 6.3. In this table, the predicted ultimate moment, $M_{u\text{ prd}}$, of stiffened cylinders is calculated using the proposed design equation (Equation 6.13). For the unstiffened cylinders, the design equations proposed by Stephens *et al.* (Equations 6.6 and 6.7) are used to calculate $M_{u\text{ prd}}$. As expected, the predicted moments in Table 6.3 show that there is a significant difference between stiffened and

unstiffened cylinders. This difference is greater for stiffened cylinders with large R/t ratios or for those that failed by general buckling.

Figure 6.12 illustrates the $M_{u\text{ prd}}/M_p$ ratio of stiffened cylinders with $s/t = 50, 75, 100$, and 125 , compared with unstiffened cylinders. The material and the stiffeners are the same as those for the cylinders in the numerical analysis. The stiffened cylinders with $s/t = 125$ (shell buckling) have a $M_{u\text{ prd}}/M_p$ ratio between 0.45 to 0.81 as the R/t ratio varies from 400 to 100 . For stiffened cylinders that fail in general buckling ($s/t = 50$), the moment ratio is in the range of 0.71 to 0.95 . However, when the cylinders are unstiffened, the moment ratio is only 0.30 to 0.67 in the same R/t range. It is apparent that the use of longitudinal stiffeners results in a significant increase in bending strength, particularly for the case of general buckling. When the R/t ratio is large, such an increase becomes more substantial, as shown in Figure 6.12. Of course, the designer must also consider the cost of fabricating a stiffened cylinder as compared with an unstiffened one in order to make a final decision as to which type to use.

6.9 Summary

The evaluation of current design standards shows the bending capacity is underestimated by a significant amount, particularly when failure is by general instability. These standards also provide specific rules to avoid interaction of different buckling modes, which generally introduce additional conservatism. However, as discussed in this chapter, interactive buckling can be included in a design curve if it is based on the results of physical experiments and their numerical simulation.

A parametric study has been carried out using the physical and numerical test results. Key parameters for the failure in the stiffened area are found to be the ratios R/t , s/t and J_s/t^4 , and they are employed in a design formula to predict the ultimate moment. The capacity for shell buckling outside the stiffened area can be calculated by modifying the equations for unstiffened cylinders under compression. Parameters governing the failure pattern have also been identified.

**Table 6.1 Ultimate Moment Predicted
by API Design Guideline**

Specimen		$M_{u \text{ API}}^a$ (kN·m)	M_u^b (kN·m)	Error ^c (%)
<u>General buckling</u>				
1.	SB1	2248	3068	-26.7
2.	SB3b	1026	1333	-23.0
3.	SB4	1461	1857	-21.3
4.	S11	1404	2321	-39.5
5.	S12	1404	2262	-37.9
6.	S13	928	2078	-55.3
7.	S21	5807	7960	-27.0
8.	S22	5807	7680	-24.4
9.	S31	12955	16526	-21.6
10.	S32	12955	15727	-17.6
<u>Shell buckling between stiffeners</u>				
11.	S14	1573	1852	-15.1
12.	S23	5181	6499	-20.3
13.	S24	4868	5846	-16.7
14.	S33	10447	12776	-18.2
15.	S34	9869	11027	-10.5

^a ultimate moment predicted by API (1987).

^b ultimate moment obtained from experiments and finite element analysis.

^c error = $(M_{u \text{ API}} / M_u - 1) 100\%$

Table 6.2 Ultimate Moment Predicted by Equation 6.13

	Specimen	R / t	s / t	J _s / t ⁴	M _u ^a _{prd} (kN·m)	M _u ^b (kN·m)	Error ^c (%)	
Tests	1.	SB1	128.2	42.6	170.9	3241	3068	5.6
	2.	SB3b	205.8	57.0	340.4	1360	1333	2.0
	3.	SB4	189.0	41.9	241.3	1819	1857	−2.0
Finite element analyses	4.	S11	120	54	169.6	2297	2321	−1.0
	5.	S12	120	54	169.6	2238	2262	−1.0
	6.	S13	120	81	169.6	2039	2078	−1.9
	7.	S14	120	108	169.6	1857	1852	0.2
	8.	S21	240	54	169.6	7824	7960	−1.7
	9.	S22	240	54	169.6	7589	7680	−1.2
	10.	S23	240	81	169.6	6585	6499	1.3
	11.	S24	240	108	169.6	5699	5846	−2.5
	12.	S31	360	54	169.6	15873	16526	−4.0
	13.	S32	360	54	169.6	15409	15757	−2.2
	14.	S33	360	81	169.6	12841	12776	0.5
	15.	S34	360	108	169.6	10673	11027	−3.2
	16.	S25	240	54	50.56	6593	6404	3.0

^a ultimate moment calculated by Equation 6.13.

^b ultimate moment obtained from experiments and finite element analysis.

^c error = $(M_{u\text{ prd}} / M_u - 1) 100\%$

Table 6.3 Comparison of Design Capacity

Unstiffened cylinders			Stiffened cylinders			Failure mode
R/t	$M_{u\text{ prd}}$ (kN·m)	$\frac{M_{u\text{ prd}}}{M_p}$	Specimen	$M_{u\text{ prd}}$ (kN·m)	$\frac{M_{u\text{ prd}}}{M_p}$	
120	1341	0.62	S11	2297	0.90	general buckling
			S12	2238	0.90	general buckling
			S13	2039	0.83	general buckling
			S14	1857	0.78	shell buckling
240	3865	0.45	S21	7824	0.78	general buckling
			S22	7589	0.78	general buckling
			S23	6585	0.68	shell buckling
			S24	5699	0.61	shell buckling
360	6724	0.35	S31	15873	0.71	general buckling
			S32	15409	0.71	general buckling
			S33	12841	0.60	shell buckling
			S34	10673	0.51	shell buckling

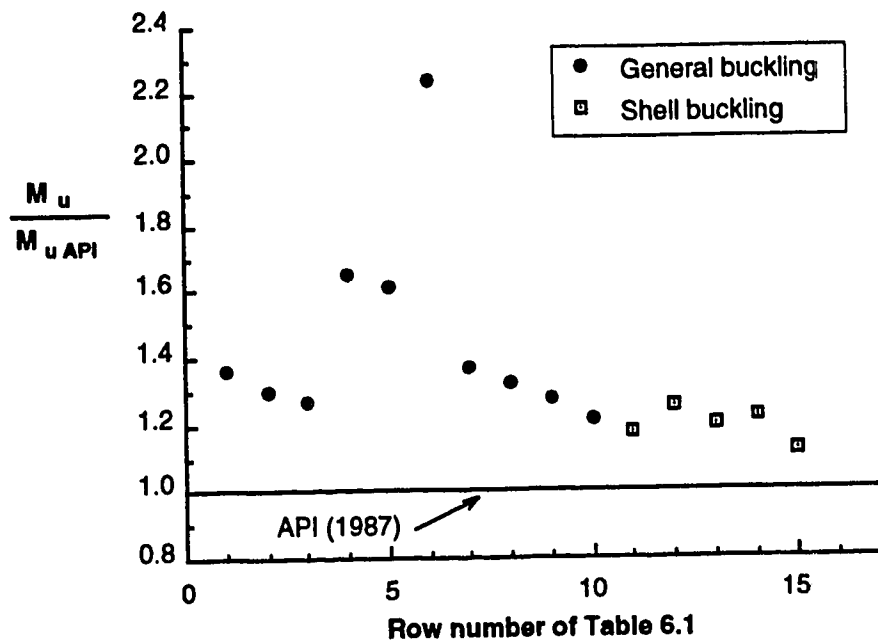


Figure 6.1 Comparison of API guideline with test and numerical analysis

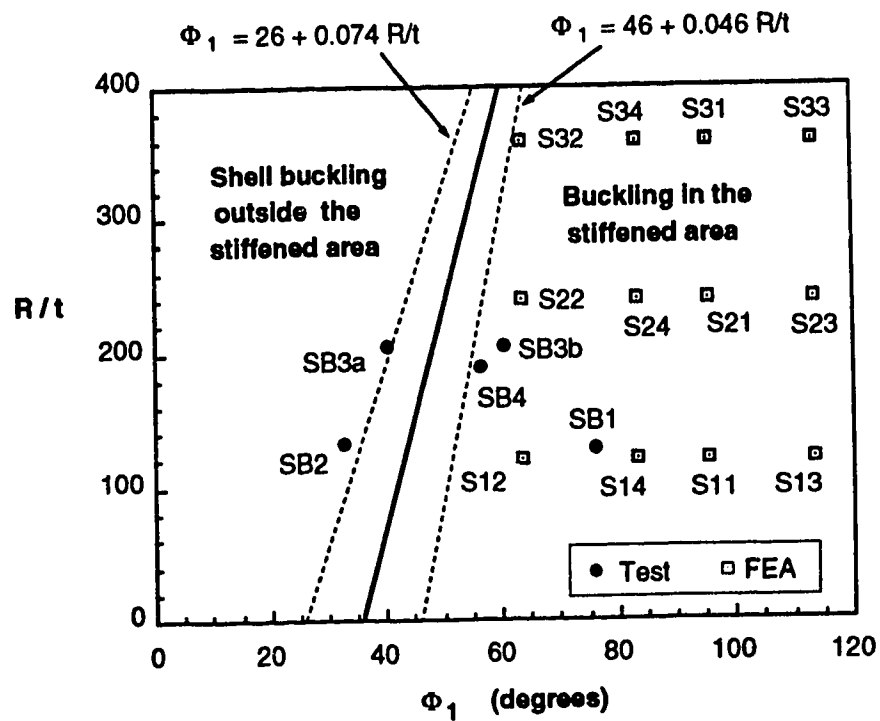


Figure 6.2 Failure mode: inside or outside the stiffened area

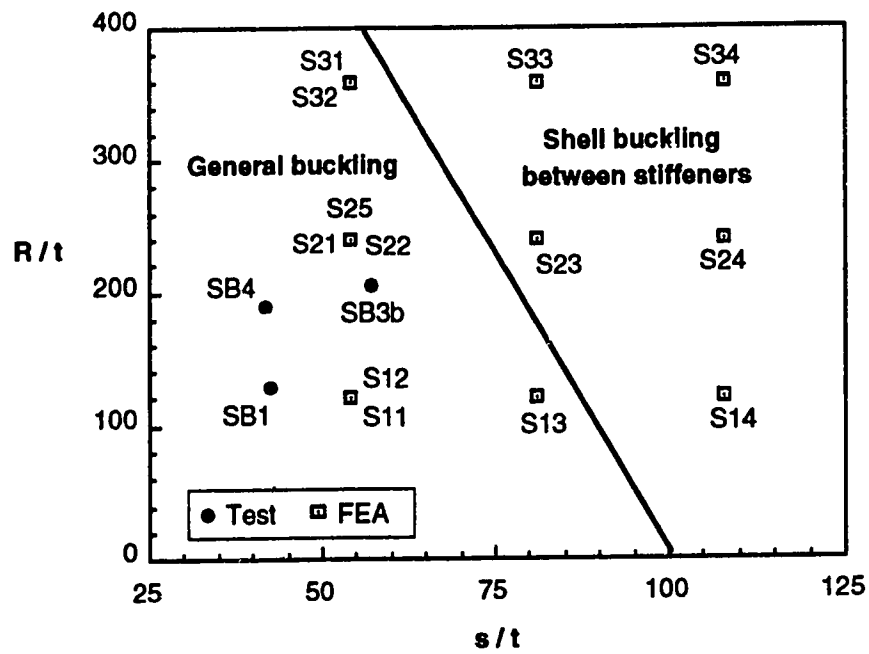


Figure 6.3 Failure in the stiffened area: general buckling versus shell buckling

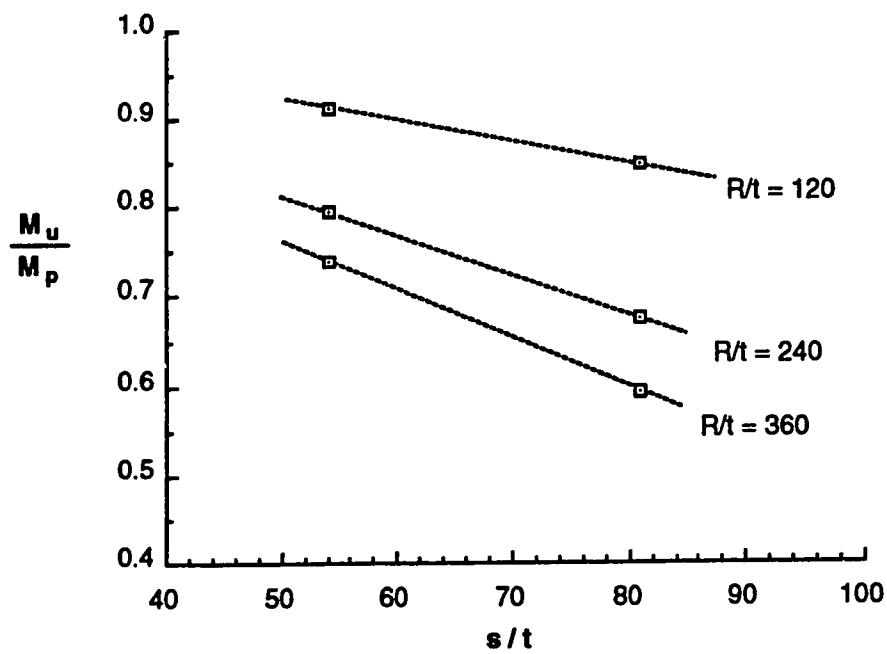


Figure 6.4 Effect of the spacing to thickness ratio (s/t) for $\Phi = 77.3^\circ$

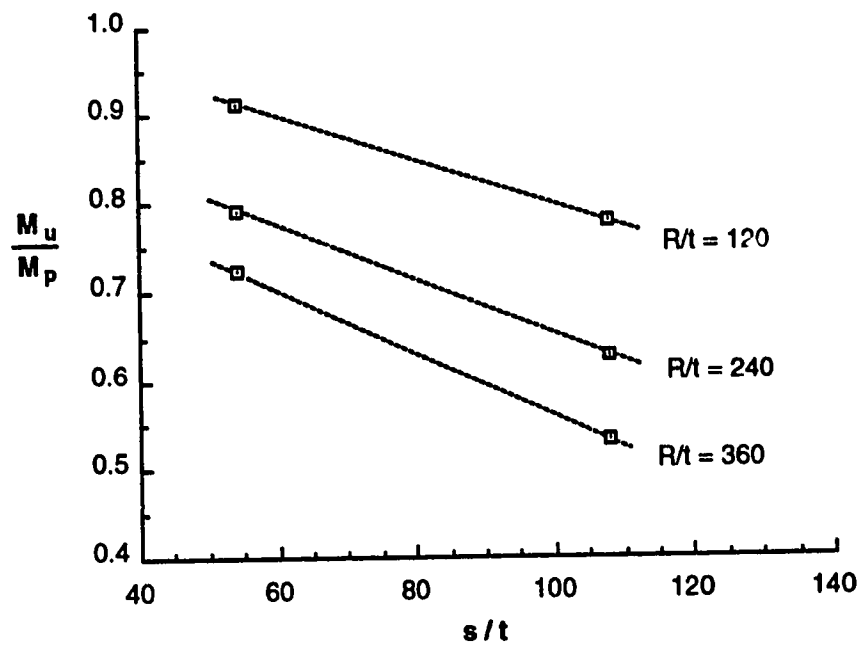


Figure 6.5 Effect of the spacing to thickness ratio (s/t) for $\Phi = 51.6^\circ$

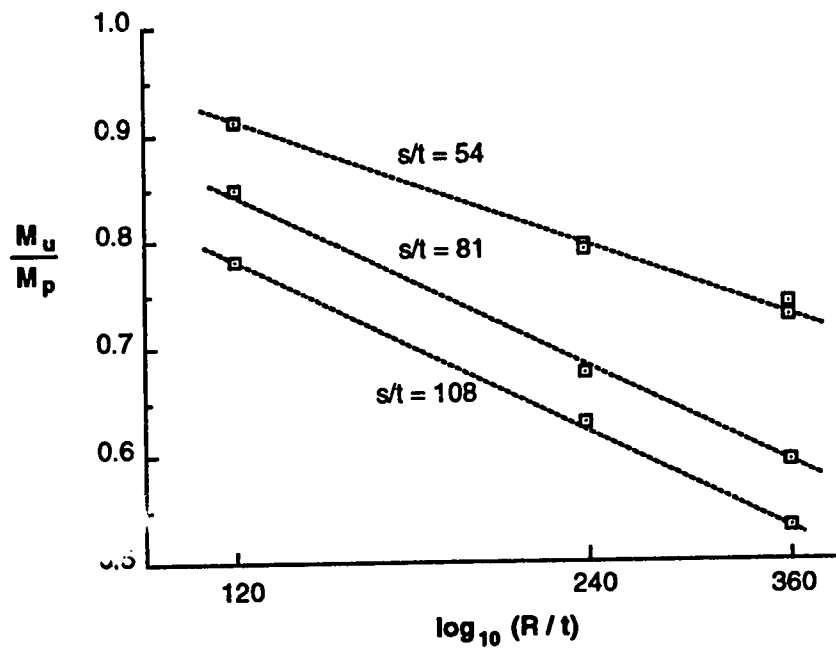


Figure 6.6 Effect of the radius to thickness ratio (R/t)

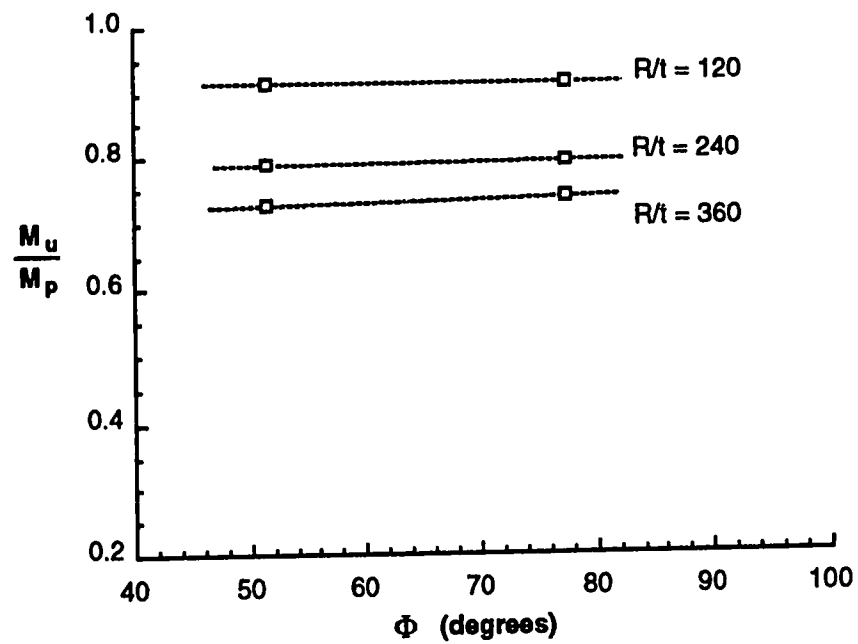


Figure 6.7 Effect of the angle Φ for $s/t = 54$

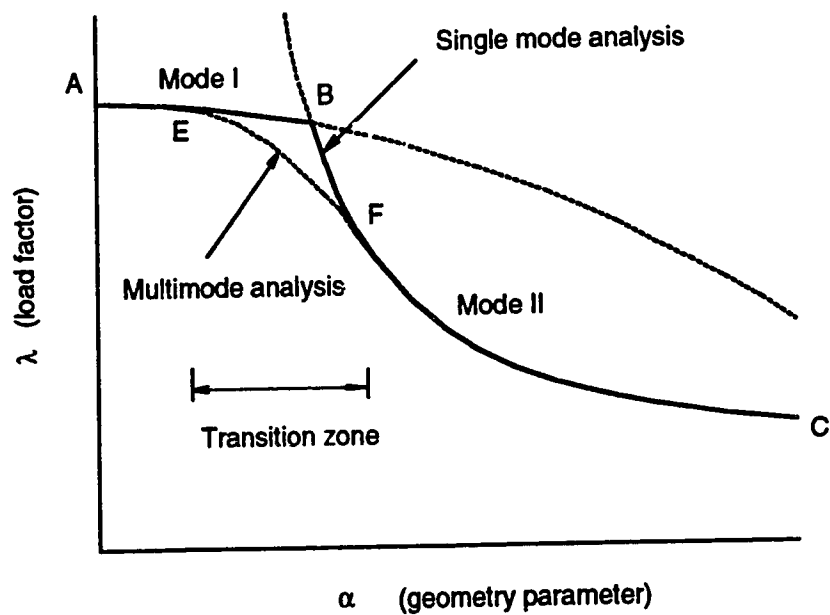


Figure 6.8 Design curves for multiple buckling modes

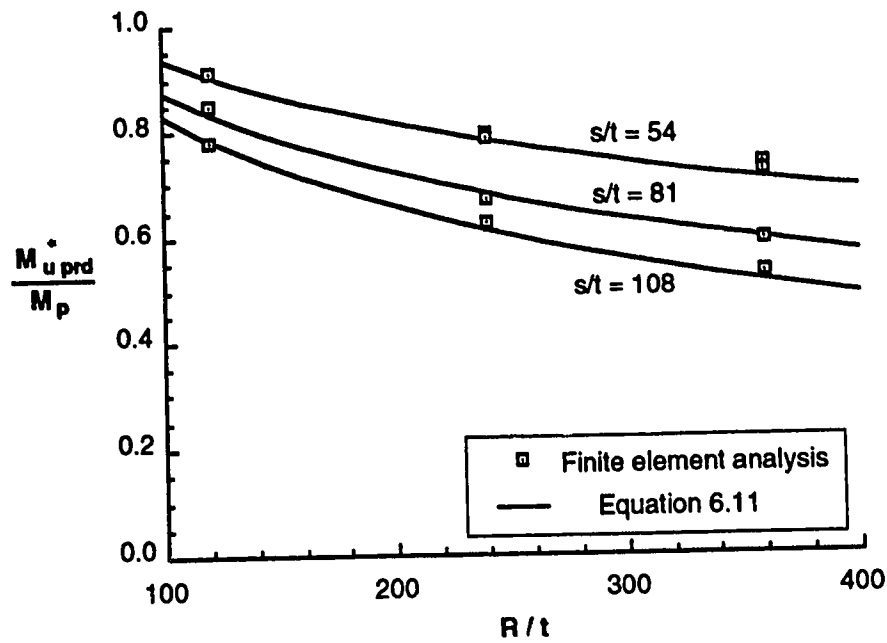


Figure 6.9 Comparison of Equation 6.11 with the finite element results

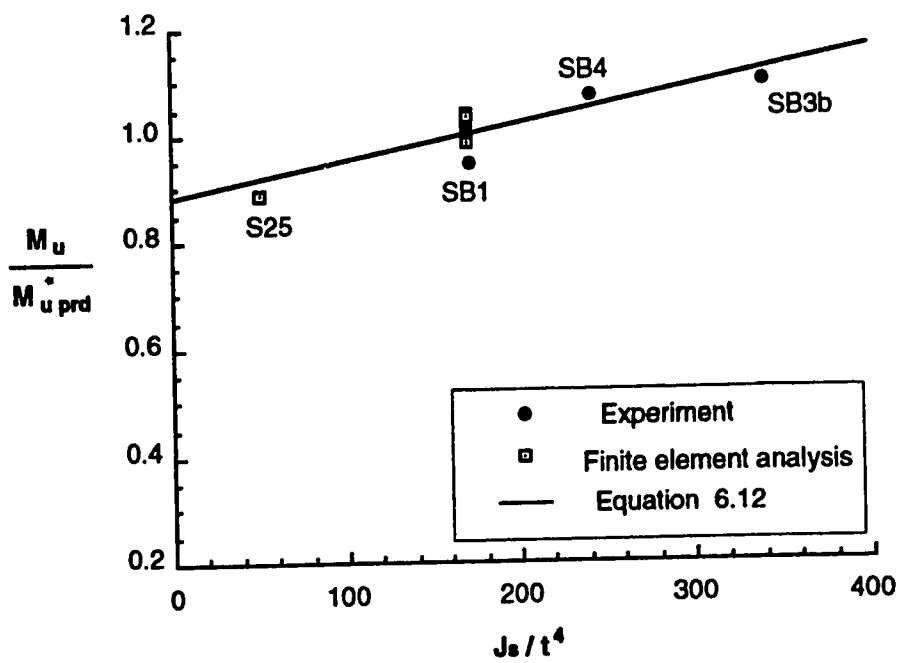


Figure 6.10 Effect of the torsional stiffness (J_s) of longitudinal stiffeners

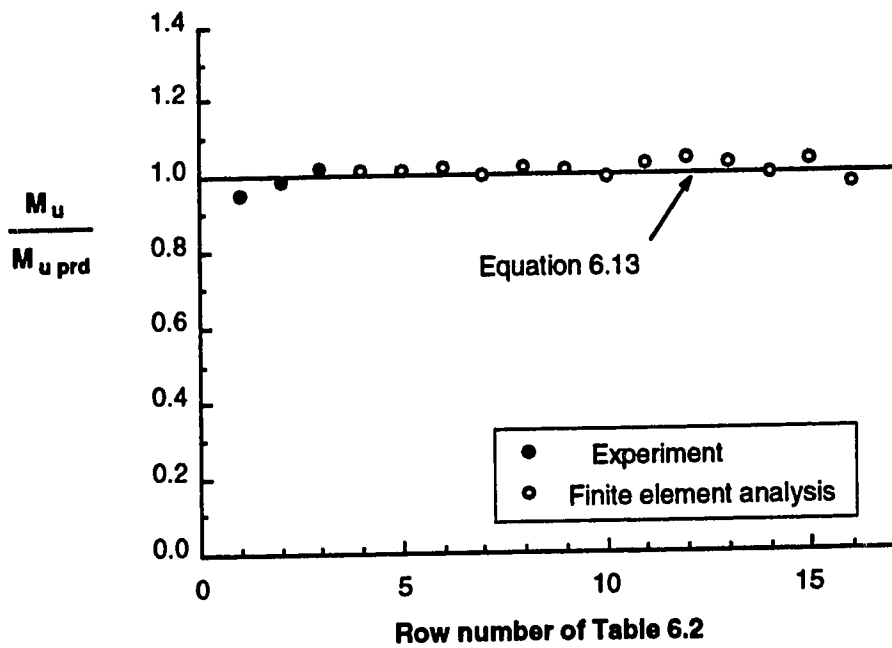


Figure 6.11 Comparison of Equation 6.13 with test and numerical results

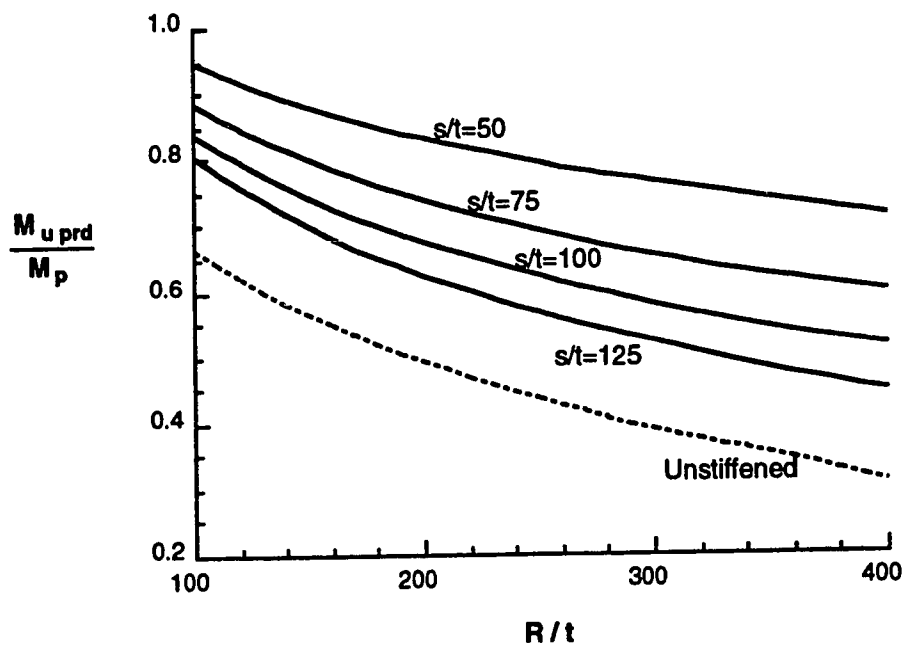


Figure 6.12 Comparison of stiffened versus unstiffened cylinders

CHAPTER SEVEN

CONCLUSIONS**7.1 Conclusions**

During this study, the research into the experiment, numerical analysis, and design of longitudinally stiffened cylinders subjected to bending has led to the following conclusions:

- (1) Existing design provisions significantly underestimate the ultimate flexural capacity, especially for cylinders that fail by general buckling. The conservatism arises from the use of elastic flexural stress calculations and allowable stress design formulae in which bending is not distinguished from axial compression. In some cases, cylinders that failed by general buckling in the tests are classified into the category of shell buckling failure.
- (2) The two buckling modes, general buckling and shell buckling, have different characteristics. General buckling is a ductile failure and can reach a point close to the plastic moment. There is a significant load increase after the initial yielding and buckling of the shell which occur at the early loading stage due to the presence of compressive residual stress. On the other hand, shell buckling failure has an abrupt nature: the ultimate point immediately follows the initial buckling. The strength of shell buckling is substantially lower than that of general buckling failure.
- (3) Failure in the stiffened area involves the interaction between the stiffeners and the shell. The key parameters of its ultimate capacity were found to be the radius-to-thickness ratio, R/t , the ratio of stiffener spacing to shell thickness, s/t , and the torsional stiffness of the stiffeners, J_s . Employing these parameters, a design formula (Equation 6.13) is proposed to predict the capacity of this type of failure.
- (4) The parameters which differentiate between the two buckling modes, general buckling and shell buckling, in the stiffened area are the s/t and R/t ratios.

However, the failure capacity of the two modes and their interactive failure can be universally described by a single formula (Equation 6.13).

- (5) When shell buckling occurs outside the stiffened area, the buckling stress is found to be comparable with that of an unstiffened shell, and the load capacity can be calculated accordingly if the effect of the stress gradient is included. Such a failure can be distinguished from the failure inside the stiffened area by the angle Φ , the R/t and s/t ratios, and the level of compressive residual stress.
- (6) The imperfections measured in test specimens were found to be moderate. The cylinders with smaller shell thickness have relatively severe imperfections.
- (7) Substantial residual stresses was found after the welding of stiffeners. The compressive residual stress has a significant influence on initial yielding and shell buckling. In some cases, it also affect the failure mode by promoting shell buckling.
- (8) The uncombined effect of the imperfections and residual stresses on the ultimate moment capacity was found to be moderate. However, in order to establish a numerical model which can predict the behavior and capacity with a reasonable accuracy, these initial defects must be well defined and integrated into such a model.

7.2 Discussion

The stability of stiffened cylinders is a complicated subject which involves a large number of parameters and different buckling modes. The scope of the current study has covered the following items:

- (1) The R/t ratio of the cylinders is in the range between 120 to 360.
- (2) The material is low carbon hot-rolled structural steel, with a nominal yield stress around 250 to 350 MPa.
- (3) The stiffener is a closed form cross-section.
- (4) The loading case is pure bending.

Future research can be the expansion of any of the above. However, the most relevant topics for design might be the use of other forms of stiffeners, in particular thin-walled open cross-sections and flat steel strips, and the capacity under combined loading cases such as bending and axial compression or bending and shear.

The use of stiffeners with open cross-sections will introduce another buckling mode—torsional and distortional buckling of the stiffeners because of their low torsional stiffness (J_s). However, this buckling mode cannot be dealt with individually. Its interaction with the stability of adjacent shell plating must be considered.

It is also noted that the HSS stiffeners used in this investigation have selective dimensions ($J_s = 100t^4$ to $400t^4$). The established design equations need to be verified for closed form stiffeners with larger J_s values.

Another example for further study is the shell buckling outside the stiffened area and its interaction with other failure modes. Since the present study focuses on the failure inside the stiffened area, the experiments and numerical analysis have not generated sufficient information about the interaction between the failures inside and outside the stiffened area. For this reason, the two failure patterns, inside or outside the stiffened area, were treated separately in Chapter Six and their interaction has not been addressed.

References

- Agelidis, N., Harding, J. E. and Dowling, P. J. (1982), *Buckling Tests on Stringer Stiffened Cylinder Models Subject to Load Combinations*, Det norske Veritas Report No. 82-0298, U.K.
- API (1987), *Bulletin on Stability Design of Cylindrical Shells*, API BUL 2U, 1st ed., American Petroleum Institute, Washington D. C.
- ASME (1986), *Metal Containment Shell Buckling Design Methods*, Section III, Division 1, Boiler and Pressure Vessel Code Case No 284, Nuclear Components, American Society of Mechanical Engineers, New York.
- ASTM (1989), *Standard Test Methods of Tension Testing of Metallic Materials*, E8-89, American Society for Testing and Materials, Philadelphia, Pennsylvania.
- Bailey, R. W. and Kulak, G. L. (1984), *Flexural and Shear Behaviour of Large Diameter Steel Tubes*, Struct. Eng. Rep. No. 119, Department of Civil Engineering, University of Alberta, Edmonton, Alberta.
- Becker, H. (1958), "Strength of Stiffened Curved Plates and Shells," *Handbook of Structural Stability*, Part VI, NACA Tech. Note 3786, July.
- Block, D. L., Card, M. F. and Mikulas, M. M. (1965), *Buckling of Eccentrically Stiffened Orthotropic Cylinders*, NASA TN D-2960.
- Budiansky, B. (1974), "Theory of Buckling and Post-buckling Behavior of Elastic Structures," *Advances in Applied Mechanics*, 14, 1-65.
- Bykov, E. and Hutchinson, J. W. (1977), "Mode Interaction in Axially Stiffened Cylindrical Shells," *AIAA Journal*, 15, 941-948.
- Chen, W. F. and Han, D. J. (1985), *Tubular Members in Offshore Structures*, Pitman Advanced Publishing Program, Boston.

- Chryssanthopoulos, M. K., Baker, M. J. and Dowling, P. J. (1991a), "Imperfection Modeling for Buckling Analysis of Stiffened Cylinders", *Journal of Structural Engineering*, ASCE, 117, 1998–2017.
- Chryssanthopoulos, M. K., Baker, M. J. and Dowling, P. J. (1991b), "Statistical Analysis of Imperfections in Stiffened Cylinders", *Journal of Structural Engineering*, ASCE, 117, 1979–1997.
- Croll, J. G. A. (1985), "Stiffened Cylindrical Shells under Axial and Pressure Loading," *Shell Structures*, Chapter 2, ed. by R. Narayanan, Elsevier Applied Science Publishers, Barking, Essex, England.
- DnV (1987), *Buckling Strength Analysis of Mobile Offshore Units*, Classification Notes, No. 30.1, Det norske Veritas, Norway.
- Dwight, J. B. (1982), "Imperfection Levels in Large Stiffened Tubes", *Buckling of Shells in Offshore Structures*, Offshore Structures Engineering III, ed. Harding, J. E., Dowling, P. J. and Agelidis, N., Gulf Pub. Co., London, U.K.
- ECCS (1988), *Buckling of Shells*, European Recommendations for Steel Construction, European Convention for Constructional Steelwork, Brussels, Belgium.
- Ellinas, C. P., Bastista, R. C. and Croll J. G. A. (1981), "Overall Buckling of Stringer Stiffened Cylinders," *Proc. ICE., Part 2*, 71, 479–512.
- Ellinas, C. P. and Croll J. G. A. (1983), "Experimental and Theoretical Correlations for Elastic Buckling of Axially Compressed Stringer Stiffened Cylinders", *Journal of Strain Analysis*, 18 (1), 41–67.
- Faulkner, D. (1977), "Effects of Residual Stresses on the Ductile Strength of Plane Welded Grillages and of Ring Stiffened Cylinders", *Journal of Strain Analysis*, 12, 130–139.
- Faulkner, D., Chen, Y. N. and deOliveira, J. G. (1983), "Limit State Design Criteria for Stiffened Cylinders of Offshore Structures," *ASME 4th National Congress of Pressure Vessels and Piping Technology*, Portland, Oregon.

- Green, D. R. and Nelson, H. M. (1982), "Compression Tests on Large-Scale, Stringer-Stiffened Tubes", *Buckling of Shells in Offshore Structures*, Offshore Structures Engineering III, ed. Harding, J. E., Dowling, P. J. and Agelidis, N., Gulf Pub. Co., London, U.K.
- Häfner, L., Ramm, E., Sättele, J. M. and Stegmüller, H. (1981), *NISA 80—Programmdokumentation—Programmsystem*, Bericht Des Institut Für Baustatik, Universität Stuttgart, Stuttgart, Germany.
- Harding, J. E., Dowling, P. J., Valsgard, S. and Walker, A. C. (1983), "The Buckling Design of Stiffened Shells Subject to Combined Pressure and Axial Compression," *1983 Offshore Technology Conference*, Vol. 1, Paper 4473, pp267–270.
- Hu, S. (1991), An Analytical Investigation of the Compressive Behavior of Fabricated Steel Tubes, Ph.D. Thesis, Department of Civil Engineering, University of Toronto, Toronto, Ontario.
- Hui, D., Tennyson, R. C. and Hansen, J. S. (1981) "Mode Interaction of Axially Stiffened Cylindrical Shells: Effects of Stringer Axial Stiffness, Torsional Rigidity, and Eccentricity", *Journal of Applied Mechanics, Transactions of ASME*, 48, 915–922
- Hutchinson, J. W. and Koiter, W. T. (1970), "Postbuckling Theory", *Applied Mechanics Review*, 23, 1353–1366.
- Hutchinson, J. W. and Amazigo, J. (1967), "Imperfection-Sensitivity of Eccentrically Stiffened Cylindrical Shells". *AIAA Journal*, 5, 392–401.
- Koiter, W. T. (1976), *General Theory of Mode Interaction in Stiffened Plate and Shell Structures*, Delft University of Technology, Report WTHD 91, Delft, Holland.
- Masubuchi, K. (1980), *Analysis of Welded Structures: Residual Stresses, Distorsion, and Their Consequences*, Pergamon, Oxford, U.K.

- Mok, J. and Elwi, A. E. (1986), *Shear Behavior of Large Diameter Fabricated Steel Cylinders*, Struct. Eng. Rep. No.136, Department of Civil Engineering, University of Alberta, Edmonton, Alberta.
- Obaia, K. H., Elwi, A. E. and Kulak, G. L. (1991), *Inelastic Transverse Shear Capacity of Large Fabricated Steel Tubes*, Struct. Eng. Rep. No.171, Department of Civil Engineering, University of Alberta, Edmonton, Alberta.
- Petrick, D. J. (1985), *Nonlinear Finite Element Analysis of Thin-Walled Cylindrical Shells Subject to Pure Bending*, M. Sc. Thesis, Department of Civil Engineering, University of Manitoba, Winnipeg, Manitoba.
- Pinkney, R. B., Stephens, M. J., Murray, D. W. and Kulak, G. L. (1983), "Use of Measured Imperfections to Predict the Buckling of Axially Loaded Cylindrical Shells", *Canadian Journal of Civil Engineering*, 10 (4), 662–669.
- Prion, H. G. L. and Birkemoe, P. C. (1987), "Beam–Column Behavior of Unstiffened Fabricated Steel Tubes", *Proceedings of the SSRC Annual Technical Session*, Houston, Texas.
- Ramm, E., (1980a), "A Plate/Shell Element for Large Deformation and Rotations, Nonlinear Finite Element Analysis in Structural Mechanics," *Proc. of the Europe–U.S. Workshop*, Ruhr Universitat, Bochum, Germany.
- Ramm, E. (1980b) "Strategies for Tracing the Nonlinear Response Near Limit Points", Nonlinear Finite Element Analysis in Structural Mechanics, *Proc. of the Europe–U.S. Workshop*, Ruhr Universitat, Bochum, Germany.
- Ramm, E. and Matzenmiller, A. (1986) "Large Deformation Shell Analyses Based on the Degeneration Concept", *Finite Element Methods for Plate and Shell Structures*, ed. by Hughes, T. J. R. and Hinton, E., Pineridge Press, Swansea, U.K.
- Roman, V. G. and Elwi, A. E. (1987), *Post-buckling Behavior of Thin Steel Cylinders under Transverse Shear*, Struct. Eng. Rep. No.146, Department of Civil Engineering, University of Alberta, Edmonton, Alberta.

SSRC (1988), *Guide to Stability Design Criteria for Metal Structures*, Structural Stability Research Council, ed. by T. V. Galambos, 4th ed., Wiley, New York.

Stephens, M. J., Kulak, G. L. and Montgomery, C. J. (1982), *Local Buckling of Thin-Walled Tubular Steel Members*, Struct. Eng. Rep. No.103, University of Alberta, Edmonton, Alberta.

Stegmüller, H. (1984), *NISA—Input Description*, Institut Für Baustatik, Universität Stuttgart, Stuttgart, Germany.

van der Neut, A. (1968), "The Interaction of Local Buckling and Column Failure of Thin-walled Compression Members," *Proc. Twelfth International Cong. Appl. Mech.*, Stanford, California.

Walker, A. C., Andronicou, A. and Sridharan, S. (1982), "Experimental Investigation of the Buckling of Stiffened Shells Using Small Scale Models", *Buckling of Shells in Offshore Structures*, Offshore Structures Engineering III, ed. by J. E. Harding, P. J. Dowling and N. Agelidis, Gulf Pub. Co., London, U.K.

Walker, A. C. and Sridharan, S. (1980), "Analysis of the Behaviour of Axial Compressed Stringer-Stiffened Cylindrical Shells", *Proc. ICE., Part 2*, 69, 447–472.

APPENDIX THE IGI PROGRAMS

Two programs, programs IGI1 and IGI2, were written to convert the raw data of initial imperfections into useful information.

1. Description of Program IGI1

Program IGI1 reads the raw data from specimen measurements, and perform a data analysis in order to

- (1) find the perfect cylinder which is the best-fit of the specimen; and
- (2) compute the imperfections of the three categories as described in Section 3.2.3.2.

The input variables are:

- n0 = number of measured points at each cross-section;
- m0 = number of measured cross-sections;
- R0 = radius of the measuring device;
- theda0 = angle θ which corresponds to the first point measured at each cross-section;
- thin = increment of angle θ ;
- x = x-coordinate of the cross-section;
- d0 = deflection of the axis in the measuring device;
- delta = a table containing the readings at each measuring points.

The output file of IGI1 is used for the input file of IGI2.

2. Description of Program IGI2

The following information is needed for the input:

- (1) the output of IGI1;
- (2) the nodal data of the perfect cylinder, which is generated by NISA.

With the input data, IGI2 calculates the x-, y-, and z-coordinates of each node for the imperfect specimen. The output file can be used as part of the input file for the NISA program.

3. The FORTRAN code of IGI1 and IGI2

c IGI1 — Implementation of Geometric Imperfection (STEP 1)

```
c-----
      dimension x(100), a(100), b(100), c(100), R(100), d0(100)
      dimension delta(100, 100), theda(100), w(100, 100)
```

```
c
      open(unit=2, file='IGI1.in')
      read(2, '(2i4, f10.4)') n0, m0, R0
      read(2, '(2f10.4)') theda0, thin
      read(2, '(5f10.4)') (x(j), j=1, m0)
      read(2, '(5f10.4)') (d0(j), j=1, m0)
      read(2, '(8f10.4)') ((delta(j, i), i=1, n0), j=1, m0)
```

```
c
c      **The theda is in degree. Need to convert into radius.**
```

```
c      pi=2.0*asin(1.0)
      theda0=theda0*pi/180.
      thin=thin*pi/180.
      do 100 ii=1, m0
      theda(ii)=float(ii-1)*thin+theda0
      if(theda(ii).gt.2.0*pi) theda(ii)=theda(ii)-2.0*pi
100    continue
```

```
c
c      **Find the best-fit circle by the least square method.**
```

```
c
      r11=0.
      r12=0.
      r13=0.
      r21=0.
      r22=0.
      r23=0.
      r31=0.
      r32=0.
      r33=0.
```

```
c
      do 300 ii=1, n0
      ss=sin(theda(ii))
      cc=cos(theda(ii))
      r11=r11+cc*cc
      r12=r12+ss*cc
      r13=r13+cc
      r21=r21+ss*cc
      r22=r22+ss*ss
      r23=r23+ss
      r31=r31+cc
      r32=r32+ss
      r33=r33+1.
```

```

300  continue
c
D=r11*r22*r33+r12*r23*r31+r13*r21*r32-r13*r22*r31-r11*r23*r32-r12*r21*r33
c
do 500 jj=1, m0
b1=0.
b2=0.
b3=0.
c
do 400 ii=1, n0
b1=b1+delta(jj, ii)*cos(theda(ii))
b2=b2+delta(jj, ii)*sin(theda(ii))
b3=b3+delta(jj, ii)
400  continue
c
Da=b1*r22*r33+r12*r23*b3+r13*b2*r32-r13*r22*b3-b1*r23*r32-r12*b2*r33
Db=r11*b2*r33+b1*r23*r31+r13*r21*b3-r13*b2*r31-r11*r23*b3-b1*r21*r33
Dc=r11*r22*b3+r12*b2*r31+b1*r21*r32-b1*r22*r31-r11*b2*r32-r12*r21*b3
c
a(jj)=Da/D
b(jj)=Db/D
c(jj)=Dc/D
c
**Compute Type(c) imperfection**
do 450 ii=1, n0
450  w(jj, ii)=delta(jj, ii)-a(jj)*cos(theda(ii))-b(jj)*sin(theda(ii))-c(jj)
500  continue
c
**Compute Type(a) imperfection**
do 600 j=2, m0-1
dx=(x(j)-x(1))/(x(m0)-x(1))
a(j)=a(j)-a(1)-(a(m0)-a(1))*dx
b(j)=b(j)-b(1)-(b(m0)-b(1))*dx-d0(j)
600  continue
a(1)=0.
b(1)=0.
a(m0)=0.
b(m0)=0.
c
** Compute Type(b) imperfection **
rm0=float(m0)
Rsum=0.
do 700 j=1, m0
R(j)=sqrt(R0*R0+2.*c(j)*R0)
700  Rsum=Rsum+R(j)
Ravg=Rsum/rm0
write(6, '(f12.6)') err
go to 699
c

```



```

800  open(unit=8, file="IGI1.o")
      write(8, '(2i4, 2f12.6)') n0, m0, R0, Ravg
      write(8, '(8f12.6)') (theda(i), i=1, n0)
      write(8, '(5f12.6)') (x(j), a(j), b(j), c(j), R(j), j=1, m0)
      write(8, '(8f12.6)') ((w(j, i), i=1, n0), j=1, m0)
      stop
      end

c
c  IGI2 — Implementation of Geometric Imperfection (STEP 2)
c  -----
c
      dimension xj(100), aj(100), bj(100), cj(100), Rj(100), theda(100)
      dimension w(100, 100), x(2000), y(2000), z(2000), irs(2000, 6)

c
c  **Read from "IGI1.o"**
c      read(5, '(2i4, 2f12.6)') n0, m0, R0, Ravg
      read(5, '(8f12.6)') (theda(i), i=1, n0)
      read(5, '(5f12.6)') (xj(j), aj(j), bj(j), cj(j), Rj(j), j=1, m0)
      read(5, '(8f12.6)') ((w(j, i), i=1, n0), j=1, m0)

c
c  **Read nodal data from NISA output **
c      read(5, '/i5') numnp
      read(5, 1020) ((irs(k, j), j=1, 6), x(k), y(k), z(k), k=1, numnp)
1020  format(5x, 6i5, 3f10.5)

c
      pi=asin(1.0)*2.0

c
c  **Expolate beyond theda=2pi so that the whole circle can be covered**
c
      theda(n0+1)=theda(1)+2.0*pi
      do 20 j=1, m0
20    w(j, n0+1)=w(j, 1)

c
      do 1000 k=1, numnp
      if(x(k).le.xj(1).or.x(k).ge.xj(m0)) go to 1000

c
c  **Linearly interpolate according to x(k)**
c      j=1
100  if(x(k).ge.xj(j).and.x(k).le.xj(j+1)) then
      ak=aj(j)+(aj(j+1)-aj(j))*(x(k)-xj(j))/(xj(j+1)-xj(j))
      bk=bj(j)+(bj(j+1)-bj(j))*(x(k)-xj(j))/(xj(j+1)-xj(j))
      Rk=Rj(j)+(Rj(j+1)-Rj(j))*(x(k)-xj(j))/(xj(j+1)-xj(j))
      else
      j=j+1
      if(j.ge.m0) then
      write(6, '(30Hj is greater than m0 — ERROR      )')
      stop
      endif

```

```

        go to 100
    endif

c
c    **Compute radius for stiffeners.**
c    **They are attached to the imperfect shell.**
c
    if(sqrt(y(k)*y(k)+z(k)*z(k)).gt.(Ravg+2.5)) then
        Rk=Rk+(sqrt(y(k)*y(k)+z(k)*z(k))-Ravg)
    endif

c
c    **Compute thedak from y(k) and z(k)**
101  if (abs(y(k))/R0.le.1.0e-15) then
        if (z(k).ge.0.0) thedak=pi/2.0
        if (z(k).le.0.0) thedak=3.0*pi/2.0
    else
        thedak=atan(z(k)/y(k))
        if (y(k).lt.0.0) thedak=thedak+pi
    endif
        if (thedak.lt.0.0) thedak=thedak+2.0*pi
        if (thedak.lt.theda(1)) thedak=thedak+2.0*pi

c
c    **Linearly interpolate w for x(k) and thedak **
c
    i=1
100  if(thedak.ge.theda(i).and.thedak.le.theda(i+1)) then
        w1=w(j, i)+(w(j+1, i)-w(j, i))*(x(k)-xj(j))/(xj(j+1)-xj(j))
        w2=w(j, i+1)+(w(j+1, i+1)-w(j, i+1))*(x(k)-xj(j))/(xj(j+1)-xj(j))
        wk=w1+(w2-w1)*(thedak-theda(i))/(theda(i+1)-theda(i))
    else
        i=1+i
        if(i.ge.(n0+1)) then
            write(6, '(25Hi is greater than n0-ERROR      )')
            stop
        endif
        go to 200
    endif

c
c    **Get new y(k) and z(k) which include initial imperfections.**
c
    y(k)=(Rk+wk)*cos(thedak)+ak
    z(k)=(Rk+wk)*sin(thedak)+bk
1000 continue

c
    write(6, 2010)(k, (irs(k, j), j=1, 6), x(k), y(k), z(k), 0, 0, k=1, numnp)
2010 format(7i5, f10.4, 2f10.4, i5, i2)
    stop
end

```